

**Squeezed light at 1064 nm and 1550 nm
with a nonclassical noise suppression beyond 10 dB**

Von der Fakultät für Mathematik und Physik
der Gottfried Wilhelm Leibniz Universität Hannover
zur Erlangung des Grades

Doktor der Naturwissenschaften
– Dr. rer. nat. –

genehmigte Dissertation
von

M.Sc. Moritz Mehmet

geboren am 7. September 1978 in Gießen

Januar 2012

Referent:	Prof. Dr. Roman Schnabel
Korreferent:	Prof. Dr. Karsten Danzmann
Tag der Promotion:	27.01.2012

Abstract

Squeezed states of light were observed for the first time in 1985. Since then they have developed into an important nonclassical tool in the field of high-precision metrology, for instance in gravitational wave detection, as well as in the field of quantum information, e.g. for teleportation and quantum cryptography. For all these applications a strong squeezing factor is beneficial.

This thesis presents a new benchmark value for squeezed light from non-monolithic squeezed-light sources. By means of parametric down-conversion, squeezed states at a wavelength of 1064 nm were generated and a nonclassical noise suppression of 12.3 dB was observed. In contrast to a monolithic resonator, the resonance frequency of this squeezed-light source can be adjusted to a downstream experiment.

In an additional experiment this squeezed-light source was utilized to determine the quantum efficiency of photo diodes. The applied method permits high precision since strong squeezing is sensitive to even low values of optical loss.

In view of the application of squeezed light in future-generation gravitational wave detectors and quantum information science, a dedicated squeezed-light source was developed and at a wavelength of 1550 nm squeezing in the continuous-wave regime was observed for the first time. These squeezed states were employed to quantum-enhance the sensitivity of a fiber-based Sagnac interferometer. Thus the compatibility of squeezing at 1550 nm with fiber-based quantum communication was demonstrated. Furthermore, upon thorough optimization of the squeezed-light generation and detection at 1550 nm, a quantum noise suppression of 12.3 dB was measured. Moreover, squeezing in the Fourier audio-band was observed for the first time.

The findings presented in this thesis constitute key research towards the squeezed-light technology at 1550 nm as it is required for future gravitational wave detectors such as the recently proposed Einstein Telescope.

Keywords: Squeezed light, gravitational wave detector, quantum information

Kurzzusammenfassung

Gequetschte Zustände des Lichts wurden 1985 erstmalig nachgewiesen. Seitdem haben sie sich zu einem wichtigen nichtklassischen Bestandteil im Bereich der hochpräzisen Messtechnik, wie etwa der Detektion von Gravitationswellen, und im Bereich der Quanteninformation, z.B. für Teleportation und Quantenkryptographie entwickelt. Für alle Anwendungen ist ein starker Quetschgrad von besonderem Interesse.

Mit dieser Arbeit wird ein neuer Maßstab für den durch nichtmonolithische Quetschlichtquellen erzeugbaren Quetschgrad gesetzt. Mittels parametrischer Abwärtskonversion wurden gequetschte Zustände bei einer Wellenlänge von 1064 nm erzeugt und eine nichtklassische Rauschunterdrückung von 12.3 dB gemessen. Im Gegensatz zu einem monolithischen Resonator kann die Resonanzfrequenz dieser Quetschlichtquelle an ein Folgeexperiment angepasst werden.

Mit dieser Quetschlichtquelle wurde in einem weiteren Experiment die Quanteneffizienz von Photodioden bestimmt. Die hier vorgestellte Methode erlaubt aufgrund der hohen Sensibilität stark gequetschter Zustände auf nur geringste optische Verluste eine besondere Präzision.

Im Hinblick auf die Verwendung von gequetschtem Licht in Gravitationswellendetektoren der zukünftigen Generation und in der Quanteninformation wurde eine weitere Quetschlichtquelle entwickelt und gequetschtes Licht bei einer Wellenlänge von 1550 nm erstmalig im Dauerstrichbetrieb nachgewiesen. Mithilfe dieser gequetschten Zustände wurde die Empfindlichkeit eines Faser-Sagnac Interferometers nichtklassisch erhöht. Hierdurch wurde gezeigt, dass gequetschtes Licht bei 1550 nm und faserbasierende Quantenkommunikation miteinander vereinbar sind.

Mit einer im Hinblick auf optische Verluste optimierten Quetschlichtquelle wurde wie bei 1064 nm ein Quetschgrad von 12.3 dB gemessen. Darüber hinaus wurde erstmals gequetschtes Licht bei 1550 nm im Bereich von Audiofrequenzen nachgewiesen.

Die Ergebnisse dieser Arbeit bilden die Grundlage für die Quetschlicht-Technologie bei 1550 nm, wie sie für zukünftige Gravitationswellendetektoren, wie dem kürzlich vorgeschlagenen Einstein Telescope, benötigt wird.

Stichworte: Gequetschtes Licht, Gravitationswellendetektor, Quanteninformation

Acknowledgments

I'd like to take the opportunity and express my gratitude to the many people who have helped me in completing this work in a variety of ways.

I especially thank Roman Schnabel for believing in me in the first place. I really enjoyed growing up in your quantum interferometry group.

A big thank you for allowing me to join their very unique team goes to the guys from the old school – Alexander Bunkowski, Oliver Burmeister, André Thüring, Boris Hage, Simon Chelkowski, Henning Vahlbruch, Nico Lastzka, Alexander Franzen, and Nicolai Grosse.

I am truly grateful to Michael Britzger and Daniel Friedrich. The two of you have been an important part of my life inside and outside the institute. I thank Stefan Ast, Tobias Eberle, Alexander Khalaidovski, and Henning Vahlbruch for proofreading parts of this thesis. Thanks Henning for your support during crunch-time.

I am grateful to Ping Koy Lam for having me in his quantum optics group at the Australian National University in Canberra, Australia. It was an exciting time; thank you to Nicolai Grosse, Syed Assad, and Michael Stefszky. It was a pleasure working with you.

To all colleagues here at the Institut für Gravitationsphysik: thank you for making science such an enjoyable thing. I would like to thank Karsten Danzmann for his admirable effort in leading such a thriving institution. The available support and the abundance of possibilities are truly exceptional.

I thank the administration, the mechanical- and the electronics workshop for their excellent work. I thank HIT for bits and bytes. I'd like to thank this year's AEI-football-team for winning the cup. Finally!

To Volker, Thorsten, Tina, and Bennett: you are phenomenal!

To my family: thanks for your support, understanding and encouragement over all the years.

Thank you Anke for your unlimited support and patience.

Moritz Mehmet, December 2011

Contents

Abstract	i
Kurzzusammenfassung	iii
Acknowledgments	v
Contents	vii
Glossary	xi
List of Figures	xiv
List of Tables	xvi
1 Introduction	1
References	5
2 Basic quantum optics	9
2.1 Quantization of the electromagnetic field	9
2.2 Quantum fluctuations	12
2.3 Quadrature operators and Heisenberg's Uncertainty Principle	13
2.4 Quantum states of light	15
2.4.1 Coherent states	15
2.4.2 Squeezed states of light	17
2.5 State representation	22
2.5.1 The density operator	22
2.5.2 Wigner function	25
2.5.3 Covariance matrix	28
2.5.4 Purity	28

References	29
3 Generation and detection of squeezed states	31
3.1 Generation of squeezed quantum noise	31
3.1.1 Second-order nonlinear interactions	31
3.1.2 Phase matching	32
3.1.3 Squeezed light from parametric down-conversion	33
3.2 Detection of quantum noise	36
3.2.1 Linearization of operators	37
3.2.2 Direct homodyne detection	38
3.2.3 Balanced homodyne detection	39
3.3 Limits to the measurable level of squeezing	41
3.3.1 Modeling optical loss	42
3.3.2 Total detection efficiency	44
3.3.2.1 Escape efficiency	44
3.3.2.2 Propagation efficiency	45
3.3.2.3 Photo-electric quantum efficiency	45
3.3.2.4 Homodyne efficiency	46
3.3.3 Squeezing bandwidth	46
3.3.4 Phase noise	48
3.3.5 Electronic dark noise	50
3.4 Model of a realistic squeezed-light source	51
References	52
4 Strong squeezing at 1064 nm from a monolithic squeezed light resonator	53
4.1 Introduction	53
4.2 Experimental setup	55
4.3 Observation of high-purity strongly squeezed states	57
4.4 Squeezed vacuum states in the photon-number basis	62
4.5 Observation of high-bandwidth squeezing	64
4.6 Conclusion	66
References	69
5 Strong squeezing as an estimator for optical loss	73
5.1 Introduction	73
5.2 Experimental setup	75
5.2.1 Laser preparation	75
5.2.2 Pump field preparation	77
5.2.3 Generation of squeezed vacuum states	79

5.2.4	Detection of squeezed vacuum states	80
5.3	Observation of 12.3 dB squeezing at 1064 nm	81
5.4	Experimental data vs. theory	83
5.4.1	Direct measurement of the linewidth and free spectral range	84
5.4.2	Deriving the detection efficiency via the level of squeezing and anti-squeezing	88
5.4.3	Loss analysis	88
5.4.4	Quantum efficiency of the photo diodes	90
5.5	Conclusion	90
	References	90
6	Squeezed light at 1550 nm	93
6.1	Introduction	93
6.2	Experimental setup	94
6.3	Observation of 5.3 dB squeezing	96
6.4	Conclusion	97
	References	99
7	A quantum-enhanced fiber Sagnac interferometer	101
7.1	Introduction	101
7.2	Experimental setup	104
7.3	Characterization of the squeezed states	104
7.4	Squeezed states in a Sagnac interferometer	105
7.5	Conclusion	107
	References	107
8	Strongly squeezed light at 1550 nm	109
8.1	Introduction	109
8.2	Experimental setup	111
8.3	Observation of 12.3 dB squeezing at 5 MHz sideband frequency	113
8.4	Characterization of the OPA	115
8.5	Low frequency performance	118
8.6	Conclusion	119
	References	120
9	Summary and Conclusion	123
	Curriculum vitae	127
	Publications	129

Glossary

Abbreviations

AR	Anti-reflection
BS	Beamsplitter
EOM	Electro-optical modulator
cw	Continuous-wave
DBS	Dichroic beamsplitter
FI	Faraday isolator
FWHM	Full width half maximum
BHD	Balanced homodyne detector
HR	High-reflection
HV	High voltage
LO	Local oscillator
M	Mirror
MC	Mode cleaner cavity
NPRO	Non-planar ring-oscillator
ND:YAG	Neodymium-doped yttrium aluminum garnet
OPA	Optical parametric amplification
OPO	Optical parametric oscillation
PBS	Polarizing beamsplitter
PD	Photodetector
PDH	Pound-Drever-Hall
PPKTP	Periodically-poled potassium titanyl phosphate
PZT	Piezo-electric transducer
RBW	Resolution bandwidth
ROC	Radius of curvature
SHG	Second harmonic generation
SQL	Standard quantum limit

TEM	Transverse electromagnetic Hermite Gauss
VBW	Video bandwidth
VIS	Visibility

Symbols

$\langle \hat{O} \rangle$	Expectation value of \hat{O}
$[\hat{A}, \hat{B}]$	Commutator of \hat{A} and \hat{B}
\hat{a}^\dagger	Creation operator
\hat{a}	Annihilation operator
$\chi^{(2)}$	Second order non-linearity
$\chi^{(3)}$	Third order non-linearity
$\Delta^2 \hat{o}, \text{Var}(\hat{o})$	Variance of \hat{O}
$\Delta \hat{o}$	Standard deviation of \hat{O}
ϵ_0	Electrical permeability
E_n	Energy eigenvalue
η	Total detection efficiency
η_{esc}	Escape efficiency
η_{prop}	Propagation efficiency
η_{homo}	Homodyne efficiency = VIS^2
η_{qe}	Quantum efficiency of photo diode
\mathcal{F}	Finesse
f	Frequency
γ	Cavity decay rate
h	Planck-constant
$\hbar = h/2\pi$	Reduced Planck-constant
\hat{H}, H	Hamilton-operator, Hamilton-function
i_-	Photocurrent difference
l	Cavity round-trip length
μ	Purity
μ_0	Magnetic permeability
\hat{n}	Number operator
$\hat{\rho}$	Density operator
ν	cavity linewidth (FWHM)
r	Squeezing-parameter
σ	Standard deviation

ζ	Covariance matrix
$\hat{S}(\xi)$	Squeezing-operator
τ	cavity round-trip time
ω	Angular frequency
ϕ	Phase angle
p	Position
P	Laser power
\mathcal{P}	Electric polarization
q	Momentum
V	Variance
$W(x, p)$	Wigner-Function
$\hat{X}^\theta, \hat{X}(\theta)$	Generic quadrature-operator
$\hat{X}_1 = \hat{X}^{\theta=0}$	Amplitude-quadrature operator
$\hat{X}_2 = \hat{X}^{\theta=\pi/2}$	Phase-quadrature operator
\hat{Y}_1, \hat{Y}_2	Rotated quadrature operator

List of Figures

2.1	Phase-space picture of a coherent state and of a vacuum state	18
2.2	Phase-space picture of squeezed states 1	20
2.3	Phase-space picture of squeezed states 2	21
2.4	Density matrix for a (squeezed) vacuum state	23
2.5	Photon number distribution of a (squeezed) vacuum state	24
2.6	Wigner function of a vacuum state and of a coherent state	26
2.7	Wigner function of a squeezed vacuum state	26
2.8	Probability density distribution	27
3.1	Schematic of a simple OPA	34
3.2	Squeezing and anti-squeezing from an OPA	36
3.3	Schematic setup for balanced homodyne detection	39
3.4	Model of optical loss	42
3.5	Squeezing and anti-squeezing vs. detection efficiency.	44
3.6	Squeezing and anti-squeezing vs. sideband frequency	47
3.7	Wigner function of a phase-diffused squeezed state	49
3.8	Squeezing and anti-squeezing vs. sideband frequency for a phase-diffused squeezed vacuum state	50
4.1	Experimental apparatus	57
4.2	Quadrature noise variances as measured by balanced homodyne detection of three different states produced by the OPO	59
4.3	Wigner function of the squeezed vacuum state produced by the monolithic squeezed light source	61
4.4	Density matrix of the squeezed state of Fig. 4.2(c)	62
4.5	Photon-number oscillation	63
4.6	High bandwidth squeezing spectrum of the monolithic squeezed light source	65
5.1	Experimental setup for the hemilithic squeezer at 1064 nm	75

5.2	CAD drawing of the mode cleaner design	76
5.3	Layout and optical properties of the SHG and photo of a MgO:LiNbO ₃ - crystal	77
5.4	SHG transmission and corresponding error signal	78
5.5	Optical properties of the PPKTP crystal and basic optical layout if the OPA	79
5.6	12.3 dB of squeezing at 1064 nm	82
5.7	Anti-squeezing and squeezing measured as a function of the pump power.	83
5.8	Schematic of the experimental setup for direct measurement of the cavity linewidth and free spectral range	86
5.9	Measurement of the linewidth of the squeezing cavity	86
5.10	Measurement of the free spectral range of the squeezing cavity	87
5.11	Dark-noise corrected squeezing and anti-squeezing as a function of the pump power	88
6.1	Schematic of the experimental setup for the first 1550 nm squeezer	95
6.2	Linearity of the homodyne detector	97
6.3	Squeezing of 5.3 dB at 1550 nm at sideband frequency of 5 MHz	98
7.1	Experimental setup for the squeezing-enhanced fiber Sagnac interferometer	103
7.2	Direct observation of 6.4 dB squeezing at 1550 nm	105
7.3	Squeezing-enhanced fiber Sagnac interferometer output signal	106
8.1	Schematic of the experimental setup for the third 1550 nm squeezer . . .	112
8.2	Squeezing of 12.3 dB at 1550 nm at a sideband frequency of 5 MHz . . .	114
8.3	Measured squeezing and anti-squeezing vs. pump power	116
8.4	Measured squeezing and anti-squeezing vs. frequency	117
8.5	Squeezing at 1550 nm in a frequency band from 1.5 kHz to 80 kHz	118

List of Tables

5.1	Measurement data I	84
5.2	Measurement data II	85

Introduction

Squeezed states of light are nonclassical states of the electromagnetic field. The first observation of squeezed states was reported in 1985 in the work by Slusher *et al.* [1.1]. The conceptual ideas of squeezed states date back to the 1920's [1.2], however it took the invention of the laser in the 1960's to stimulate active research within the field of quantum optics. The first detailed theoretical analysis of squeezed states was presented by Yuen [1.3] in 1976.

The basic idea behind squeezed light is intuitive: as a result of Heisenberg's uncertainty principle even a perfect laser produces light with an intrinsic noise, the so-called quantum noise. Quantum noise cannot be eliminated. However, it can be redistributed. At the expense of an increased noise in one variable of the light field, the quantum noise can be reduced in the conjugate variable. A measurement system can consequently profit from squeezing if it is based on the variable with reduced (squeezed) noise. In that case it can be more precise than a conventional (classical) measurement by means of coherent states, for which the quantum fluctuations are equally distributed over the electric field amplitude and phase quadrature, respectively. It is plausible that the quantum-enhancement increases with the strength of the squeezing.

Since their first observation, squeezed states have been used, for example, to demonstrate the Einstein-Podolski-Rosen paradox [1.4, 1.5], as a resource for quantum teleportation [1.6–1.8], and for the generation of Schrödinger cat states for quantum information networks [1.9, 1.10]. Currently, the most prominent application of squeezed states and the main motivation for the work presented in this thesis is the sensitivity enhancement of gravitational wave interferometers.

Gravitational waves (GWs) – periodical changes of space-time curvature traveling through the universe at the speed of light – were predicted by Einstein's theory of general relativity as a consequence of accelerated massive objects [1.11, 1.12]. For

the strongest anticipated astrophysical events, the associated relative length change in the distance between two points in space is only of the order of 10^{-22} or less [1.13], which makes the direct detection of GWs one of the most challenging enterprises in contemporary experimental physics. A direct detection would not only validate the theory of general relativity, but it would also constitute the foundation for gravitational wave astronomy, a novel way to probe the universe for electromagnetically dark objects [1.14].

In the pursuit of a first detection, several kilometer-scale laser Michelson interferometers (see for example References [1.15–1.17]) have been constructed. The sensitivity of these GW detectors, which measure the relative change in the distance between their end mirrors, is ultimately limited by quantum noise, namely the vacuum fluctuations of the electromagnetic field.

Already in 1981, Caves [1.18] proposed to use squeezed states of light to enhance the sensitivity of GW interferometers beyond their quantum noise limit. The analysis of the interferometer response (to a phase signal) showed that the measurement noise at a given frequency arises only from one quadrature of the vacuum field entering through the dark port of the interferometer. Caves' idea was to replace the vacuum field by a *squeezed* vacuum field with less noise in this quadrature, thereby reducing the quantum noise and hence increasing the signal to shot noise ratio.

Following Caves' suggestion, several table top experiments were set up to prove the compatibility of the squeezed light technique with today's GW detectors, see e.g. [1.19–1.22]. Only recently, a squeezed light add-on was successfully integrated into the km-scale GW detector GEO 600. A broadband noise reduction of up to 3.5 dB in the detector's shot-noise limited regime has been demonstrated [1.23]. The demonstrated sensitivity improvement corresponds to a laser power increase by a factor of 2.2.

Currently, all of the existing GW interferometers are undergoing major upgrades. State of the art technology will turn them into second-generation, or so-called advanced detectors [1.24–1.26] with an intended ten-fold improvement in sensitivity. As part of the upgrades, a considerable increase in laser power is intended. In advanced LIGO [1.24] for instance, it is planned to store up to 1 MW in the interferometer arm cavities. This might lead to a critical thermal load on the interferometer components. Since, in terms of sensitivity improvement, the injection of squeezing is equivalent to increasing the laser power, here the application of squeezed light would allow for a reduction of the design laser power in order to reach the same sensitivity [1.27]. However, in the case that the thermal load can be managed, the squeezed-light technique can lead to an additional sensitivity enhancement.

Beyond these advanced detectors, plans for third-generation instruments already exist. One of the most ambitious projects is a joint European proposal, the so-called Einstein

Telescope (ET) [1.28]. With a broad band improvement by one order of magnitude over the second generation detectors, ET is meant to constitute an observatory for routine GW detection. It is planned for ET to utilize cryogenically cooled interferometers, in order to reduce the contribution of thermal noise. This would imply a change of test mass material to enable efficient cooling. In this respect, the most promising candidate is crystalline silicon [1.29]. Silicon is opaque to the laser wavelength used in today's GW detectors, but it is highly transparent at the wavelength of 1550 nm. As a consequence, the use of crystalline silicon requires changing the interferometer baseline laser wavelength from 1064 nm to 1550 nm [1.30, 1.31].

The improvement in the sensitivity of today's GW detectors by squeezed light is limited by optical loss inside the detectors [1.23] and by the fact that they are not quantum noise limited over their entire measurement band (10 Hz–10 kHz) but only at frequencies above approximately 500 Hz. However, the implementation of ultra low loss optical components will decrease the loss considerably in second- and third-generation detectors. Additionally, due to sophisticated seismic isolation and the reduction of thermal noise, the quantum noise contribution will be significant over most of the detection band. Hence future GW detectors will benefit considerably more from the injection of strong squeezing. Since squeezed-light enhancement is indeed considered for ET [1.28], continuous-wave squeezed states at 1550 nm are also required.

All of the current GW interferometers are operated with lasers at 1064 nm. Hence, the squeezed-light research within the GW community has quite naturally been focused on providing squeezing at that respective wavelength. And indeed, the strongest squeezing value observed so far (12.7 dB [1.32]) was achieved at the wavelength of 1064 nm. However, a monolithic squeezer was used. Monolithic squeezers do not seem to be applicable to GW detectors since dynamic tuning of their resonance frequency to follow the wavelength of interferometer's laser has not been demonstrated. The work in this thesis was therefore dedicated to investigate the limits for strongly squeezed states at both the wavelength of 1064 nm and 1550 nm from squeezed light source that are compatible with existing and future GW technology.

Structure of the thesis

Most of the research presented in this thesis was published in four peer-reviewed journal papers. Together with one complementary experiment (Chapter 5), these constitute the main body of the text.

Chapter 2 presents the background theoretical material, explains some of the key concepts of quantum optics and holds terms and definitions.

Chapter 3 introduces the main concepts underlying the generation and detection of squeezed light. A detailed analysis of the limitations to the detectable squeezing level is given. The chapter closes with the presentation of a model for the output of a realistic squeezed light source.

Chapters 4 and 5 both discuss the generation of strong squeezing at the wavelength of 1064 nm. Chapter 4 presents the realization of strong squeezing by means of a monolithic squeezed-light source. The direct detection of 11.5 dB is demonstrated and a squeezing bandwidth of ~ 170 MHz is reported. The observed squeezed states are mathematically analyzed with respect to their Wigner function, density matrix and photon number distribution. With this experiment the necessary insight for the generation of strong squeezing was gained. It also provided the foundation for the experiment presented in Ref. [1.32] in which today's strongest squeezing was reported by means of monolithic squeezer made from PPKTP.

Chapter 5 reports the strongest squeezing from a non-monolithic squeezed-light source observed so far. A noise suppression of (directly measured) 12.3 dB at 1064 nm is demonstrated at a sideband frequency of 5 MHz. A detailed characterization of the squeezed-light source performance is provided. By fitting the data to a model, the value of overall detection efficiency is used to deduce the quantum efficiency of the photo diodes.

Chapters 6 through 8 report the development of continuous-wave squeezed light at the telecommunication wavelength of 1550 nm. The first proof-of-principle experiment is presented in Chapter 6. An advanced setup and the application of squeezed states at 1550 nm in a fiber-based Sagnac interferometer is presented in Chapter 7. Today's strongest squeezing of (again) 12.3 dB together with the observation of squeezed light at sideband frequencies in the audio band is described in Chapter 8.

Chapter 9 provides a summary and overall conclusions.

References

- [1.1] R. E. Slusher, L. W. Hollberg, B. Yurke, J. C. Mertz, and J. F. Valley, "Observation of squeezed states generated by four-wave mixing in an optical cavity," *Phys. Rev. Lett.* **55**, 2409–2412 (1985).
- [1.2] V. V. Dodonov, „‘Nonclassical’ states in quantum optics: a ‘squeezed’ review of the first 75 years“, *J. Opt. B:Quantum Semiclass. Opt.* **4**, R1 (2002).
- [1.3] H. P. Yuen, "Two-photon coherent states of the radiation field," *Phys. Rev. A* **13**, 2226–2243 (1976).
- [1.4] A. Einstein, B. Podolsky, and N. Rosen, "Can quantum-mechanical description of physical reality be considered complete?," *Phys. Rev.* **47**, 777–780 (1935).
- [1.5] Z. Y. Ou, S. F. Pereira, H. J. Kimble, and K. C. Peng, "Realization of the Einstein-Podolsky-Rosen paradox for continuous variables," *Phys. Rev. Lett.* **68**, 3663–3666 (1992).
- [1.6] D. Bouwmeester *et al.*, "Experimental quantum teleportation," *Nature* **390**, 575–579 (1997).
- [1.7] A. Furusawa *et al.*, "Unconditional quantum teleportation," *Science* **282**, 706–709 (1998).
- [1.8] W. P. Bowen *et al.*, "Experimental investigation of continuous-variable quantum teleportation," *Phys. Rev. A* **67**, 032302 (2003).
- [1.9] A. Ourjoumtsev, R. Tualle-Brouri, J. Laurat, and P. Grangier, "Generating optical Schrödinger Kittens for Quantum Information Processing," *Science* **312**, 83 (2006).
- [1.10] J. S. Neergaard-Nielsen, B. Melholt Nielsen, C. Hettich, K. Mølmer, and E. S. Polzik, "Generation of a superposition of odd photon number states for quantum information networks," *Phys. Rev. Lett.* **97**, 083604 (2006).
- [1.11] A. Einstein, "Näherungsweise Integration der Feldgleichungen der Gravitation," *Sitzungsberichte der Preussischen Akademie der Wissenschaften zu Berlin* 688, (1916).
- [1.12] A. Einstein, "Über Gravitationswellen," *Sitzungsberichte der Preussischen Akademie der Wissenschaften zu Berlin* 154, (1918).

- [1.13] C. Cutler and K. Thorne, "An overview of gravitational-wave sources," Proceedings of the 16th International Conference on General Relativity & Gravitation, World Scientific (2002).
- [1.14] B. F. Schutz, "Gravitational wave astronomy," *Classical and Quantum Gravity*, **16**, A131–A156 (1999).
- [1.15] B. Abbott, et al., "LIGO: the Laser Interferometer Gravitational-Wave Observatory," *Rep. Prog. Phys.* **72**, 076901 (2009).
- [1.16] T. Accadia et al., "Status of the Virgo project," *Class. Quantum Grav.* **28**, 114002 (2011).
- [1.17] H. Grote and the LIGO Scientific Collaboration, "The GEO 600 status," *Class. Quantum Grav.* **27**, 084003 (2010).
- [1.18] C. M. Caves, "Quantum-mechanical noise in an interferometer," *Phys. Rev. D* **23**, 1693 (1981).
- [1.19] K. McKenzie, D. A. Shaddock, D. E. McClelland, B. C. Buchler, and P. K. Lam, "Experimental demonstration of a squeezing-enhanced power-recycled Michelson interferometer for gravitational wave detection," *Phys. Rev. Lett.* **88**, 231102 (2002).
- [1.20] H. Vahlbruch, S. Chelkowski, B. Hage, A. Franzen, K. Danzmann, and R. Schnabel, "Demonstration of a squeezed-light-enhanced power- and signal-recycled Michelson interferometer," *Phys. Rev. Lett.* **95**, 211102 (2005).
- [1.21] H. Vahlbruch, S. Chelkowski, B. Hage, A. Franzen, K. Danzmann, and R. Schnabel, "Coherent Control of Vacuum Squeezing in the Gravitational-Wave Detection Band," *Phys. Rev. Lett.* **97**, 011101 (2006).
- [1.22] K. Goda, O. Miyakawa, E. E. Mikhailov, S. Saraf, R. Adhikari, K. McKenzie, R. Ward, S. Vass, A. J. Weinstein, and N. Mavalvala, "A quantum-enhanced prototype gravitational-wave detector," *Nat. Phys.* **4**, 472–476 (2008).
- [1.23] The LIGO Scientific Collaboration, "A gravitational wave observatory operating beyond the quantum shot-noise limit," *Nat. Phys.* **7**, 962–965 (2011).
- [1.24] G. M. Harry (for the LIGO Scientific Collaboration), "Advanced LIGO: the next generation of gravitational wave detectors," *Class. Quantum Grav.* **27**, 084006 (2010).

- [1.25] The Virgo Collaboration, "Advanced Virgo Baseline Design," note VIR-027A-09 May 16 (2009). <https://tds.ego-gw.it/itf/tds/file.php?callFile=VIR-0027A-09.pdf>
- [1.26] B. Willke et al., "The GEO-HF project," *Class. Quantum Grav.* **23**, 207–214 (2006).
- [1.27] R. Schnabel, N. Mavalvala, David E. McClelland, and P. K. Lam "Quantum metrology for gravitational wave astronomy," *Nat. Commun.* **1**, 121 (2010).
- [1.28] The ET Science Team, "Einstein gravitational wave Telescope (ET) conceptual design study," ET-0106C-10 (2011), <https://tds.ego-gw.it/ql/?c=7954>.
- [1.29] D. F. McGuigan, C. C. Lam, R. Q. Gram, A. W. Hoffman, and D. H. Douglass "Measurements of the mechanical Q of single-crystal silicon at low temperatures," *J. Low Temp. Phys.* **30**, 621 (1978).
- [1.30] S. Rowan, J. Hough, D. R. M. Crooks, "Thermal noise and material issues for gravitational wave detectors," *Phys. Lett. A* **347**, 25–32 (2005).
- [1.31] R. Schnabel, M. Britzger, F. Brückner, O. Burmeister, K. Danzmann, J. Dück, T. Eberle, D. Friedrich, H. Lück, M. Mehmet, R. Nawrodt, S. Steinlechner and B. Willke, "Building blocks for future detectors: Silicon test masses and 1550 nm laser light," *J. Phys.: Conf. Ser.* **228**, 012029 (2010).
- [1.32] T. Eberle, S. Steinlechner, J. Bauchrowitz, V. Händchen, H. Vahlbruch, M. Mehmet, H. Müller-Ebhardt, and R. Schnabel, "Quantum Enhancement of the Zero-Area Sagnac Interferometer Topology for Gravitational Wave Detection," *Phys. Rev. Lett.* **104**, 251102 (2010).

Basic quantum optics

This chapter reviews the basic theoretical concepts underlying the experiments presented in this thesis.

2.1 Quantization of the electromagnetic field

A traveling wave solution for a light field in free space can be derived from the Maxwell equations. More specific, we consider a monochromatic electromagnetic field that propagates in z -direction within a one-dimensional cavity with perfectly reflecting mirrors and assume the electric component to be x -polarized. The electric field that satisfies Maxwell's equations with the given boundary conditions reads (in SI units) [2.1]

$$E_x(z, t) = \left(\frac{2\omega^2}{V\epsilon_0} \right)^{1/2} q(t) \sin(kz) \quad (2.1)$$

and the y -polarized magnetic field can be written as

$$B_y(z, t) = \left(\frac{\mu_0\epsilon_0}{k} \right) \left(\frac{2\omega^2}{V\epsilon_0} \right) \dot{q}(t) \cos(kz). \quad (2.2)$$

In these equations ω , is the angular frequency of the mode, $k = \omega/c$ is the wave number, $q(t)$ is a time-dependent factor having the dimension of a length and $p(t) = \dot{q}(t)$ is a time-dependent factor having the dimension of a velocity. The constant coefficients depend on the chosen system of units and are of no importance for the following considerations. From Eqs. (2.1) and (2.2), one obtains the Hamiltonian [2.1]

$$H(q, p) = \frac{1}{2}(p^2 + \omega^2 q^2), \quad (2.3)$$

of the single-mode field [2.1]. The transition from the classical to the quantum mechanical description of the system can be made by applying the correspondence rule, according to which the canonical variables q and p can be replaced by their corresponding operators:

$$q \rightarrow \hat{q}, \quad p \rightarrow \hat{p} \quad . \quad (2.4)$$

The position operator \hat{q} and the momentum operator \hat{p} obey the commutation relation

$$[\hat{q}, \hat{p}] = i\hbar \quad . \quad (2.5)$$

Consequently, this yields the operators $\hat{E}_x(z, t)$ and $\hat{B}_y(z, t)$ for the electric and magnetic field, respectively, and the Hamilton operator is then given by

$$\hat{H} = \frac{1}{2}(\hat{p}^2 + \omega^2 \hat{q}^2). \quad (2.6)$$

To obtain dimensionless operators, the linear combinations

$$\hat{a} = (2\hbar\omega)^{-1/2}(\omega\hat{q} + i\hat{p}) \quad \text{and} \quad (2.7)$$

$$\hat{a}^\dagger = (2\hbar\omega)^{-1/2}(\omega\hat{q} - i\hat{p}) \quad (2.8)$$

can be chosen. These are the so-called annihilation operator \hat{a} and the creation operator \hat{a}^\dagger . Their commutator relation is given by

$$[\hat{a}, \hat{a}^\dagger] = \hat{a}\hat{a}^\dagger - \hat{a}^\dagger\hat{a} = 1 \quad . \quad (2.9)$$

This can be used to re-express the Hamilton operator as

$$\hat{H} = \frac{1}{2}\hbar\omega \left(\hat{a}\hat{a}^\dagger + \hat{a}^\dagger\hat{a} \right) = \hbar\omega \left(\hat{a}^\dagger\hat{a} + \frac{1}{2} \right). \quad (2.10)$$

To see what information about the system's energy is contained within this Hamiltonian, we first propose an energy eigenstate of the system $|n\rangle$ with the corresponding energy eigenvalue E_n , such that

$$\hat{H} |n\rangle = E_n |n\rangle \quad . \quad (2.11)$$

As the next step, we apply the creation operator to both sides of Eq. (2.11), such that $\hat{a}^\dagger \hat{H} |n\rangle = \hat{a}^\dagger E_n |n\rangle$. The expansion of the left hand side yields $\hbar\omega(\hat{a}^\dagger \hat{a}^\dagger \hat{a} + \frac{1}{2})\hat{a}^\dagger |n\rangle = E_n \hat{a}^\dagger |n\rangle$ and by using the commutation relation, Eq. (2.9), one obtains

$$\hat{H} \hat{a}^\dagger |n\rangle = (E_n + \hbar\omega) \hat{a}^\dagger |n\rangle \quad . \quad (2.12)$$

This is an eigenvalue equation for a new (unnormalized) state $\hat{a}^\dagger |n\rangle$ that is also an eigenstate of the Hamiltonian and possesses the energy eigenvalue $(E_n + \hbar\omega)$. The same can be done for the annihilation operator, which yields

$$\hat{H}(\hat{a} |n\rangle) = (E_n - \hbar\omega)(\hat{a} |n\rangle) . \quad (2.13)$$

Again, a new (unnormalized) eigenstate $\hat{a} |n\rangle$ is produced with the corresponding energy eigenvalue $(E_n - \hbar\omega)$.

One can interpret the application of the creation operator as bringing the system into a new state $|n + 1\rangle$ with an increased energy level $E_n + \hbar\omega$. The annihilation operator does the opposite and creates a new state $|n - 1\rangle$ with decreased energy $E_{n-1} = E_n - \hbar\omega$. This illustrates the origin of the names *creation operator* and *annihilaton operator*, since \hat{a}^\dagger creates and \hat{a} annihilates a quantum of energy $\hbar\omega$.

The total energy of the system must not be negative. Therefore, a state of minimum energy has to exist. This is the so-called *ground state* or *vacuum state*. It is denoted by $|0\rangle$. Since no eigenstate with an energy smaller than the ground state exists, the application of the annihilation operator to this state is defined by

$$\hat{a} |0\rangle = 0 . \quad (2.14)$$

The eigenvalue equation for the ground state thus is

$$\hat{H} |0\rangle = \hbar\omega \left(\hat{a}^\dagger \hat{a} + \frac{1}{2} \right) |0\rangle = \frac{1}{2} \hbar\omega |0\rangle . \quad (2.15)$$

From Eq. (2.15), it is evident that the lowest energy level – the *zero-point energy* – is $E_0 = \hbar\omega/2$. We know that the creation operator produces a quantum of energy $\hbar\omega$ each time it is applied. By starting from the ground state, the energy eigenvalues of the Hamiltonian can therefore be constructed according to

$$E_n = \hbar\omega \left(n + \frac{1}{2} \right), \quad n = 0, 1, 2, \dots \quad (2.16)$$

As a consequence, the field energy is quantized.

One can define the number operator \hat{n} as

$$\hat{n} = \hat{a}^\dagger \hat{a} . \quad (2.17)$$

By comparison with the Hamilton operator in Eq. (2.11), we find the effect of \hat{n} acting on a state $|n\rangle$ to be

$$\hat{n} |n\rangle = n |n\rangle . \quad (2.18)$$

Apparently, the state itself is not changed by the number operator and the number of quanta (in multiples of $\hbar\omega$) is given as the eigenvalue.

The fact that eigenstates form an orthonormal basis entails a normalization condition of the form:

$$\langle n | n' \rangle = \delta_{nn'} \quad \text{with} \quad \delta_{nn'} = \begin{cases} 1 & \text{if } n = n' \\ 0 & \text{if } n \neq n' \end{cases} \quad (2.19)$$

Let us now consider the annihilation operator acting on an arbitrary state $|n\rangle$

$$\hat{a} |n\rangle = c_n |n-1\rangle. \quad (2.20)$$

The normalization coefficient c_n can be determined by taking the inner product of the state $\hat{a} |n\rangle$ with itself and using Eqs. (2.18) and (2.19)

$$(\langle n | \hat{a}^\dagger)(\hat{a} |n\rangle) = \langle n | \hat{a}^\dagger \hat{a} |n\rangle = n \quad (2.21)$$

$$= \langle n-1 | c_n^* c_n |n-1\rangle = |c_n|^2, \quad (2.22)$$

which yields $c_n = \sqrt{n}$, and thus

$$\hat{a} |n\rangle = \sqrt{n} |n-1\rangle. \quad (2.23)$$

For the creation operator the calculation can be carried out analogously and we have

$$\hat{a}^\dagger |n\rangle = \sqrt{n+1} |n+1\rangle. \quad (2.24)$$

From the last result it can be shown that an arbitrary excited state $|n\rangle$ can be obtained by repeatedly applying the creation operator to the ground state $|0\rangle$

$$|n\rangle = \frac{(\hat{a}^\dagger)^n}{\sqrt{n!}} |0\rangle. \quad (2.25)$$

The states described by Eq. (2.25) are known as *number states* or *Fock states*.

2.2 Quantum fluctuations

In the preceding section it has been shown that the state $|n\rangle$ possesses a well-defined energy $E_n = \hbar\omega(n + \frac{1}{2})$. However, it is not a state with a well-defined electric field [2.1]. With the electric field operator $\hat{E}_x(z, t) = \mathcal{E}_0(\hat{a} + \hat{a}^\dagger) \sin(kz)$, the mean electric field of a Fock state can be determined to be

$$\langle n | \hat{E}_x(z, t) |n\rangle = \mathcal{E}_0 \sin(kz) [\langle n | \hat{a} |n\rangle + \langle n | \hat{a}^\dagger |n\rangle] = 0. \quad (2.26)$$

2.3

But for the energy density, which is related to the mean of the square of this field, we have

$$\langle n | \hat{E}_x^2(z, t) | n \rangle = 2\mathcal{E}_0^2 \sin^2(kz) \left(n + \frac{1}{2} \right). \quad (2.27)$$

These results can be used to compute the variance of the electric field. The variance of a quantity is a measure for its fluctuations and for an operator \hat{o} it is defined by

$$\text{Var}(\hat{o}) = \Delta^2 \hat{o} = \langle \hat{o}^2 \rangle - \langle \hat{o} \rangle^2. \quad (2.28)$$

The variance is the square of the standard deviation, which is given by

$$\Delta \hat{o} = \sqrt{\langle \hat{o}^2 \rangle - \langle \hat{o} \rangle^2}. \quad (2.29)$$

For a Fock state we obtain

$$\Delta \hat{E}_x = \sqrt{2} \mathcal{E}_0 \sin(kz) \left(n + \frac{1}{2} \right)^{1/2}. \quad (2.30)$$

by inserting the results from Eqs. (2.27) and (2.26) into Eq. (2.29). From Eq. (2.30) one can see that even when $n = 0$ the electric field is fluctuating. These fluctuations are the so-called *vacuum fluctuations*. They are a direct consequence of the non-vanishing energy of the ground state.

2.3 Quadrature operators and Heisenberg's Uncertainty Principle

The operators \hat{a} and \hat{a}^\dagger were useful to obtain the quantized Hamiltonian in Sec. 2.1. However, these operators are non-hermitian (since $\hat{a} \neq \hat{a}^*$ and $\hat{a}^\dagger \neq (\hat{a}^\dagger)^*$) and therefore do not represent observables of the light field. It is useful to introduce the so-called *quadrature operators*

$$\hat{X}_1 = \frac{1}{2}(\hat{a} + \hat{a}^\dagger) \quad (2.31)$$

$$\hat{X}_2 = \frac{1}{2i}(\hat{a} - \hat{a}^\dagger). \quad (2.32)$$

These hermitian operators are referred to as the *amplitude quadrature* (\hat{X}_1) and the *phase quadrature* (\hat{X}_2). With the quadrature operators, the electric field can be rewritten as

$$\hat{E}_x(z, t) \propto \sin(kz) [\hat{X}_1 \cos(\omega t) + \hat{X}_2 \sin(\omega t)]. \quad (2.33)$$

It is intelligible from Eq. (2.33) that the quadrature operators correspond to field amplitudes that oscillate 90° out of phase with respect to each other – they are in quadrature.

The quadrature operators do not commute as they obey the commutation relation

$$[\hat{X}_1, \hat{X}_2] = \frac{i}{2}. \quad (2.34)$$

Heisenberg's uncertainty principle states that for any two non-commuting observables there is a fundamental limit to the accuracy with which a simultaneous measurement on both quantities can be conducted. In other words, the more precise one observable is known, the less precise is the knowledge on the other. For two operators \hat{A} and \hat{B} with a non-vanishing commutator $[\hat{A}, \hat{B}] = C$, the uncertainty relation is given by

$$\Delta\hat{A}\Delta\hat{B} \geq \frac{1}{2}|C| \quad \text{or} \quad (2.35)$$

$$\Delta\hat{A}^2\Delta\hat{B}^2 \geq \frac{1}{4}|C|^2, \quad (2.36)$$

when expressed by the variances instead of the standard deviations. Together with Eq. (2.34) it follows for the quadrature operators that

$$\langle(\Delta\hat{X}_1)^2\rangle\langle(\Delta\hat{X}_2)^2\rangle \geq \frac{1}{16}. \quad (2.37)$$

For an arbitrary Fock state, the expectation value of the quadrature operators are

$$\langle n | \hat{X}_1 | n \rangle = \langle n | \hat{X}_2 | n \rangle = 0, \quad (2.38)$$

but for the squared operators they are given by

$$\langle n | (\hat{X}_1)^2 | n \rangle = \frac{1}{4} \langle n | \hat{a}^2 + \hat{a}^\dagger \hat{a}^\dagger + \hat{a}^\dagger \hat{a} + \hat{a} \hat{a}^\dagger | n \rangle \quad (2.39)$$

$$= \frac{1}{4} \langle n | \hat{a}^2 + \hat{a}^\dagger \hat{a}^\dagger + 2\hat{a}^\dagger \hat{a} + 1 | n \rangle \quad (2.40)$$

$$= \frac{1}{4}(2n + 1) \quad (2.41)$$

and

$$\langle n | (\hat{X}_2)^2 | n \rangle = \frac{1}{4}(2n + 1). \quad (2.42)$$

According to Eq. (2.28), this directly yields the variance

$$\langle(\Delta\hat{X}_1)^2\rangle = \frac{1}{4}(2n + 1) = \langle(\Delta\hat{X}_2)^2\rangle \quad (2.43)$$

of both quadratures. Evidently, the uncertainty is equally distributed between the two quadratures and is minimized by the vacuum state

$$\langle (\Delta \hat{X}_1)^2 \rangle_{n=0} = \frac{1}{4} = \langle (\Delta \hat{X}_2)^2 \rangle_{n=0}. \quad (2.44)$$

A state which minimizes Eq. (2.37) is a so-called *minimum-uncertainty state*. The value of 1/4 is referred to as the *vacuum noise variance*. Note that this value is the result of setting Planck's constant to a particular value [2.3], in this case $\hbar = 1/2$. Two other common definitions exist. The first ($\hbar = 1$) leads to the commutation relation $[\hat{X}'_1, \hat{X}'_2] = i$ and the corresponding uncertainty relation $\Delta \hat{X}'_1 \Delta \hat{X}'_2 \geq 1/4$, such that the vacuum variance is normalized to 1/2.

The second ($\hbar = 2$) results in a commutation relation of the form $[\hat{X}''_1, \hat{X}''_2] = 2i$, with the corresponding uncertainty relations $\Delta \hat{X}''_1 \Delta \hat{X}''_2 \geq 1$. Here the vacuum variance is normalized to 1.

2.4 Quantum states of light

2.4.1 Coherent states

The number states or Fock states introduced in Sec. 2.1 are indeed an adequate description of light, for example when dealing with single photon phenomena. However, for continuous-wave quantum optics experiments that usually employ laser light with a strong excitation, number states are an insufficient concept. This is easily seen by looking at the mean value of the electric field of a Fock state, which is $\langle n | \hat{E}_x | n \rangle = 0$ for all n . For the classical limit, i.e. for very large photon numbers, this does clearly not resemble the classical field which at a fixed point in space is a sinusoidal oscillation. The quantum states which are closest to a classical sinusoidal wave (such as a continuous-wave laser) are the so-called *coherent states* which were introduced by Ron. J. Glauber in 1963 [2.4]. The coherent states are denoted as $|\alpha\rangle$ and satisfy the eigenvalue relation [2.1]

$$\hat{a} |\alpha\rangle = \alpha |\alpha\rangle, \quad (2.45)$$

where α is a complex number. The expansion in the basis of Fock states yields

$$|\alpha\rangle = \sum_{n=0}^{\infty} C_n |n\rangle. \quad (2.46)$$

Inserted in the eigenvalue equation, Eq. (2.45), this gives

$$\hat{a} |\alpha\rangle = \sum_{n=1}^{\infty} C_n \sqrt{n} |n-1\rangle \quad (2.47)$$

$$= \alpha \sum_{n=0}^{\infty} C_n |n\rangle . \quad (2.48)$$

By equating coefficients one obtains

$$C_n \sqrt{n} = \alpha C_{n-1} , \quad (2.49)$$

which can be rearranged to obtain

$$C_n = \frac{\alpha}{\sqrt{n}} C_{n-1} \quad (2.50)$$

$$= \frac{\alpha^2}{\sqrt{n(n-1)}} C_{n-2} = \dots$$

$$= \frac{\alpha^n}{\sqrt{n!}} C_0 . \quad (2.51)$$

With this result one can rewrite Eq. (2.46) as

$$|\alpha\rangle = C_0 \sum_{n=0}^{\infty} \frac{\alpha^n}{\sqrt{n!}} |n\rangle . \quad (2.52)$$

The states $|\alpha\rangle$ have to fulfill the normalization condition $\langle\alpha|\alpha\rangle = 1$. With the normalization condition, the constant C_0 can be determined and one obtains

$$|\alpha\rangle = e^{-\frac{1}{2}|\alpha|^2} \sum_{n=0}^{\infty} \frac{\alpha^n}{\sqrt{n!}} |n\rangle . \quad (2.53)$$

In the above argument the coherent states emerged from being eigenstates of the annihilation operator. However, other ways to define a coherent state exist. For example, one can introduce the *displacement operator* \hat{D} , which is given by

$$\hat{D}(\alpha) = \exp(\alpha \hat{a}^\dagger - \alpha^* \hat{a}) . \quad (2.54)$$

A coherent state can then be produced by applying \hat{D} to the vacuum [2.1]

$$\begin{aligned} |\alpha\rangle &= \hat{D}(\alpha) |0\rangle \\ &= e^{-\frac{1}{2}|\alpha|^2} \sum_{n=0}^{\infty} \frac{\alpha^n}{\sqrt{n!}} |n\rangle . \end{aligned} \quad (2.55)$$

The meaning of the complex parameter α (where $\alpha = |\alpha|e^{i\Theta}$) becomes clear when looking at the expectation value of the number operator $\hat{n} = \hat{a}^\dagger \hat{a}$ which is given by

$$n = \langle \alpha | \hat{n} | \alpha \rangle = |\alpha|^2 . \quad (2.56)$$

Thus, $|\alpha|^2$ is the mean number of photons present in the excitation of the coherent state. To determine the fluctuations of the photon number, one needs to evaluate the expectation value of \hat{n}^2 . It is given by

$$\begin{aligned} \langle \alpha | \hat{n}^2 | \alpha \rangle &= \langle \alpha | \hat{a}^\dagger \hat{a} \hat{a}^\dagger \hat{a} | \alpha \rangle \\ &= |\alpha|^4 + |\alpha|^2 \\ &= n^2 + n \end{aligned} \quad (2.57)$$

and thus

$$\Delta^2 n = \langle \hat{n}^2 \rangle - \langle \hat{n} \rangle^2 = n , \quad (2.58)$$

which is characteristic of a Poisson process. For any coherent state $|\alpha\rangle$, it can be shown that

$$\langle (\Delta(\hat{X}_1))^2 \rangle_\alpha = \frac{1}{4} = \langle (\Delta(\hat{X}_2))^2 \rangle_\alpha . \quad (2.59)$$

Again, the fluctuations are distributed symmetrically between the amplitude and the phase quadrature. In contrast to the Fock states, a coherent state of light has fluctuations equal to the vacuum fluctuations for any arbitrary excitation α ; and hence all coherent states are minimum-uncertainty states.

A useful way to visualize quantum states is the coordinate system spanned by the two quadratures, the so-called *phase-space*. The phase-space picture (also called *quantum phasor* or *ball-on-stick* picture) is a combination of the classical phasor picture with the quantum noise properties of light. In phase-space, a classical electromagnetic wave would correspond to a well-defined point that rotates around the origin at the carrier frequency and whose distance from the origin (the length of the phasor) is the amplitude. From Eq. (2.37) it is obvious that a quantum state *cannot* be related to such a well-defined point. Merely a probability with an area of uncertainty which is defined by the Heisenberg uncertainty principle can be given. Figure 2.1 shows the illustration of a coherent state and of the vacuum state in the phase-space picture .

2.4.2 Squeezed states of light

One can introduce the generic quadrature operator $\hat{X}(\theta)$ as

$$\hat{X}(\theta) = \frac{1}{2} \left(\hat{a} e^{-i\theta} + \hat{a}^\dagger e^{i\theta} \right) . \quad (2.60)$$

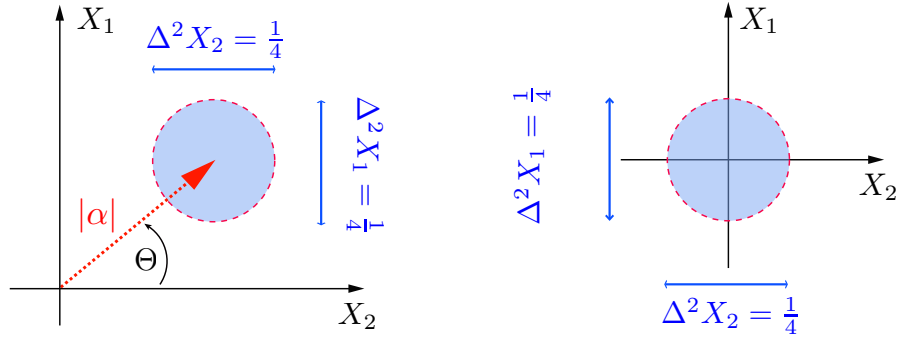


Figure 2.1 — Phase-space illustrations of a coherent state $|\alpha\rangle$ of amplitude $|\alpha|$ and phase angle Θ (left) and of a vacuum state (right) for which $|\alpha| = 0$.

By evaluating $\hat{X}(\theta)$ for two quadrature angles $\theta = 0$ and $\theta = \pi/2$, one obtains the amplitude quadrature $\hat{X}_1 = \hat{X}(0)$ and phase quadrature $\hat{X}_2 = \hat{X}(\pi/2)$. Consequently, \hat{X}_1 and \hat{X}_2 can be used to express the generic quadrature operator as a linear combination

$$\hat{X}(\theta) = \hat{X}_1 \cos \theta + \hat{X}_2 \sin \theta. \quad (2.61)$$

A state is said to be *quadrature squeezed* if

$$\langle [\Delta \hat{X}(\theta)]^2 \rangle < \frac{1}{4} \quad \text{for some angle } \theta. \quad (2.62)$$

Equation (2.62) states that for a state to be squeezed the uncertainty in one quadrature needs to be smaller than the uncertainty of a coherent or vacuum state. Still, Heisenberg's uncertainty principle, Eq. (2.36), has to be satisfied, which implies that the uncertainty in the orthogonal quadrature increases.

Being more specific and considering the operators of the amplitude and phase quadrature, a state is squeezed if

$$\Delta^2 \hat{X}_1 < \frac{1}{4} \quad (\text{amplitude squeezed}) \quad (2.63)$$

$$\text{or } \Delta^2 \hat{X}_2 < \frac{1}{4} \quad (\text{phase squeezed}). \quad (2.64)$$

A squeezed state can be generated mathematically through the action of the (unitary) *squeeze operator* defined as [2.1]

$$\hat{S}(\zeta) = \exp \left[\frac{1}{2} (\zeta^* \hat{a} \hat{a} - \zeta \hat{a}^\dagger \hat{a}^\dagger) \right], \quad (2.65)$$

where $\xi = re^{i\phi}$. The parameter r is the *squeeze parameter* with $0 \leq r < \infty$ and ϕ is a phase with $0 \leq \phi \leq 2\pi$. Now let us consider the action of this operator $\hat{S}(\xi)$ to the state $|\psi\rangle$

$$|s\rangle = \hat{S}(\xi) |\psi\rangle . \quad (2.66)$$

In order to determine the variances of \hat{X}_1 and \hat{X}_2 , the expectation values of the annihilation and creation operator are required. One can make use of the following properties that are obtained from an application of the Baker-Campbell-Hausdorff formula [2.5]

$$\hat{S}^\dagger(\xi) \hat{a} \hat{S}(\xi) = \hat{a} \cosh(r) - \hat{a}^\dagger e^{i\phi} \sinh(r), \quad (2.67)$$

$$\hat{S}^\dagger(\xi) \hat{a}^\dagger \hat{S}(\xi) = \hat{a}^\dagger \cosh(r) - \hat{a} e^{-i\phi} \sinh(r) . \quad (2.68)$$

Using that $\hat{S}(\xi)$ is a unitary operator, $\hat{S}(\xi) \hat{S}^\dagger(\xi) = \mathbb{1}$, and restricting the consideration to the special case of the squeeze operator acting on the vacuum state $|0\rangle$, it follows for the variances [2.1]

$$\begin{aligned} \langle \Delta^2 \hat{X}_1 \rangle_\xi &= \frac{1}{4} \left[\cosh^2(r) + \sinh^2(r) - 2 \sinh(r) \cosh(r) \cos(\phi) \right] \\ &= \frac{1}{4} \left[\sin^2 \left(\frac{\phi}{2} \right) e^{2r} + \cos^2 \left(\frac{\phi}{2} \right) e^{-2r} \right] , \end{aligned} \quad (2.69)$$

$$\begin{aligned} \langle \Delta^2 \hat{X}_2 \rangle_\xi &= \frac{1}{4} \left[\cosh^2(r) + \sinh^2(r) + 2 \sinh(r) \cosh(r) \cos(\phi) \right] \\ &= \frac{1}{4} \left[\cos^2 \left(\frac{\phi}{2} \right) e^{2r} + \sin^2 \left(\frac{\phi}{2} \right) e^{-2r} \right] . \end{aligned} \quad (2.70)$$

The squeezing angle ϕ determines the quadrature that is squeezed. For $\phi = 0$, Eqs. (2.69) and (2.70) reduce to

$$\langle \Delta^2 \hat{X}_1 \rangle_\xi = \frac{1}{4} e^{-2r} \quad \text{and} \quad (2.71)$$

$$\langle \Delta^2 \hat{X}_2 \rangle_\xi = \frac{1}{4} e^{2r} . \quad (2.72)$$

Evidently, when $\phi = 0$ squeezing is present in the amplitude quadrature \hat{X}_1 . When setting $\phi = \pi$, the squeezing will appear in the phase quadrature \hat{X}_2 . From Eqs. (2.71) and (2.72) it can be seen that the uncertainty principle is satisfied: when the noise in one quadrature is squeezed below the vacuum noise, other quadrature exhibits noise above the vacuum noise level, we say it is *anti-squeezed*. The phase-space pictures for an amplitude squeezed state and for a phase squeezed state, respectively, are shown

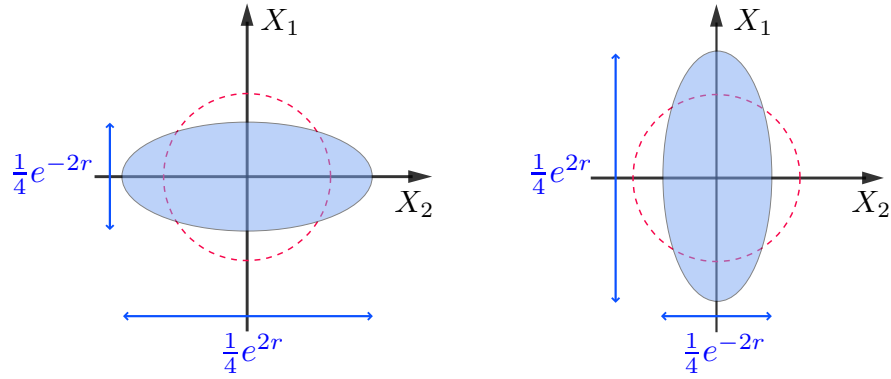


Figure 2.2 — Phase-space picture of squeezed vacuum states. Left: illustration of an amplitude squeezed vacuum state. The uncertainty in the X_1 -quadrature is squeezed by the factor $\exp(-2r)$ while the X_2 -quadrature is anti-squeezed by the factor $\exp(2r)$, both relative to the vacuum uncertainty of $1/4$. Right: corresponding illustration of a phase squeezed vacuum state.

in Fig.2.2. Pure squeezed states equalize the uncertainty relation; they are minimum uncertainty states. However, this is not a necessity, and as we shall see later, it is usually not the case under experimental conditions since optical loss will degrade the purity of the states.

When a different choice is made for the angle ϕ , it is useful to introduce rotated quadrature operators

$$\begin{pmatrix} \hat{Y}_1 \\ \hat{Y}_2 \end{pmatrix} = \begin{pmatrix} \cos(\phi/2) & \sin(\phi/2) \\ -\sin(\phi/2) & \cos(\phi/2) \end{pmatrix} \begin{pmatrix} \hat{X}_1 \\ \hat{X}_2 \end{pmatrix}. \quad (2.73)$$

Analogously it can be shown for these new operators that

$$\langle \Delta^2 \hat{Y}_1 \rangle_{\xi} = \frac{1}{4} e^{-2r} \quad \text{and} \quad (2.74)$$

$$\langle \Delta^2 \hat{Y}_2 \rangle_{\xi} = \frac{1}{4} e^{2r}. \quad (2.75)$$

Squeezing and anti-squeezing are therefore not restricted to the amplitude and phase quadrature, respectively, but can appear along any two orthogonally oriented quadratures.

So far, only the special case of squeezed vacuum states was considered. A more general squeezed state can be obtained by letting the displacement operator act on a squeezed vacuum state

$$|\alpha, \xi\rangle = \hat{D}(\alpha) \hat{S}(\xi) |0\rangle. \quad (2.76)$$

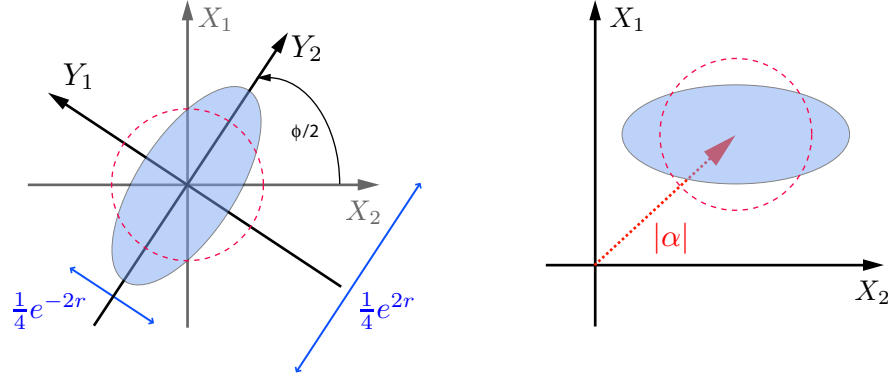


Figure 2.3 — Left: Phase-space picture of the squeezed vacuum state with squeezing along an arbitrary axis Y_1 which is rotated by $\phi/2$. Right: Displaced squeezed state with squeezing in the amplitude quadrature and coherent excitation α

Obviously, a coherent state is obtained if $\xi = 0$. To determine the average photon number in such a state, one needs to evaluate the expectation value of the number operator

$$\langle \alpha, \xi | \hat{n} | \alpha, \xi \rangle = |\alpha|^2 + \sinh^2(r). \quad (2.77)$$

It is clear that $r = 0$ yields the mean photon number of the coherent state [compare Eq. 2.56)] and $\alpha = 0$ yields the corresponding value for the squeezed vacuum state. Furthermore, Eq. (2.77) illustrates that the process of squeezing produces photons since the expectation value of \hat{n} is increased by $\sinh^2(r)$. Calculating the variances of the quadrature operators of the state once again gives

$$\langle \Delta^2 \hat{Y}_1 \rangle_{\xi} = \frac{1}{4} e^{-2r} \quad \text{and} \quad (2.78)$$

$$\langle \Delta^2 \hat{Y}_2 \rangle_{\xi} = \frac{1}{4} e^{2r}, \quad (2.79)$$

which shows that the coherent excitation α does not alter the quantum noise characteristic of the *displaced squeezed state*. The phase-space illustrations for the vacuum state with squeezing along an arbitrary quadrature and the according picture for a displaced squeezed state are depicted in Fig.2.3.

2.5 State representation

2.5.1 The density operator

The density operator completely describes an ensemble (mixture) of quantum states as being made up of individual pure states, and the probabilities with which they are likely to be found. It is defined as

$$\hat{\rho} = \sum_i p_i |\Psi_i\rangle \langle \Psi_i| , \quad (2.80)$$

where p_i is the probability of finding the system in the state $|\Psi_i\rangle$. For an operator \hat{o} , the expectation value is given by

$$\langle \hat{o} \rangle = \text{Tr}(\hat{o}\hat{\rho}) . \quad (2.81)$$

The probabilities naturally obey $0 \leq p_i \leq 1$, $\sum_i p_i = 1$, and $\sum_i p_i^2 \leq 1$. From that some important properties of the density operator follow, such as the normalization condition

$$\text{Tr}(\hat{\rho}) = \sum_i p_i = 1 \quad (2.82)$$

and the purity condition which holds for a pure state with $\hat{\rho} = |\Psi\rangle \langle \Psi|$

$$\hat{\rho}^2 = |\Psi\rangle \langle \Psi| |\Psi\rangle \langle \Psi| = \hat{\rho} , \quad (2.83)$$

and thus

$$\text{Tr}(\hat{\rho}) = \text{Tr}(\hat{\rho}^2) = 1 . \quad (2.84)$$

Likewise it can be shown that for a mixed state

$$\text{Tr}(\hat{\rho}^2) < 1 . \quad (2.85)$$

Consequently, the trace of the square of the density operator is a measure for the purity of the quantum state. In terms of the number states the density operator can be written as

$$\hat{\rho} = \sum_n \sum_m |m\rangle \rho_{nm} \langle n| . \quad (2.86)$$

The knowledge of all elements ρ_{nm} of the density matrix is necessary to determine the operator $\hat{\rho}$. In order to calculate the density matrix elements ρ_{nm} for a single-mode

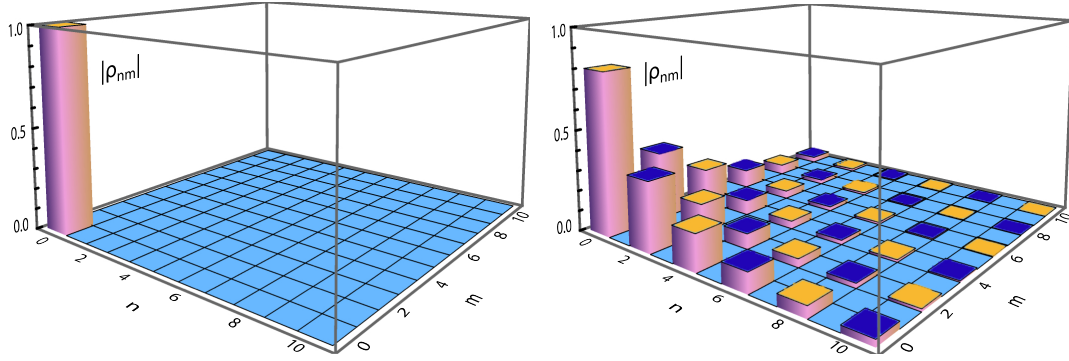


Figure 2.4 — Plot of the density matrix elements ρ_{nm} for the vacuum state (left) and for a squeezed vacuum state (right) with a squeezing factor $r = 0.7$ which corresponds to squeezing (anti-squeezing) of -6 dB (6 dB). The illustration is truncated at $n = m = 10$; dark blue entries indicate negative values.

(squeezed) vacuum state, one can follow the prescription given in [2.6]. With the definitions

$$\tilde{V}_x = V_x + 1/2, \quad (2.87)$$

$$\tilde{V}_p = V_p + 1/2, \quad (2.88)$$

$$U = 1 - \frac{1}{2\tilde{V}_x} - \frac{1}{2\tilde{V}_p} \quad \text{and} \quad (2.89)$$

$$T = \frac{1}{4\tilde{V}_x} - \frac{1}{4\tilde{V}_p} \quad (2.90)$$

the entries can be obtained using the equation

$$\rho_{nm} = \sqrt{\frac{m!n!}{\tilde{V}_x\tilde{V}_p}} \sum_a \frac{(-T)^{[(m-n)/2]+2a} U^{n-2a}}{a!(n-2a)! (a + \frac{m-n}{2})!}, \quad (2.91)$$

if $m + n$ is even, and $\rho_{m,n} = 0$ if $m + n$ is odd. Note that V_x and V_p correspond to the linear quadrature variances of the quantum state as introduced in Eq. (2.37), but with the vacuum variance set to $1/2$. This expression for the density matrix in the Fock state basis can be derived from the covariance matrix by first noting that the Husimi Q-function in the coherent state basis is the generating function for the density matrix in the Fock state basis [2.6]. The covariance matrix needs to be transformed from the quadrature basis into the coherent basis to obtain the above formula. The density matrices for the vacuum state and for a squeezed vacuum state (with 6 dB of squeezing) are illustrated in Fig. (2.4). The photon numbers n and m range from zero

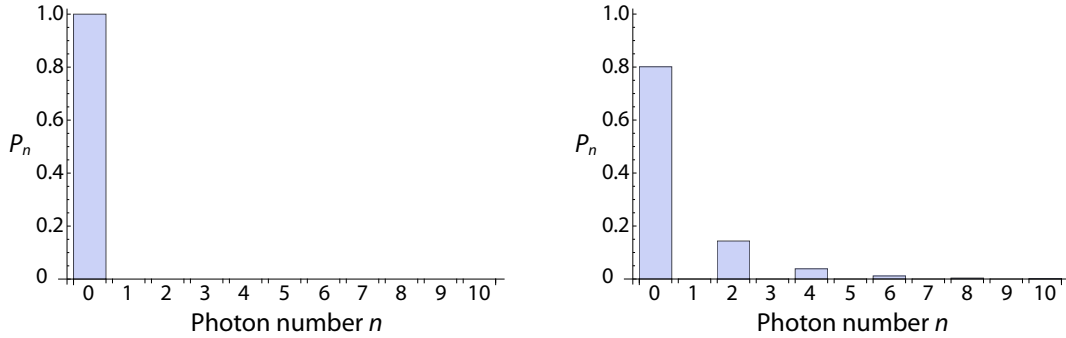


Figure 2.5 — Plot of the diagonal elements of the density matrix elements ρ_{nm} for $n = 0, 1, \dots, 10$ which correspond to the probabilities P_n of finding n photons. Left: vacuum state. Right: squeezed vacuum state with a squeezing factor $r = 0.7$ which corresponds to squeezing (anti-squeezing) of -6 dB (6 dB).

to 10. In principle, the Fock basis is infinitely large, but the values of the entries of the density matrix decrease rapidly with the photon number.

The diagonal elements of the density matrix ρ_{nm} give the probabilities P_n of finding a certain number n of photons in the field, that is

$$P_n = \rho_{nn}. \quad (2.92)$$

For pure (squeezed) vacuum states with photon numbers $n = 0, 1, 2, \dots$ these probabilities can be determined to be [2.1]

$$P_{2n} = \frac{(2n)!}{2^{2n}(n!)^2} \frac{(\tanh r)^{2n}}{\cosh r}, \quad (2.93)$$

where r is the squeeze parameter as introduced in Eq. (2.65), and

$$P_{2n+1} = 0. \quad (2.94)$$

As can be seen in Fig. (2.5), the photon number distribution clearly shows an oscillatory behavior, with vanishing probabilities for all odd-valued n . This is only true for a pure squeezed vacuum state and, as we will see later, odd photon numbers will occur when the purity of the state decreases. The vacuum state contains zero photons on average, and hence the probability to measure no photon is equal to one. As mentioned before, the process of squeezing generates photons (see Eq. (2.77)), and consequently there is a certain probability to detect photon numbers larger than zero for the squeezed vacuum state.

2.5.2 Wigner function

The density operator can be used to define the Wigner function for two conjugate variables (here the position q and the momentum p) as [2.1]

$$W(q, p) = \frac{1}{2\pi\hbar} \int e^{ipx/\hbar} \left\langle q + \frac{x}{2} \left| \hat{\rho} \right| q - \frac{x}{2} \right\rangle dx, \quad (2.95)$$

where $\hat{\rho}$ is the density operator of an arbitrary (quantum) state. In terms of the amplitude and phase quadrature, the Wigner function can be expressed as

$$W(X_1, X_2) = \frac{1}{2\pi\sqrt{V_1 V_2}} \exp \left[-\frac{1}{2} \left(\frac{(X_1 - x_1)^2}{V_1} + \frac{(X_2 - x_2)^2}{V_2} \right) \right], \quad (2.96)$$

where $V_1 = \Delta^2 X_1$ and $V_2 = \Delta^2 X_2$ are the variances of the amplitude and phase quadrature, respectively. The Wigner function, first introduced by Eugene Wigner in 1932 [2.7], is a quasi-probability distribution in phase-space. The term "quasi" stems from the fact that the Wigner function does not always reflect physical probability densities, as it can also take on negative values. It is the projection of the Wigner function onto an arbitrary quadrature that results in a true probability density for that respective quadrature. For a coherent state, the Wigner function is given by [2.8]

$$W(X_1, X_2) = \frac{2}{\pi} \exp \left(-2[(X_1 - x_1)^2 + (X_2 - x_2)^2] \right), \quad (2.97)$$

where $x_{1,2}$ correspond to the displacements in phase-space with the coherent excitation $|\alpha\rangle = \sqrt{(x_1^2 + x_2^2)}$. As already shown, the noise characteristics of coherent states and of the vacuum state are the same and independent of $|\alpha|$. Therefore, setting $x_1 = x_2 = 0$ yields the Wigner function of the vacuum state. The Wigner function of the vacuum state and the Wigner function of a coherent state are depicted in Fig. (2.6). Note that the normalization pre-factors in Eq. (2.97), and consequently the value of W , depend on the definition of the vacuum level. In Fig. (2.7), the more general form of the Wigner function, Eq. (2.96), was used to plot the Wigner function for two squeezed vacuum states: one with squeezing in the X_1 quadrature (left) and the other with squeezing in the X_2 quadrature (right). For each state the uncertainty in the squeezed quadrature is decreased by a factor of 4 (corresponding to -6 dB or a squeeze parameter $r = 0.7$) relative to the vacuum uncertainty of $1/4$. The states are pure and therefore the uncertainty in the anti-squeezed quadrature is increased by the same factor. As mentioned above, in order to extract a real probability distribution from the Wigner function, one has to carry out the integration over one quadrature. For instance, integrating the coherent state's Wigner function over the phase quadrature

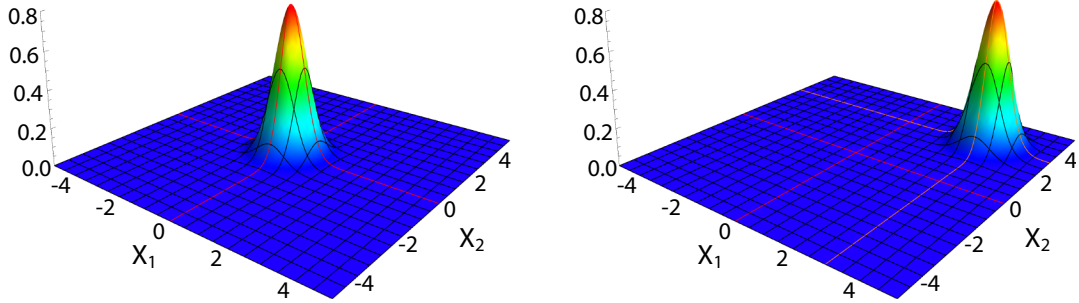


Figure 2.6 — Wigner function of the vacuum state (left) and of a dim coherent state (right) which is displaced by $x_1 = x_2 = 3$.

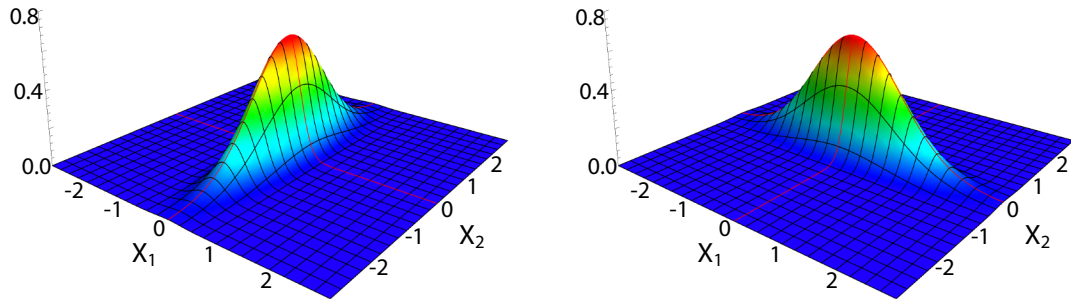


Figure 2.7 — Wigner function of a squeezed vacuum state. Left: amplitude squeezed state. Right: phase squeezed state. The uncertainty in the squeezed (anti-squeezed) quadrature is decreased (increased) by a factor of 4, corresponding to 6 dB or to a squeeze parameter $r = 0.7$, relative to the vacuum uncertainty of $1/4$.

X_2 yields the probability density function for the amplitude quadrature X_1

$$P(X_1) = \int_{-\infty}^{\infty} W(X_1, X_2) dX_2 \quad (2.98)$$

$$= \frac{2}{\pi} e^{-2(X_1 - x_1)^2} \int_{-\infty}^{\infty} e^{-2(X_2 - x_2)^2} dX_2 \quad (2.99)$$

$$= \sqrt{\frac{2}{\pi}} e^{-2(X_1 - x_1)^2}, \quad (2.100)$$

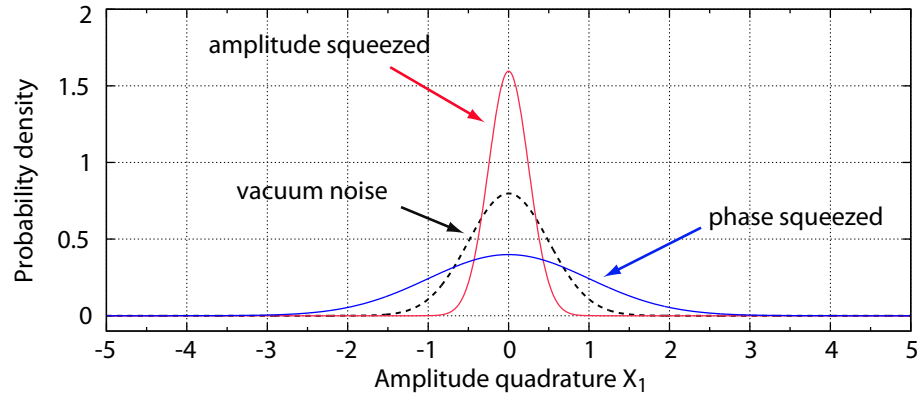


Figure 2.8 — Probability density distribution of the X_1 quadrature obtained from the projection of the Wigner function, that is, by integration over X_2 . From top to bottom: amplitude squeezed vacuum state, vacuum state, and phase squeezed vacuum state. The squeezing factor was again chosen to be -6 dB and the variance of the vacuum state was $1/4$.

where $\int_{-\infty}^{\infty} \exp(-cx^2)dx = \sqrt{\pi/c}$ was used. In the same manner one obtains the probability density for the phase quadrature

$$P(X_2) = \int_{-\infty}^{\infty} W(X_1, X_2) dX_1 \quad (2.101)$$

$$= \sqrt{\frac{2}{\pi}} e^{-2(X_2 - x_2)^2} . \quad (2.102)$$

Equations (2.100) and (2.102) are gaussian probability distributions with a variance of $1/4$ and mean values x_1 and x_2 , respectively. For a squeezed vacuum state with quadrature variances V_i ($i = 1, 2$) one finds

$$P(X_i) = \frac{1}{\sqrt{2\pi V_i}} e^{-\frac{(X_i - x_i)^2}{2V_i}} . \quad (2.103)$$

This is again a gaussian probability function with mean value x_i , but with the variance V_i . A plot of three projections onto the amplitude quadrature X_1 is shown in Fig. (2.8). Once more, it was assumed that the squeezed quadrature (top trace) has a factor of 4 less uncertainty than the vacuum (dashed trace). As a consequence, the phase-squeezed state exhibits anti-squeezing in the X_1 quadrature being 4 times larger than the vacuum uncertainty.

From Eq. (2.97) it is evident that knowing the variances of the amplitude and phase quadrature in principle is sufficient to infer the Wigner function. Note that this is true

only for *gaussian states* for which the fluctuations of the generic quadrature operator $\delta\hat{X}^\theta$ obey a gaussian probability distribution for all quadrature angles θ . A means to get more complete information about the Wigner function is quantum-state tomography. Quantum-state tomography makes use of the fact that the probability distributions $P_\theta(X_\theta)$ can be obtained from the projections of the Wigner function at different angles. $W(X_1, X_2)$ can then be obtained by back-projection via the inverse Radon transform [2.9]. The set of P_θ can be acquired by stepwise measuring the variance V_θ of the generic quadrature operator as introduced in Eq. (2.61) with $0 \leq \theta \leq \pi$. Such measurements can be conducted by means of a so-called *homodyne detector* which will be discussed in more detail in Sec. 3.2. Details on optical tomography of quantum states can be found, for example, in [2.10, 2.11].

2.5.3 Covariance matrix

For gaussian states, the covariance matrix is another complete description of a state. It is fully determined by the variances of the amplitude and phase quadratures. For multiple party systems, this can be generalized for all quadrature variances of the single parties and the covariances of all possible combinations of the quadratures. The covariance matrix is given by

$$\zeta_{ij} = \text{Cov}(\zeta_i, \zeta_j) , \quad (2.104)$$

where $\hat{\zeta} = (\hat{X}_1^A, \hat{X}_2^A, \hat{X}_1^B, \hat{X}_2^B, \dots)$ is a $2n$ -dimensional vector with the number of parties n and the covariance $\text{Cov}(X, Y)$ is defined as

$$\text{Cov}(X, Y) = \langle XY \rangle - \langle X \rangle \langle Y \rangle . \quad (2.105)$$

The covariance is a generalization of the variance since $\text{Var}(X) = \text{Cov}(X, X)$. In terms of the covariance matrix, the Wigner function can be written as

$$W(\zeta) = \frac{1}{(2\pi)^n \sqrt{\det\zeta}} \exp \left[-\frac{1}{2} \zeta \zeta^{-1} \zeta^T \right] , \quad (2.106)$$

with $\det\zeta$ being the determinant of ζ and n the dimension of the covariance matrix.

2.5.4 Purity

So far, only pure states, that is states that minimize the Heisenberg uncertainty principle were considered. However, optical loss in the experimental setup will entail

a decrease in purity, since (as we will see in Sec. 3.3.1) the effect of optical loss essentially corresponds to mixing the state with the vacuum. The purity is defined as

$$\mu = \text{Tr}(\rho^2), \quad (2.107)$$

where ρ is the density matrix. For a squeezed vacuum state, the density matrix in the Fock state basis has an infinite number of dimensions. It is therefore useful to redefine the purity as a function of the covariance matrix

$$\mu = \frac{1}{\sqrt{4^n \det \zeta}}. \quad (2.108)$$

The factor of four is due to the normalization to the vacuum noise of $1/4$ and n is the dimension of the covariance matrix. For a squeezed vacuum state, the covariance matrix is a 2×2 -matrix. With the choice of a suitable basis, the off-diagonal elements vanish and the entries on the main diagonal contain the variances of the amplitude and phase quadrature, respectively. The covariance matrix of a squeezed vacuum state is then given by

$$\zeta = \begin{pmatrix} V_1 & 0 \\ 0 & V_2 \end{pmatrix}, \quad (2.109)$$

and the expression for the purity simplifies to

$$\mu = \frac{1}{4\sqrt{V_1 V_2}}. \quad (2.110)$$

References

- [2.1] C. C. Gerry and P. L. Knight, *Introductory Quantum Optics* (Cambridge Univ. Press, Cambridge, 2004).
- [2.2] W. Heisenberg, "Über den anschaulichen Inhalt der quantentheoretischen Kinematik und Mechanik," *Zeitschrift für Physik* **43**, 172–198 (1927).
- [2.3] C. Weedbrook, S. Pirandola, R. Garcia-Patron, N. J. Cerf, T. C. Ralph, J. H. Shapiro, S. Lloyd, "Gaussian Quantum Information," arXiv:1110.3234v1 (2011).
- [2.4] R.J. Glauber, "Coherent and incoherent states of radiation field," *Phys. Rev.* **131**, 2766–2788 (1963).

- [2.5] H. F. Baker, "On the Calculation of the Finite Equations of a Continuous Group," Proc. Lond. Math. Soc., S. 332 (1902).
- [2.6] P. Marek *et al.*, "Multiple-copy distillation and purification of phase-diffused squeezed states," Phys. Rev. A **76**, 053820 (2007).
- [2.7] E. Wigner, "On the Quantum Correction For Thermodynamic Equilibrium", Phys. Rev. **49**, 7 49–759 (1932).
- [2.8] D. F. Walls, and G. J. Milburn, *Quantum Optics* (Springer, 2004).
- [2.9] K. Vogel, and H. Risken, "Determination of quasiprobability distributions in terms of probability distributions for the rotated quadrature phase," Phys. Rev. A **40**, 2847–2849 (1989).
- [2.10] G. Breitenbach, S. Schiller, and J. Mlynek, "Measurement of the quantum states of light," Nature **387**, 471–475 (1997).
- [2.11] B. Hage, *Quantentomographische Charakterisierung gequetschter Zustände*, Diplomarbeit. Universität Hannover (2004).

Generation and detection of squeezed states

3.1 Generation of squeezed quantum noise

Various ways to generate squeezed light experimentally exist. The experiments presented in this thesis are, however, entirely based on degenerate parametric down-conversion, a process belonging to the class of so-called second-order nonlinear interactions.

3.1.1 Second-order nonlinear interactions

When light propagates through a dielectric material, a certain macroscopic polarization can be induced. This polarization describes the response of the medium's loosely bound valence electrons to the disturbance of the traversing electric field. Assuming a driving electric field E the polarization can be written as

$$\mathcal{P} = \varepsilon_0 \left(\chi^{(1)}E + \chi^{(2)}E^2 + \chi^{(3)}E^3 + \dots \right) , \quad (3.1)$$

where ε_0 is the permittivity of the vacuum and $\chi^{(n)}$ is the n -th order susceptibility of the medium. The term $\chi^{(1)}$ is the linear susceptibility and is connected to the refractive index $n = \sqrt{1 + \chi^{(1)}}$. Typically, $\chi^{(1)} \sim 1$. The value of the second-order nonlinear susceptibility is much smaller, for example, $\chi^{(2)} \sim 10^{-10}$ – 10^{-13} mV⁻¹ for a medium with a relatively high second-order susceptibility. The class of interaction processes based on the $\chi^{(2)}$ term can be divided into two complementary categories:

up-conversion processes, in which two low-frequency photons are converted into one photon of high frequency; or *down-conversion* processes, where one photon of high frequency is converted into two low-frequency photons.

The need for energy conservation leads to constraints for the light fields participating in a $\chi^{(2)}$ process. Let us denote the low-frequency photons with indices 1,2 and let the high-frequency photon have the index 3. As a consequence of energy conservation, for all processes the frequencies have to fulfill

$$\omega_1 + \omega_2 = \omega_3 . \quad (3.2)$$

For the experiments presented in this thesis, only two special cases of $\chi^{(2)}$ processes were used. First, second-harmonic generation (SHG) which probably is the simplest and most widely used up-conversion process. In SHG, the two low-frequency photons have exactly the same (fundamental) frequency ($\omega_1 = \omega_2 = \omega_f$), and consequently the up-converted field is at twice the fundamental frequency ($\omega_3 = 2\omega_f$). Second, degenerate parametric down-conversion, where the high-frequency photon converts into two photons of exactly half the frequency ($\omega_1 = \omega_2 = \omega_3/2$). Obviously these are two complementary processes. As we shall see shortly, degenerate parametric down-conversion can be used to produce squeezing, while the necessary pump field needs to be generated by SHG. Note that parametric down-conversion is frequently referred to as optical parametric amplification (OPA). The process of SHG is the degenerate case of the more general sum-frequency generation (SFG). Accordingly, degenerate OPA also has its more general extensions.

The even smaller $\chi^{(3)}$ term in Eq. (3.1) is linked to third order effects such as the optical Kerr effect, Four Wave Mixing, and third-harmonic generation.

3.1.2 Phase matching

For the total momentum of the involved light fields ($p_i = \hbar k_i$) to be conserved, it follows for their wave vectors that

$$k_1 + k_2 = k_3 , \quad (3.3)$$

where the wave vectors are given by

$$k_i = \frac{\omega_i}{c_i} . \quad (3.4)$$

The propagation velocity c_i within the medium, also called the phase velocity of the respective field, is given by

$$c_i = \frac{c}{n(\omega_i)} , \quad (3.5)$$

with c being the speed of light in free space and the frequency dependent index of refraction $n(\omega_i)$. One can introduce the phase mismatch parameter $\Delta k = k_1 + k_2 - k_3$. For SHG and degenerate OPA we have $\omega_1 = \omega_2 = \omega_3/2$ and thus the requirement from Eq. (3.3) becomes

$$n(\omega_1) = n(\omega_3). \quad (3.6)$$

In the case this is fulfilled ($\Delta k = 0$), that is the refractive indices are equal for both fundamental and harmonic field, the two fields propagate at the same velocity. Consequently, the relative phase between both fields stays constant. We say the system is *phase matched*. A deviation from optimum phase matching will decrease the efficiency of the nonlinear coupling. Most dielectric media are dispersive so in general the phase matching condition is not satisfied and $\Delta k \neq 0$. Different techniques that can be applied to bring a system to (or at least very close) to $\Delta k = 0$ exist. Note that perfect phase matching can only be obtained for plane waves. Within the field of SHG and OPA the two techniques that are mainly applied are birefringent phase matching (BPM) and quasi phase matching (QPM). These were also used for the experiments presented in this thesis.

3.1.3 Squeezed light from parametric down-conversion

In the process of degenerate parametric down-conversion, that is also referred to as *degenerate optical parametric amplification*, a pump field \hat{b} of frequency ω_p is incident on a nonlinear medium. In the course of the nonlinear interaction, pairs of photons with identical optical frequencies ($\omega = \omega_p/2$) are generated from the pump field. The Hamilton operator for such a process reads [3.1]

$$\hat{H} = \hbar\omega\hat{a}^\dagger\hat{a} + \hbar\omega_p\hat{b}^\dagger\hat{b} + i\hbar\chi^{(2)}(\hat{a}\hat{a}\hat{b}^\dagger - \hat{a}^\dagger\hat{a}^\dagger\hat{b}), \quad (3.7)$$

where \hat{a} is the *signal field* consisting of the down-converted photons, and $\chi^{(2)}$ is the second order nonlinear susceptibility describing the coupling strength depending on the medium. Let us suppose that the intensity of the pump field is much larger than the intensity of the signal field. We then can assume that the pump is in a classical state and that the depletion of the pump field due to the down-conversion process is negligible. Further we assume the pump field \hat{b} to be described by a coherent state. Including the time evolution one can write $|\beta e^{-i\omega_p t}\rangle$. Consequently, \hat{b} and \hat{b}^\dagger can be approximated as $\beta e^{-i\omega_p t}$ and $\beta^* e^{i\omega_p t}$, respectively. Thus, for the approximated Hamilton operator we have [3.1]

$$\hat{H} = \hbar\omega\hat{a}^\dagger\hat{a} + i\hbar\chi^{(2)}(\beta^*\hat{a}\hat{a}e^{i\omega_p t} - \beta\hat{a}^\dagger\hat{a}^\dagger e^{-i\omega_p t}). \quad (3.8)$$

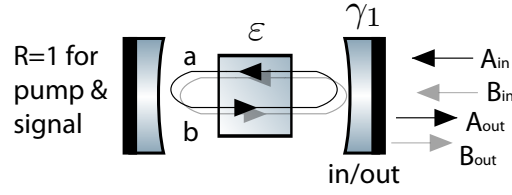


Figure 3.1 — Illustration of the single-ended cavity used to model the degenerate parametric down-conversion below threshold. A nonlinear medium is enclosed between two mirrors. The left mirror has perfect reflectivity for both the signal field and the pump field. The coupling mirror has perfect transmission for the pump and a certain reflectivity for the signal field. The cavity loss rate γ_1 is related to the cavity linewidth. The nonlinear interaction is described by $\varepsilon = \beta\chi$, where β is the amplitude of the pump field and χ is proportional to the nonlinear susceptibility of the medium.

Since in degenerate parametric down-conversion the frequency of the pump field is twice the frequency of the signal field ($\omega_p = 2\omega$), the Hamiltonian can be simplified to

$$\hat{H} = i\hbar\chi^{(2)}(\beta^*\hat{a}\hat{a} - \beta\hat{a}^\dagger\hat{a}^\dagger). \quad (3.9)$$

The evolution operator associated with this Hamiltonian is given by

$$\hat{U} = \exp\left(-\frac{i}{\hbar}\hat{H}t\right) = \exp(\eta^*t\hat{a}\hat{a} - \eta t\hat{a}^\dagger\hat{a}^\dagger),$$

where $\eta = \beta\chi^{(2)}$. This result has the form of the squeezing operator as introduced in Equation 2.65. It thus becomes evident that the process of degenerate parametric down-conversion can produce squeezing.

The above considerations correspond to a single-pass of the pump field through the medium. To increase the interaction between the two participating light fields, the nonlinear crystal is usually placed inside an optical cavity. Typically, the cavity is designed such that only the signal field is resonantly enhanced. Once more, let us suppose the depletion of the pump to be negligible. The pump mode can hence be treated classically. The resulting Hamiltonian is [3.8]

$$\hat{H} = \hbar\omega\hat{a}^\dagger\hat{a} + \frac{i\hbar}{2}(\varepsilon\hat{a}^\dagger\hat{a}^\dagger - \varepsilon^*\hat{a}\hat{a}) + \hat{a}\hat{\Gamma}^\dagger + \hat{a}^\dagger\hat{\Gamma}, \quad (3.10)$$

where $\varepsilon = \beta\chi$, with β being the amplitude of the pump, and χ being proportional to the nonlinear susceptibility of the medium. The losses due to the cavity are represented by the reservoir operator $\hat{\Gamma}$. Let us assume a single ended cavity, as illustrated in Fig. (3.1), with a single *loss rate* γ_1 . The loss rate is sometimes also referred to

as *decay rate* or *coupling rate*. It is defined by $\gamma_1 = T/2\tau$, where T is the power transmissivity of the coupling mirror and τ is the cavity round-trip time. The round-trip time is given by $\tau = L/c$, with L being the optical round-trip length of the cavity and c is the vacuum speed of light. In such a model, a corresponding loss rate is ascribed to each loss mechanism. Such additional loss mechanisms include, for example, intra-cavity loss (e.g. due to absorption and scattering) and loss at the cavity end mirror. The total loss rate of the cavity is then given by the sum of the individual loss rates. Here it was assumed that no other loss mechanisms, except for loss due to the transmission of the coupling mirror, exist. Therefore, γ_1 corresponds to the total decay rate of the cavity. Note that different definitions for the decay rate exist [3.3]. The one given here is a good estimate for relatively high reflectivities, and in that case is also equal to the cavity *half-linewidth*, that is the half width at half maximum (HWHM). For the case that the input at the signal field frequency is just the vacuum field (with a variance of the fluctuations equal to 1), the spectra of the output noise variances can be calculated to be [3.8]

$$V_1^{\text{out}}(\omega) = 1 + \frac{4\gamma_1|\varepsilon|}{(\gamma_1 - |\varepsilon|)^2 + \omega^2}, \quad (3.11)$$

$$V_2^{\text{out}}(\omega) = 1 - \frac{4\gamma_1|\varepsilon|}{(\gamma_1 + |\varepsilon|)^2 + \omega^2}, \quad (3.12)$$

where $\omega = 0$ means that the cavity is on resonance. Introducing the pump parameter $\xi = \varepsilon/\gamma_1$ yields

$$V_1^{\text{out}}(\omega) = 1 + \frac{4\xi}{(1 - \xi)^2 + \left(\frac{\omega}{\gamma_1}\right)^2}, \quad (3.13)$$

$$V_2^{\text{out}}(\omega) = 1 - \frac{4\xi}{(1 + \xi)^2 + \left(\frac{\omega}{\gamma_1}\right)^2}. \quad (3.14)$$

From the linear variances V , the strength of squeezing and anti-squeezing on a logarithmic scale V_{dB} can be calculated via the relation

$$V_{\text{dB}} = 10 \log_{10}(V). \quad (3.15)$$

To obtain the squeezing and anti-squeezing when measuring exactly on the OPA resonance frequency, we set $\omega = 0$ and find the output variance of the signal field in dependence of the pump parameter ξ as plotted in Fig. 3.2. It can be seen that for ξ approaching unity, the fluctuations in the X_2 quadrature tend to zero and the

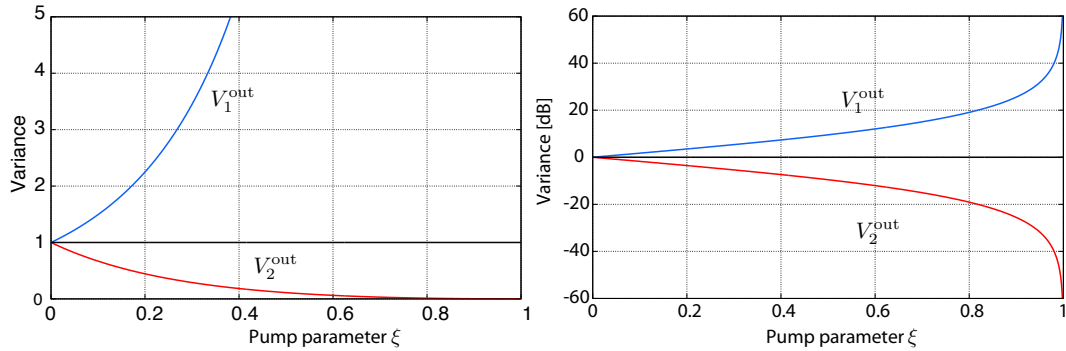


Figure 3.2 — Pump parameter dependent output of an optical parametric amplifier. The squeezing occurs in the phase quadrature. The amplitude quadrature is anti-squeezed. In principle, the squeezing/anti-squeezing is infinitely strong when the OPO threshold is reached at $\xi = 1$. Left: linear scale with the variance of the vacuum fluctuations equal to one. Right: logarithmic scale. The limited amount of squeezing and anti-squeezing results from the limited resolution of the x -axis. The detection frequency was chosen to be equal to the resonance frequency of the cavity ($\omega = 0$).

fluctuations in the X_1 quadrature diverge. The point of maximum squeezing/anti-squeezing is at $\xi = 1$. This is the so-called *threshold* to optical parametric oscillation (OPO). Above threshold a coherent field at the signal frequency would be produced and the pump would be significantly depleted. In that case, the assumptions made within the simple model described here are no longer valid.

For a description of the optical parametric amplification above threshold, see for example [3.2, 3.8]. When the squeezed-light source is operated below threshold, the predicted squeezing value approaches infinity when approaching threshold. Note that the process of optical parametric amplification itself and the actual device [for example the squeezed-light source depicted in Fig. (3.1)] which is said to be an optical parametric amplifier are both abbreviated as OPA throughout this thesis.

3.2 Detection of quantum noise

In this section, the basic principles of the detection of light are reviewed. First, the concept of *linearization of operators* is introduced, a technique that is often used to simplify quantum optical computations. Subsequently, the *direct homodyne detection* of light, that is the use of a single photo-sensitive device to detect the light from a single laser beam, is outlined. Subsequently, the considerations are extended to

introduce the *balanced homodyne detection* which is the most important detection scheme in continuous-wave quantum optics. Finally, the very central issue of optical loss, which is crucial in experiments that aim at the detection of strong squeezing, will be addressed.

3.2.1 Linearization of operators

The linearization of operators was applied for the first time within the field of quantum optics to model squeezing in a cavity [3.1]. The basic idea is to assume that the steady state amplitude of the electromagnetic field is much larger than the fluctuations. In this case, the operator can be expanded about the steady state value and the calculations can be simplified by linearizing the resulting expression to first order in the fluctuation terms. For example, applying the linearization to the annihilation and creation operators yields

$$\hat{a} = \alpha + \delta\hat{a} \quad \text{and} \quad (3.16)$$

$$\hat{a}^\dagger = \alpha^* + \delta\hat{a}^\dagger, \quad (3.17)$$

where α and α^* are the complex-numbered steady state expectation values of the operators \hat{a} and \hat{a}^\dagger corresponding to the classical amplitudes of the electromagnetic field. As a consequence of the linearization, all fluctuations are attributed to the operators $\delta\hat{a}$ and $\delta\hat{a}^\dagger$ and hence

$$\langle \delta\hat{a} \rangle = \langle \delta\hat{a}^\dagger \rangle = 0. \quad (3.18)$$

With the linearized expressions from Eq. (3.16) and Eq. (3.17), the variances of the quadrature operators can be expressed as

$$\Delta^2 X_1 = \langle (\delta\hat{a} + \delta\hat{a}^\dagger)^2 \rangle = \langle (\delta\hat{X}_1)^2 \rangle, \quad (3.19)$$

$$\Delta^2 X_2 = \langle (-i(\delta\hat{a} - \delta\hat{a}^\dagger))^2 \rangle = \langle (\delta\hat{X}_2)^2 \rangle. \quad (3.20)$$

Note that for the sake of simplicity the vacuum level was chosen to be equal to unity. The linearization can be regarded as the mathematical description of the ‘quantum phasor’ or ‘ball-on-stick’ picture as introduced in Sec. 2.3. The coherent amplitude α represents the phasor while the fluctuating term describes the uncertainty circle.

As an example, let us now consider the linearization of the number operator $\hat{n} = \hat{a}^\dagger \hat{a}$. Assuming α to be real-valued and using the linearized operators as given by Eqs. (3.16)

and (3.17) yields

$$\begin{aligned}
\hat{n} &= (\alpha^* + \delta\hat{a}^\dagger)(\alpha + \delta\hat{a}) \\
&= \alpha^2 + \alpha \left[\delta\hat{a}^\dagger + \delta\hat{a} \right] + \delta\hat{a}^\dagger \delta\hat{a} \\
&\approx \alpha^2 + \alpha\delta\hat{X}_1 .
\end{aligned} \tag{3.21}$$

For the last step, the assumption was made that second- and higher-order fluctuation terms are negligibly small compared to the coherent amplitude. Note that this is the assumption that justified the linearization in the first place.

The linearized version of the number operator can now be used to calculate its variance for which we obtain

$$\begin{aligned}
\Delta^2\hat{n} &= \langle \hat{n}^2 \rangle - \langle \hat{n} \rangle^2 \\
&= \langle (\alpha^2 + \alpha\delta\hat{X}^+)^2 \rangle - \langle \alpha^2 + \alpha\delta\hat{X}^+ \rangle^2 \\
&= \alpha^2 \langle (\delta\hat{X}^+)^2 \rangle \\
&= \alpha^2 \Delta^2\hat{X}_1 .
\end{aligned} \tag{3.22}$$

For a coherent state ($\Delta^2\hat{X}_1 = 1$) this yields $\Delta^2\hat{n} = \alpha^2$ which is in agreement with the variance of a random variable with poissonian distribution.

3.2.2 Direct homodyne detection

In experiments, light is usually detected with photo diodes. These are semi-conductor diodes in which the photoelectric effect converts incident photons into electrons. When directly detecting a laser beam with a single photo diode, the resulting photocurrent I is therefore proportional to the number of photons in the optical field

$$i(t) \propto \hat{a}^\dagger(t)\hat{a}(t) . \tag{3.23}$$

Making use of the linearization of operators once more and again assuming α to be real, the photocurrent is can be described by

$$i(t) \propto \alpha^2 + \alpha\delta\hat{X}_1(t) . \tag{3.24}$$

The resulting photocurrent is the sum of a large direct current (DC) term (that is proportional to the intensity) and an alternating current (AC) term given by the fluctuations of the amplitude quadrature scaled by the mean field amplitude. Hence, in order to gain information about the quantum noise, the fluctuations of the light field are of interest and have to be measured. To measure the fluctuations $\delta\hat{X}_1(\omega)$,

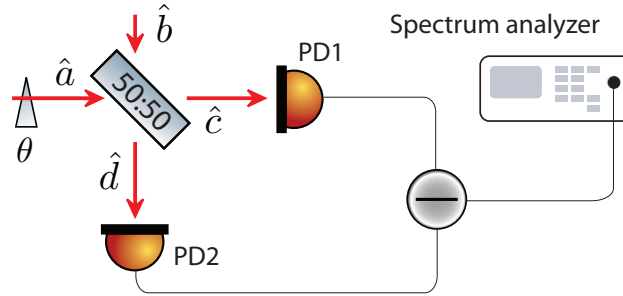


Figure 3.3 — Schematic diagram of a balanced homodyne detection. The two outputs of the beamsplitter are detected with photo diodes PD1 and PD2. The differential phase $e^{i\theta}$ between the inputs can be varied with a phase shifter, typically a piezo-actuated mirror in the beam path. The difference signal is recorded with a spectrum analyzer.

the resulting photocurrent is typically transformed into a voltage that can be fed into a spectrum analyzer to obtain a power spectrum. The power spectrum is the frequency-space equivalent to the variance Δ^2 in the time domain. Taking the Fourier transform of Eq. (3.24) gives

$$i(\omega) \propto \alpha^2 + \alpha \delta \hat{X}_1(\omega), \quad (3.25)$$

and analogous to Eq. (3.22) the variance of the photocurrent as measured by a spectrum analyzer is

$$V(\omega) \propto \alpha^2 \langle (\delta \hat{X}_1)^2 \rangle = \alpha^2 V_1(\omega). \quad (3.26)$$

The result of a direct detection is the variance of the amplitude quadrature multiplied by the optical DC power of the light field. Therefore, no information about any other quadrature can be obtained from a direct detection.

3.2.3 Balanced homodyne detection

One method to conduct a phase-sensitive measurement is the so-called *balanced homodyne detection*. The signal field is brought to interfere on a symmetric beamsplitter with a reference field, also referred to as the *local oscillator* (LO), that originates from the same laser source. As schematically depicted in Fig. 3.3, two input fields \hat{a} (the LO) and \hat{b} (the signal) are overlapped on a beamsplitter. The beamsplitter ratio is 1/2, that is the transmissivity and reflectivity are both 50% (in power). Each of the two outputs is detected with a photo diode (PD) and the differential signal is fed into a spectrum analyzer. For a generic beamsplitter, the output fields are connected to the

input fields via

$$\begin{pmatrix} \hat{c} \\ \hat{d} \end{pmatrix} = \begin{pmatrix} t & r \\ -r & t \end{pmatrix} \begin{pmatrix} \hat{a} \\ \hat{b} \end{pmatrix}, \quad (3.27)$$

where lower case r and t are the reflectivity and transmissivity in terms of field amplitudes. These are connected to the power reflectivity R and transmissivity T by $r = \sqrt{R}$ and $t = \sqrt{T}$. Assuming a loss-free beamsplitter with $R = T = 0.5$, the output fields \hat{c} and \hat{d} are given by

$$\begin{pmatrix} \hat{c} \\ \hat{d} \end{pmatrix} = \frac{1}{\sqrt{2}} \begin{pmatrix} 1 & 1 \\ -1 & 1 \end{pmatrix} \begin{pmatrix} \hat{a} \\ \hat{b} \end{pmatrix}. \quad (3.28)$$

For the annihilation and creation operator of the two output fields it follows

$$\hat{c} = \frac{1}{\sqrt{2}}(\hat{a} + \hat{b}), \quad \hat{c}^\dagger = \frac{1}{\sqrt{2}}(\hat{a}^\dagger + \hat{b}^\dagger), \quad (3.29)$$

$$\hat{d} = \frac{1}{\sqrt{2}}(-\hat{a} + \hat{b}), \quad \hat{d}^\dagger = \frac{1}{\sqrt{2}}(-\hat{a}^\dagger + \hat{b}^\dagger). \quad (3.30)$$

The photocurrents i_1 and i_2 that are generated in the two detectors are proportional to the light intensities and hence to the number of incident photons:

$$i_1 \propto \hat{c}^\dagger \hat{c} = \frac{1}{2}(\hat{a}^\dagger + \hat{b}^\dagger)(\hat{a} + \hat{b}), \quad (3.31)$$

$$i_2 \propto \hat{d}^\dagger \hat{d} = \frac{1}{2}(-\hat{a}^\dagger + \hat{b}^\dagger)(-\hat{a} + \hat{b}). \quad (3.32)$$

Once again we use the linearization procedure to decompose the operators \hat{a} and \hat{b} into their steady-state values and their fluctuations. We write $\hat{a} = \alpha + \delta\hat{a}$ and $\hat{b} = \beta + \delta\hat{b}$ and in the following neglect terms like $\delta\hat{a}\delta\hat{b}$ in the calculations. Setting the phase of \hat{b} as the reference phase, we can choose β to be real and extract the differential phase $e^{i\theta}$ from \hat{a} , such that \hat{a} is replaced by

$$\hat{a} = \hat{a}_0 e^{i\theta} = \alpha_0 e^{i\theta} + \delta\hat{a} e^{i\theta}. \quad (3.33)$$

We can now write the photocurrents from Eqs. (3.31) and (3.32) as

$$i_1 \propto \frac{1}{2}(\alpha_0 e^{-i\theta} + \delta\hat{a}^\dagger e^{-i\theta} + \beta + \delta\hat{b}^\dagger)(\alpha_0 e^{i\theta} + \delta\hat{a} e^{i\theta} + \beta + \delta\hat{b}) \quad (3.34)$$

$$= \frac{1}{2} \left[\alpha_0^2 + \beta^2 + 2\alpha_0\beta \cos\theta + \alpha_0(\delta\hat{X}_a^+ + \delta\hat{X}_b^\theta) + \beta(\delta\hat{X}_b^+ + \delta\hat{X}_a^{-\theta}) \right], \quad (3.35)$$

and

$$i_2 \propto \frac{1}{2} (-\alpha_0 e^{-i\theta} - \delta \hat{a}^\dagger e^{-i\theta} + \beta + \delta \hat{b}^\dagger) (-\alpha_0 e^{i\theta} - \delta \hat{a} e^{i\theta} + \beta + \delta \hat{b}) \quad (3.36)$$

$$= \frac{1}{2} \left[\alpha_0^2 + \beta^2 - 2\alpha_0\beta \cos \theta + \alpha_0 (\delta \hat{X}_a^+ - \delta \hat{X}_b^\theta) + \beta (\delta \hat{X}_b^+ - \delta \hat{X}_a^{-\theta}) \right], \quad (3.37)$$

where $\delta \hat{X}_a^+ = \delta \hat{a} + \delta \hat{a}^\dagger$ and $\delta \hat{X}_b^+ = \delta \hat{b} + \delta \hat{b}^\dagger$ are the fluctuations of the amplitude quadrature of the two input fields, and $\delta \hat{X}_a^\theta = \delta \hat{a} e^{-i\theta} + \delta \hat{a}^\dagger e^{i\theta}$ and $\delta \hat{X}_b^\theta = \delta \hat{b} e^{-i\theta} + \delta \hat{b}^\dagger e^{i\theta}$ are the respective generic quadrature operators.

The difference of the two photocurrents is given by

$$i_- \propto \hat{c} \hat{c}^\dagger - \hat{d} \hat{d}^\dagger \quad (3.38)$$

$$= 2\alpha_0\beta \cos \theta + \alpha_0 \delta \hat{X}_b^\theta + \beta \delta \hat{X}_a^{-\theta}. \quad (3.39)$$

Finally, we obtain the variance of the differential current as measured by the spectrum analyzer:

$$V_{i_-} = \alpha_0^2 V(\delta \hat{X}_b^\theta) + \beta^2 V(\delta \hat{X}_a^{-\theta}). \quad (3.40)$$

The necessary condition for this detection scheme is a LO power much higher than the signal power ($\alpha_0^2 \gg \beta^2$). In this case the term containing β^2 can be neglected. In the limit of a strong local oscillator, the detected variance thus reduces to

$$V_{i_-} = \alpha_0^2 V(\delta \hat{X}_b^\theta). \quad (3.41)$$

This indeed is a remarkable result since this variance only contains fluctuations of the field entering through the signal port scaled by the DC power of the LO. It *does not* contain any noise from the LO field. By changing the phase between the LO and the signal field, any arbitrary quadrature of \hat{b} can be investigated. By blocking the signal port – and thus setting the input to be the vacuum state for which $V(\delta \hat{X}_b^\theta) = 1$ for all θ – one obtains the shot-noise reference against which the possible squeezing is measured. This means that whenever we measure a quadrature variance $V_{i_-} < \alpha_0^2$, we have observed a squeezed state.

Apparently, the shot noise level depends on the power used for the LO. It is crucial to keep the shot noise level constant throughout data taking in order to avoid misleading squeezing values.

3.3 Limits to the measurable level of squeezing

So far, only the model of an ideal (lossless) OPA with the output detected exactly at zero frequency offset with a perfect detection efficiency was considered. In the

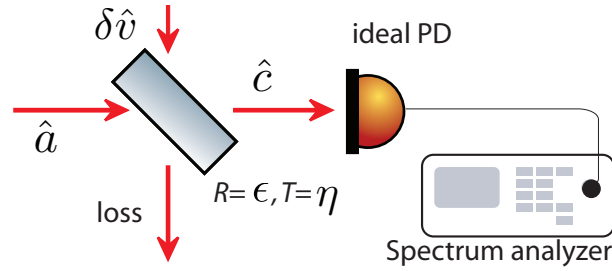


Figure 3.4 — Optical loss modeled by an ideal detector and a beamsplitter with power transmission η , being equal to the total detection efficiency of the measurement process.

following, a more physical model that is able to predict the outcome of an experiment is derived. To this end, first the general procedure to model the effect of optical loss is introduced. We will see that optical loss will severely degrade the squeezing level. Second, the total detection efficiency that takes into account possible loss channels of a squeezing setup is detailed. Third, the squeezing bandwidth is examined. Due to the transfer function, additional constraints are imposed on the output variance if the squeezed-light source is realized as a cavity. Subsequently, the issue of electronic dark noise is addressed. Finally, the model for a realistic squeezed-light source is presented.

3.3.1 Modeling optical loss

The photocurrent and hence the detected spectrum only is an exact electronic reproduction of the photon noise if the measurement is conducted with an ideal detector. The ideal detector creates an electron from each incident photon, that is its quantum efficiency, which is the ratio of generated electrons to the number of incident photons, is equal to one. However, in practice the quantum efficiency of available photo diodes usually is smaller than one. Additionally, effects such as absorption and scattering can prevent the photon from reaching the detector. All effects can be combined to yield a total detection efficiency η . The *optical loss* can be modeled by a beamsplitter with power reflectivity $\epsilon = 1 - \eta$, as schematically shown in Fig. (3.4). The detector is ideal, but the beamsplitter has a transmission equal to the total detection efficiency η . The field incident on the detector is given by

$$\hat{c} = \sqrt{\eta}\hat{a} + \sqrt{1-\eta}\delta\hat{v}, \quad (3.42)$$

where $\delta\hat{v}$ are the vacuum fluctuations coupling into the measurement process. With the linearization $\hat{a} = \alpha + \delta\hat{a}$, the photocurrent is

$$i \propto \hat{c}^\dagger \hat{c} = \eta\alpha^2 + \sqrt{\eta}\alpha \left(\sqrt{\eta}\delta\hat{X}_a^+ + \sqrt{1-\eta}\delta\hat{X}_v^+ \right), \quad (3.43)$$

with the first term corresponding to the DC-part of the current scaled by the detection efficiency. The second term contains the fluctuations. Calculating the variance as measured by the spectrum analyzer gives

$$V_i = \eta\alpha^2 [\eta V_a^+ + (1-\eta)]. \quad (3.44)$$

The same kind of loss model can be applied to the balanced homodyne detector. Let the variance for the loss-free homodyne detection relative to the shot-noise reference level be V_0 . Upon including loss in the analysis, the variance becomes

$$V_\eta = \eta V_0 + (1-\eta). \quad (3.45)$$

Let us assume that the signal input to a homodyne detector has the variance V_{dB} measured in dB, that is, the linear variance $V_{\text{lin}} = 10^{(V_{\text{dB}}/10)}$. Thus, the resulting variance after experiencing the optical loss is

$$V_{\eta,\text{dB}} = 10 \log 10 \left[\eta 10^{\frac{V_{\text{dB}}}{10}} + (1-\eta) \right]. \quad (3.46)$$

The dependence of the measured variance on the detection efficiency is plotted in Fig. (3.5) for four different pairs of squeezing and anti-squeezing values. It is evident that the effect is stronger for the squeezed variance and that especially strong squeezing levels are degraded rapidly by optical loss. Furthermore, it can be seen that the purity, which is proportional to the product of the variances of amplitude and phase quadrature, changes. To infer the purity one has to use the lossy variances together with Eq. (2.110). With the vacuum reference set to 1, this yields for the purity

$$\mu = \frac{1}{\sqrt{V_{1,\eta} V_{2,\eta}}} = \frac{1}{\sqrt{1 + (\eta - \eta^2)(V_{0,1} + V_{0,2} - 2)}}, \quad (3.47)$$

where Eq. (3.45) for the lossy variances was used and $V_{0,1}$ and $V_{0,2}$ are the initial variances of the loss-free state and η is the detection efficiency. Equation (3.47) reveals that the impact of optical loss on the purity of the state depends on the degree of initial squeezing.

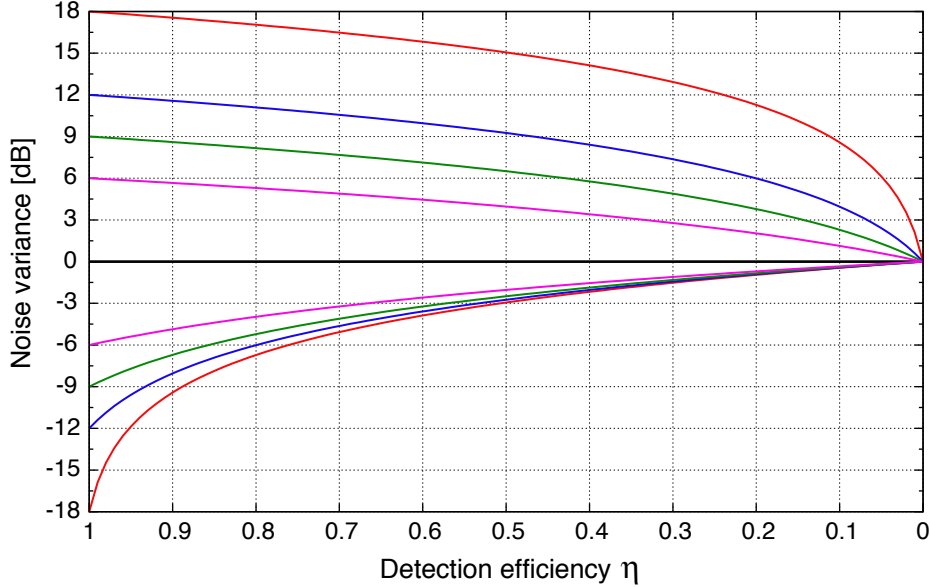


Figure 3.5 — Dependence of the measured noise variance on the total detection efficiency η . Four pairs of states with initial squeezing and anti-squeezing of ± 18 dB, ± 12 dB, ± 9 dB, and ± 6 dB are shown. The effect is stronger for the squeezed variance, especially when strong squeezing levels are assumed.

3.3.2 Total detection efficiency

Let us assume a homodyne detection scheme with a total detection efficiency η . The total detection efficiency is the product of possible inefficiencies in the OPA system. These are the escape, propagation, homodyne, and quantum efficiency, such that $\eta = \eta_{\text{esc}}\eta_{\text{prop}}\eta_{\text{homo}}\eta_{\text{qe}}$. In the following, each limiting factor is examined in more detail.

3.3.2.1 Escape efficiency

The OPA's escape efficiency is the ratio of the output coupling decay rate to the total cavity decay rate. The former is related to the transmission T of the coupling mirror, while the latter is determined by all other intra-cavity losses.

$$\eta_{\text{esc}} = \frac{\gamma_T}{\gamma_T + \gamma_L} = \frac{T}{T + L}. \quad (3.48)$$

The round-trip loss L includes possible transmission through a non-perfect high-reflection coating of the second mirror, absorption inside the nonlinear medium and scattering from imperfect anti-reflection coatings. It is therefore crucial to use high quality material in order to minimize L . It is obvious that the escape efficiency increases with increasing transmission of the coupling mirror. However, one has to take into account that this will lead to a larger OPO threshold.

3.3.2.2 Propagation efficiency

The propagation efficiency includes the loss that the squeezing experiences due to scattering, residual reflection and absorption. Scattering can occur at imperfect surfaces of optics in the beam path. Residual reflection can be caused by imperfect anti-reflection coatings of lenses and beamsplitters. Absorption will be caused upon transmission through optical components such as lenses and beamsplitters.

3.3.2.3 Photo-electric quantum efficiency

The quantum efficiency of the photo diodes is given by the percentage of photons incident on the detector that generate an electron-hole pair in the semiconductor material. A similar measure is the spectral responsivity R_λ of the detector. The responsivity is usually given in amperes per watt, and thus describes the amount of electric power (photocurrent) that can be generated from the optical power of the incident light. The quantum efficiency and the responsivity R_λ [A/W] are related by

$$\eta_{\text{qe}} = \frac{R_\lambda h c}{\lambda e} \approx \frac{R_\lambda 1240}{\lambda} \frac{\text{W nm}}{\text{A}}, \quad (3.49)$$

where h is Planck's constant, c is the speed of light in free space, λ is the wavelength in nm, and e is the elementary charge. The quantum efficiency depends on the semiconductor material and on the wavelength. A typical material for the detection of laser light at 1064 nm and 1550 nm is indium gallium arsenide (InGaAs). The respective second-harmonic wavelengths of 532 nm and 775 nm are usually detected with photo diodes made of silicon.

As already described earlier, each optical loss process introduces more contributions from the vacuum fluctuations and degrades the squeezing. For that reason, custom-made photo diodes and super-polished optics with custom made coatings were used when setting up our squeezed-light sources.

3.3.2.4 Homodyne efficiency

The homodyne efficiency describes the spatial overlap between the signal and the local oscillator modes on the homodyne detector's 50/50 beamsplitter. A mismatch between the two modes leads to imperfect interference. The mismatch can be quantified by the so-called *fringe visibility*

$$\text{VIS} = \frac{I_{\max} - I_{\min}}{I_{\max} + I_{\min}}, \quad (3.50)$$

where the maximum and minimum intensities I_{\max} and I_{\min} are measured with a single detector in one of the output ports by sweeping the relative phase between the two input fields. Assuming equal powers in the two input ports of the detector, we visibility is $0 \leq \text{VIS} \leq 1$, where 1 means a perfect overlap and 0 no overlap at all. The mode-mismatch of the two fields translates quadratically into the loss of optical power, such that the homodyne efficiency is

$$\eta_{\text{homo}} = \text{VIS}^2. \quad (3.51)$$

As an example, let us suppose the homodyne visibility is 99%. The corresponding efficiency $\eta_{\text{homo}} = 0.99^2 \approx 0.98$, so that 1% mode-mismatch equals a loss of 2% in optical power.

3.3.3 Squeezing bandwidth

The bandwidth over which squeezing can be generated is limited by the linewidth of the squeezed-light source for the fundamental field, that is the field to be squeezed. Figure 3.6 shows the squeezing and anti-squeezing as a function of the measurement frequency normalized to the cavity bandwidth. In order to plot Fig. 3.6, the squeezing spectrum as given by Eqs. (3.13) and (3.14) was plotted as a function of the sideband frequency which ranges up to ten times the cavity half-linewidth. The pump parameter was set to $\zeta = 0.5$. It becomes evident that the maximum level of noise suppression can only be obtained well within the linewidth of the cavity. The cavity's full width at half maximum (FWHM) linewidth ν can be determined by the ratio of the cavity's free spectral range (FSR) and the cavity finesse \mathcal{F}

$$\nu = \frac{\text{FSR}}{\mathcal{F}}. \quad (3.52)$$

The free spectral range can be obtained from the cavity's optical roundtrip-length l and the vacuum speed of light c :

$$\text{FSR} = \frac{c}{l}. \quad (3.53)$$

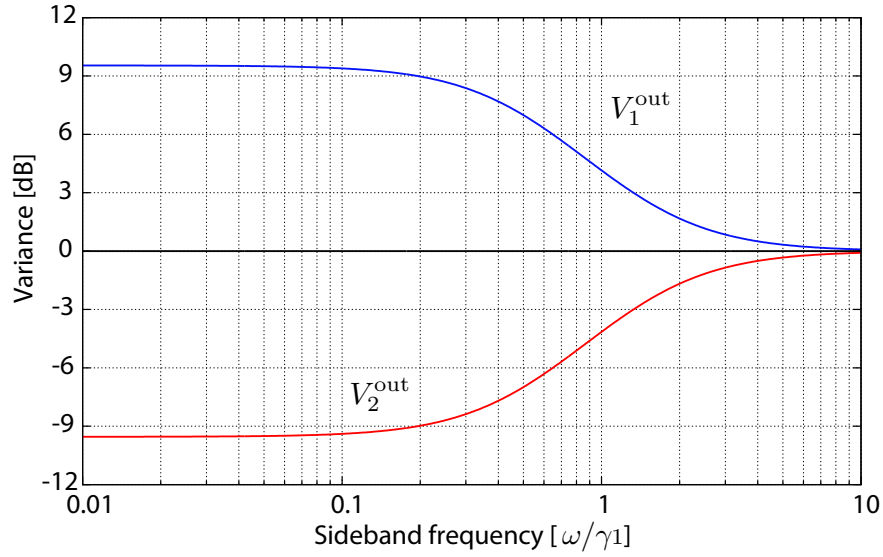


Figure 3.6 — Squeezing and anti-squeezing from an ideal OPA as a function of the sideband frequency. The quadrature variances are plotted depending on the measurement frequency ω normalized to the cavity bandwidth γ_1 . The pump parameter was set to $\zeta = 0.5$.

The finesse of the cavity is determined by the mirror reflectivities and possible intra-cavity loss, such as absorption loss and loss due to scattering. When we denote $\varrho = \sqrt{R_1 R_2}$, where R_1 is the power reflectivity of the coupling mirror and R_2 is the combination of the power reflectivity of the end mirror and of all intra-cavity losses, the finesse is given by [3.6]

$$\mathcal{F} = \frac{\pi}{2 \arcsin\left(\frac{1-\varrho}{2\sqrt{\varrho}}\right)}. \quad (3.54)$$

For the case of $\varrho \approx 1$, two common approximations to the exact equation exist

$$\mathcal{F} \approx \frac{\pi\sqrt{\varrho}}{1-\varrho} \approx \frac{\pi}{1-\rho}. \quad (3.55)$$

In the first approximation, the error in \mathcal{F} is smaller than 1% for $\mathcal{F} > 6.4$ and smaller than 0.1% for $\mathcal{F} > 20$. For the second approximation, the error is smaller than 1% for $\mathcal{F} > 160$ and smaller than 0.1% for $\mathcal{F} > 1570$.

3.3.4 Phase noise

The strength of the detectable squeezing is not only limited by optical loss. With increasing squeezing strength, the stability of the relative phase of the local oscillator and of the squeezed beam becomes more and more important. A jitter in the relative phase can have numerous origins, for example unstable locking loops, residual phase modulations or acoustically induced mirror motion. If this phase noise is faster than the time required for the spectrum analyzer to record a single data point, this point will not be a pure measurement of the variance at the angle θ . Instead, the result will be an integration over a range of angles $\theta \pm \Delta\theta$. In that case, a part of the anti-squeezed quadrature will couple into the measurement and the squeezing will no longer be maximal. Under the influence of the random phase fluctuations, the state that is described by the Wigner function from Eq. (2.97) will evolve into a mixed state. The Wigner function of a phase-diffused squeezed vacuum state is given by [3.5]

$$W(X_1, X_2) = \frac{1}{2\pi\sqrt{V_1V_2}} \int \exp \left[-\frac{1}{2} \left(\frac{(X_1^\phi)^2}{V_1} + \frac{(X_2^\phi)^2}{V_2} \right) \right] \Phi(\phi) d\phi, \quad (3.56)$$

where

$$X_1^\phi = X_1 \cos \phi + X_2 \sin \phi \quad \text{and} \quad (3.57)$$

$$X_2^\phi = X_2 \cos \phi - X_1 \sin \phi. \quad (3.58)$$

If one assumes the phase noise to be gaussian, the distribution function $\Phi(\phi)$ is completely described by the standard deviation σ and can be written as

$$\Phi(\phi) = \frac{1}{\sqrt{2\pi\sigma^2}} \exp \left(-\frac{\phi^2}{2\sigma^2} \right). \quad (3.59)$$

The effect that phase fluctuations have on a squeezed state is illustrated in Fig. 3.7. The plots show the Wigner function of a vacuum state that is squeezed by -10 dB in the phase quadrature and is anti-squeezed by $+10$ dB in the amplitude quadrature. Perfect phase stability was assumed for the left plot, enabling a pure state with maximum noise suppression. With increasing phase noise, the state is more and more transformed into a mixed state with a reduced degree of squeezing.

When assuming the standard deviation of the normally distributed phase fluctuations to be small, phase jitter with an rms of θ_{fluc} is equal to the homodyne detector measuring at a phase offset θ_{fluc} . The resulting variances can then be written as [3.7]

$$V'_{1,2} = V_{1,2} \cos^2 \theta_{\text{fluc}} + V_{2,1} \sin^2 \theta_{\text{fluc}}, \quad (3.60)$$

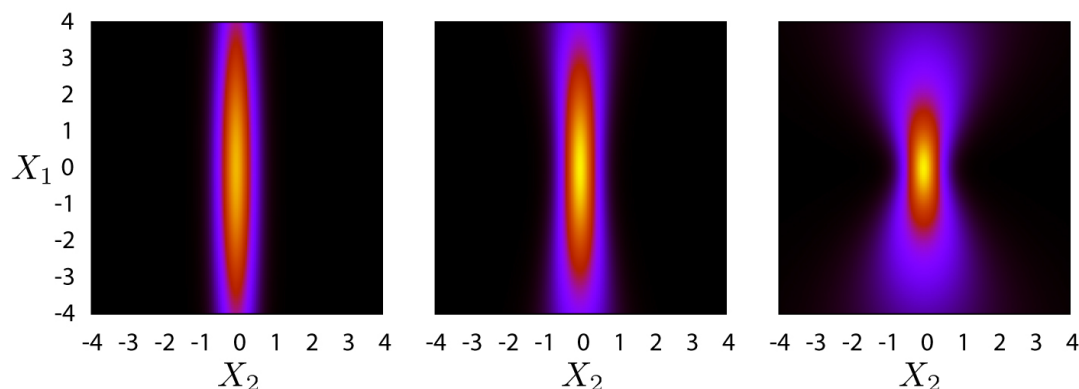


Figure 3.7 — Wigner function of a squeezed vacuum state with -10 dB of squeezing in the phase quadrature X_2 and 10 dB of anti-squeezing in the amplitude quadrature X_1 . Left: no phase noise was assumed, so that $\sigma = 0$. Middle: phase fluctuations with $\sigma = 0.1$ ($\approx 6^\circ$). Right: phase fluctuations with $\sigma = 0.3$ ($\approx 17^\circ$). It can be seen that with the increase in phase noise the state is more and more transformed into a mixed state with a reduced degree of squeezing.

where $V_{1,2}$ are the variances as given by Eqs. (3.13) and (3.14) such that

$$V_{1,2} = 1 \pm \frac{4\zeta}{(1 \mp \zeta)^2 + \left(\frac{\omega}{\gamma_1}\right)^2}. \quad (3.61)$$

The effect that phase noise has on the detected quadrature variances is plotted in Fig. 3.8. Once more, a pure vacuum state with 10 dB of squeezing was assumed. The phase fluctuations were set to $\theta_{\text{fluc}} = 6^\circ$, such that the state equals the phase-diffused squeezed vacuum state corresponding to the Wigner function depicted in Fig. 3.7 (middle). The dashed lines represent the reference variances without the influence of phase fluctuations. The solid lines correspond to the variances under the influence of phase noise. While the anti-squeezing stays unchanged, the squeezing is degraded from -10 dB to -6.8 dB. The frequency dependence of the effect is due to the decrease of the nonlinear gain. The reason is that at high frequencies the upper and lower sidebands acquire a large phase shift for each round trip, which essentially limits the nonlinear interaction.

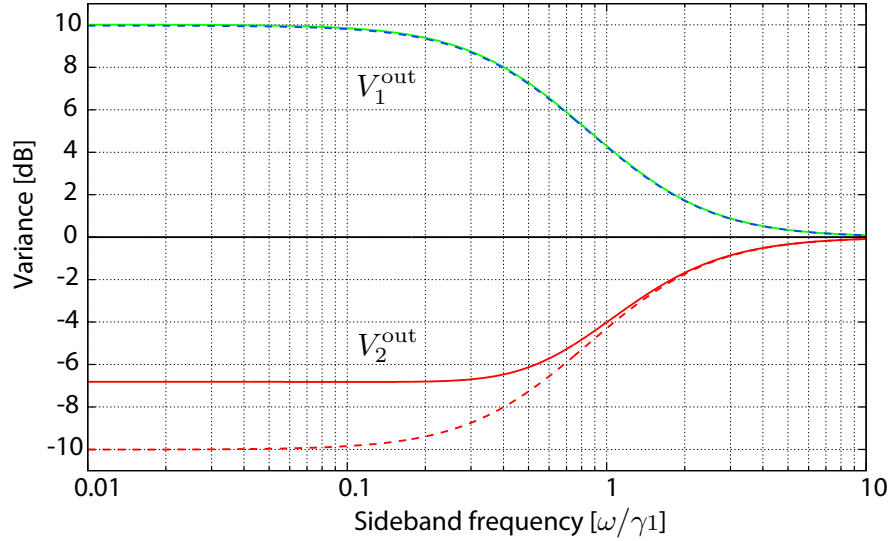


Figure 3.8 — Squeezing and anti-squeezing as a function of sideband frequency including phase fluctuations. The dashed lines correspond to the quadrature variances without phase noise. The solid lines illustrate the effect of a phase jitter with $\theta = 6^\circ$. The quadrature variances are plotted as a function of sideband frequency ω normalized to the cavity bandwidth γ_1 . The pump parameter was set to $\zeta = 0.52$.

3.3.5 Electronic dark noise

Every (homodyne) detector has a certain electronic dark noise. This is the noise measured by the spectrum analyzer when all input ports are blocked, that is when no light is incident on the detector. When conducting a balanced homodyne measurement, the clearance of the shot-noise reference level from the detector dark noise is crucial. If the clearance is not large enough, it will significantly contribute to the measured noise level. Consequently the measurable squeezing will be reduced. This makes the signal to dark noise ratio an important figure in an experiment that aims for the detection of strong squeezing. Ideally, the electronic dark noise is the uncorrelated sum of the electronic noise produced by the components that are used for the homodyne detector circuitry. Low-noise components should therefore be considered when designing the detector. Additionally, the spectrum analyzer's dark noise has to be taken into account. Likewise, stray fields from electronic oscillators and possible noise from the power supply will contribute to the final dark noise level. For the homodyne detectors that were used in the experiments presented in this thesis, a 'self-subtraction' scheme was applied in order to directly cancel the DC part of the photocurrent. Details on the

design can be found in [3.9]. The subtraction of the photocurrents was realized prior to the first electronic amplification stage, such that only the photocurrent fluctuations were converted into a voltage. On the one hand, this allows for high electronic gains within the circuit. On the other hand, this permits the use of a strong local oscillator. By those means, dark noise clearances of up to ~ 25 dB could be realized.

In earlier experiments it used to be customary to state an inferred squeezing value, which was obtained by subtraction of the dark-noise. Throughout this thesis, squeezing values were only corrected for electronic dark noise to compare them with the values predicted by theory. Whenever this was done, it is clearly stated. All other values represent direct observations.

3.4 Model of a realistic squeezed-light source

In the following the above considerations are combined to yield a model for a squeezed-light source that is suitable to be compared with experimentally obtained data. In order to get an expression that is more convenient from the experimentalist's point of view, we start by noting that the pump parameter $\xi = \varepsilon/\gamma_1$ can also be equated with the ratio of the pump field amplitude to the threshold pump field amplitude [3.4]. This can be expressed in terms of the pump power P and the threshold pump power, such that $\xi = \sqrt{P/P_{\text{th}}}$. We incorporate the total detection efficiency $\eta = \eta_{\text{esc}}\eta_{\text{prop}}\eta_{\text{homo}}\eta_{\text{det}}$ by using Eq. (3.46) to determine the effect of losses on the variances from Eq. (3.11) and (3.12). This yields

$$V_1(\Omega') = 1 + \eta_{\text{esc}}\eta_{\text{prop}}\eta_{\text{homo}}\eta_{\text{det}} \frac{4\sqrt{P/P_{\text{th}}}}{(1-\sqrt{P/P_{\text{th}}})^2 + (\Omega')^2}, \quad (3.62)$$

$$V_2(\Omega') = 1 - \eta_{\text{esc}}\eta_{\text{prop}}\eta_{\text{homo}}\eta_{\text{det}} \frac{4\sqrt{P/P_{\text{th}}}}{(1+\sqrt{P/P_{\text{th}}})^2 + (\Omega')^2}, \quad (3.63)$$

where we have introduced the normalized frequency $\Omega' = f/\frac{1}{2}\nu$, with the spectrum analyzer's measurement frequency f and the cavity (FWHM) linewidth ν . To include phase noise in the simulation we use Eq. (8.2) and obtain

$$V'_1(\Omega') = V_1(\Omega') \cos^2 \theta_{\text{fluc}} + V_2(\Omega') \sin^2 \theta_{\text{fluc}}, \quad (3.64)$$

$$V'_2(\Omega') = V_2(\Omega') \cos^2 \theta_{\text{fluc}} + V_1(\Omega') \sin^2 \theta_{\text{fluc}}. \quad (3.65)$$

We will see in the following chapters that this model indeed is able to give precise predictions of the experimental outcome.

References

- [3.1] B. Yurke, "Use of cavities in squeezed-state generation," *Phys. Rev. A* **29**, 408–410 (1984).
- [3.2] N. B. Grosse, *Harmonic entanglement and photon anti-bunching*, PhD thesis, The Australian National University, Canberra, Australia, 2009.
- [3.3] A. G. White, *Classical and quantum dynamics of optical frequency conversion*, PhD thesis, The Australian National University, Canberra, Australia, 1997.
- [3.4] B. C. Buchler, *Electro-optic Control of Quantum Measurements*, PhD thesis, The Australian National University, Canberra, Australia, 2001.
- [3.5] A. Franzen, B. Hage, J. DiGuglielmo, J. Fiurášek, and R. Schnabel, "Experimental Demonstration of Continuous Variable Purification of Squeezed States," *Phys. Rev. Lett.* **97**, 150505 (2006).
- [3.6] G. Heinzl, *Resonant Sideband Extraction—Neuartige Interferometrie für Gravitationswellendetektoren*, Master's thesis, MPI für Quantenoptik, Garching, 1995.
- [3.7] T. C. Zhang, K. W. Goh, C. W. Chou, P. Lodahl, and H. J. Kimble, "Quantum teleportation of light beams," *Phys. Rev. A* **67**, 033802 (2003).
- [3.8] K. McKenzie, *Squeezing in the Audio Gravitational Wave Detection Band*, PhD thesis, The Australian National University, Canberra, Australia, 2008.
- [3.9] H. Vahlbruch, *Squeezed Light for Gravitational Wave Astronomy*, PhD thesis, Leibniz Universität Hannover, 2008.

Strong squeezing at 1064 nm from a monolithic squeezed light resonator

Squeezed states of light constitute an important nonclassical resource in the field of high-precision measurements, for example, gravitational wave detection, as well as in the field of quantum information, for example, for teleportation, quantum cryptography, and distribution of entanglement in quantum computation networks. Strong squeezing in combination with high purity, high bandwidth, and high spatial mode quality is desirable in order to achieve significantly improved performances contrasting any classical protocols. Here we report on the observation of 11.5 dB of squeezing, together with relatively high state purity corresponding to a vacuum contribution of less than 5%, and a squeezing bandwidth of about 170 MHz. The analysis of our squeezed states reveals a significant production of higher-order pairs of quantum-correlated photons and the existence of strong photon-number oscillations.

Originally published as M. Mehmet et al. *Phys. Rev. A* **81**, 013814 (2010).

4.1 Introduction

Squeezed states as well as number states (Fock states) are so-called nonclassical states. They allow the measurement, the communication, and the processing of information in a way not possible with coherent states that are governed by vacuum

fluctuations. Squeezed states of light and correlated photon pairs have been used to realize interferometric measurements with sensitivities beyond the photon counting noise [4.1–4.6], to demonstrate the Einstein-Podolski-Rosen paradox [4.7–4.10], as a resource for quantum teleportation [4.11–4.13], and for the generation of Schrödinger cat states for quantum information networks [4.14, 4.15]. In view of applications in long-distance quantum communication, purification and distillation of entangled photon-number states and entangled two-mode squeezed states were experimentally demonstrated [4.16–4.18].

Fock states are characterized by photon counting detectors, whereas squeezed states are traditionally characterized in the phase space of position and momentum-like operators [4.19, 4.20]. Appropriate operators are the noncommuting amplitude and phase quadratures of the field, \hat{X}_1 and \hat{X}_2 , respectively. Their variances obey a Heisenberg uncertainty relation, $\Delta^2 \hat{X}_1 \cdot \Delta^2 \hat{X}_2 \geq 1/16$, with the vacuum noise variance normalized to $1/4$. A squeezed state is realized if the quantum noise of one quadrature is *squeezed* below the vacuum noise level, at the expense of increased noise of the other quadrature. For an overview we refer to Ref. [4.21]. The relation between the quadrature operators and the photon-number operator \hat{n} is revealed by the Hamilton operator of the quantized harmonic oscillator:

$$\hat{H} = \hbar\omega(\hat{n} + 1/2) = \hbar\omega(\hat{X}_1^2 + \hat{X}_2^2), \quad (4.1)$$

where \hbar is the reduced Planck constant and ω the light's angular frequency. One can think of the two expressions in equation (4.1) corresponding to the particle picture and the wave picture of quantum physics, respectively. These can be used to calculate the mean photon number of squeezed states. Note that this number is always greater than zero. Consider now a squeezed state without displacement in phase-space. Such a state is called a squeezed *vacuum* state, and one can write $\langle \hat{X}_i^2 \rangle = \Delta^2 \hat{X}_i$. If such a state is pure, that is, has minimum uncertainty, only *even* photon numbers can be observed [4.22, 4.23]. Furthermore, if the squeezing effect is strong a so-called odd-even *photon-number oscillation* is realized that includes not just the existence of photon pairs but also the existence of higher even numbers of quantum-correlated photons.

This article presents the generation and characterization of squeezed vacuum states with strong odd-even photon-number oscillations revealing a significant contribution of correlated photon numbers up to 10 and higher. This result is made possible because our squeezed vacuum states are strongly squeezed, are of high purity, and are in a well-defined spatial Gaussian fundamental mode. These properties are of great importance for applications in high-precision measurements as well as in quantum information. Our squeezed light source also exhibits a broad squeezing bandwidth and thus constitutes a bright source of quantum-correlated photons.

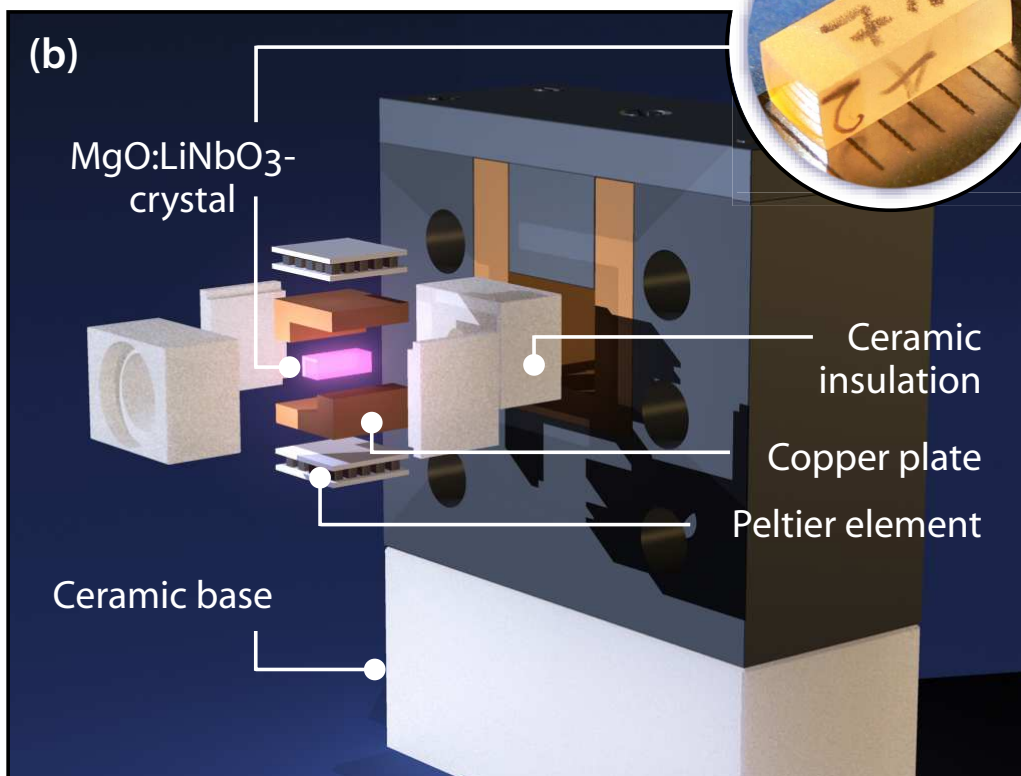
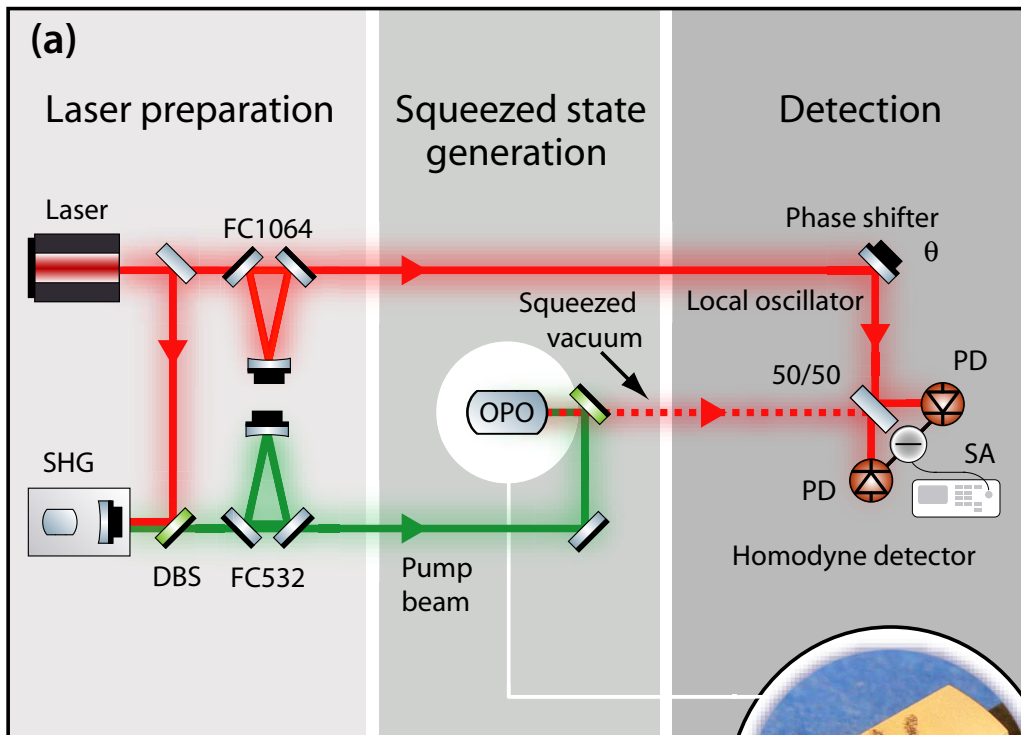
4.2 Experimental setup

At present the most successful squeezed light sources are based on parametric processes in nonlinear optical materials. In the regime of pulsed laser radiation the optical Kerr effect has recently enabled the observation of nearly 7 dB squeezing [4.24]. In the regime of continuous-wave laser radiation, squeezing of vacuum fluctuations by up to 10 dB was observed utilizing optical parametric oscillation (OPO) below threshold [4.25, 4.26].

The squeezed vacuum states investigated here were produced via type I OPO below threshold in a nonlinear standing wave cavity, similar to the experimental setup in [4.26]. In order to observe high levels of squeezing the entire experiment was optimized for low phase fluctuations and low optical loss. A schematic diagram of the experimental setup is shown in Fig. 4.1(a). The main light source was a 2-Watt continuous-wave laser at 1064 nm. It was used to generate a second-harmonic light field to pump the parametric squeezed light source and to provide the local oscillator (LO) beam for balanced homodyne detection. Both laser fields were sent through traveling wave filter cavities that were kept on resonance using Pound-Drever-Hall modulation-demodulation control schemes. The filter cavities therefore acted as optical low-pass filters that reduced potential phase noise and provided clean gaussian fundamental modes. The filtered second-harmonic pump beam had a power of up to 600 mW and was subsequently injected into the OPO cavity.

In order to minimize the internal optical loss of the squeezed light source we designed the OPO as a monolithic (bi-convex) cavity, similar to the resonator used in [4.27]. It was made from a 7% doped Mg:O LiNbO₃ crystal measuring $6.5 \times 2 \times 2.5$ mm³ with end faces of 8 mm radii of curvature (see inlay in Fig. 4.1). While the back of the crystal had a high reflection coating for both the wavelengths involved, we chose a rather low power reflectivity of 88% at 1064 nm (and < 1% at 532 nm) for the coupling front face in order to increase the ratio of out-coupling rate and cavity round-trip loss. The crystal was controlled to keep its phase-matching temperature close to 60°C using Peltier elements, and the main laser frequency was tuned to match the resonance condition of the OPO cavity. An assembly drawing of the crystal mounting is shown in Fig. 4.1(b).

No control fields at or near the fundamental wavelength of 1064 nm were injected into the squeezed light source during data taking. Thus all photons around 1064 nm leaving the OPO cavity originated from the parametric down-conversion process. The out-coupled squeezed states, that is, the photons at 1064 nm, were separated from the 532-nm pump upon reflection at a dichroic beam splitter (DBS) and subsequently analyzed by means of balanced homodyne detection. To this end the bright and



spatially filtered LO beam was precisely adjusted to the spatial mode of the squeezed beam. We achieved a fringe visibility of 99.8% at the homodyne detector's 50-50 beam splitter, which proves that the squeezed states were indeed in a well-defined Gaussian fundamental mode.

A homodyne detector is the only known means to observe and characterize strongly squeezed states. Today's single-photon detectors do not reach the same high quantum efficiencies and have an insufficient photon-number resolution. It has been shown that homodyne detection data of quantum states can indeed provide their *full* quantum information [4.28–4.30]. The phase angle θ between the local oscillator (LO) and the signal beam defines an arbitrary quadrature of the signal's quantum state $X(\theta) = \cos(\theta)X_1 + \sin(\theta)X_2$ [4.21]. In our experiment θ was controlled with a piezo actuated mirror in the LO path which allowed us to precisely set the phase angle. For example, to measure the squeezed quadrature $X(0) = X_1$ or the antisqueezed quadrature $X(\pi/2) = X_2$. The collected data was readily converted into variances by a spectrum analyzer that was also used to select a certain Fourier frequency f and resolution bandwidth Δf . The vacuum noise reference was measured with the same settings but with the squeezed field input blocked.

4.3 Observation of high-purity strongly squeezed states

The traces in Fig. 4.2(a)-4.2(c) represent three different squeezed vacuum states from our OPO source in terms of pairs of squeezed (bottom trace) and anti-squeezed

Figure 4.1 (preceding page) — Experimental apparatus. **(a)**, Schematic diagram of the experimental setup. A small part of the 1064-nm output of the 2-W laser system was used as local oscillator while the majority was sent to an external second-harmonic generation (SHG) cavity which provided the 532-nm pump beam to drive the OPO. Travelling wave filter cavities (FC1064 and FC532) in both paths were used to provide stable and well-defined laser beams. Squeezed vacuum states at 1064 nm were generated by type I OPO below threshold in a nonlinear monolithic cavity. A balanced homodyne detector was used to measure the states' quadrature variances. DBS, dichroic beam splitter; PD, photo diode; SA, spectrum analyzer. **(b)**, Exploded assembly drawing of the oven enclosing the squeezed light source. The nonlinear crystal, copper plates, Peltier elements, and thermal insulations are shown. The inlay shows a photograph of the monolithic squeezed light source made from 7% doped MgO:LiNbO₃.

(top trace) vacuum normalized quadrature variances $V_1 = \Delta^2 \hat{X}_1 / \Delta^2 \hat{X}_{1,\text{vac}}$ and $V_2 = \Delta^2 \hat{X}_2 / \Delta^2 \hat{X}_{2,\text{vac}}$, respectively. For a pump power of 30 mW [Fig. 4.2(a)] the squeezed variance (V_1) was 2.9(± 0.1) dB below and the antisqueezed variance (V_2) was 2.9(± 0.1) dB above the vacuum noise level. Within the measurement error bars of ± 0.1 dB the state shows minimum uncertainty and therefore perfect purity. Upon driving the OPO with 150 mW pump power [Fig. 4.2(b)] we observed normalized variances of -6.2(± 0.1) dB and 6.7(± 0.1) dB, respectively. The strongest squeezing level was measured with a pump power of approximately 600 mW [Fig. 4.2(c)]. With this setting 16.0(± 0.1) dB of antisqueezing and a noise reduction of 11.5(± 0.1) dB below the vacuum noise level was achieved.

In practice, squeezed vacuum states generally cannot have perfect purity due to both residual optical loss and residual phase noise. The former results in an admixture of the vacuum state and the latter results in a mixture of phase- space rotated states [4.25, 4.31]. Here, we make the attempt to describe all the three squeezed states measured by a fixed amount of optical loss assuming zero phase noise. This approach is reasonable for the following reasons: (i) previous investigations have shown that our setup is stable and phase noise is low [4.26], (ii) in contrast to squeezing in the audio band [4.32, 4.33], at MHz Fourier frequencies no displaced or thermal states are present that could mix into the state, and (iii) no evidence was found for a non-Gaussian statistic in our measured data. All three pairs of variances observed can then be consistently calculated using $V_i = \eta\gamma V_i' + (1 - \eta\gamma)$, where $V_i' = 1/V_i'$ represent the pure state variances before any decoherence has occurred. Here, $(1 - \eta\gamma)$ represents the overall contribution of the vacuum state, in power. The detection efficiency η accounts for all losses outside the squeezed light source and γ is the OPO cavity escape efficiency accounting for all losses inside the squeezed light source. We find that all of the measured variances (shown in Fig. 4.2) can indeed be modeled by a vacuum noise contribution as low as $(1 - \eta\gamma) = (4.8 \pm 0.2)\%$, independent of the pump power used. This result supports our assumption that phase noise is not significant in our set-up. The loss value of 4.8% is consistent with an independent loss analysis of all the optical components used in our set-up; however, an independent measurement of the quantum efficiency of the photo diodes of the homodyne detector typically has large uncertainties, and we estimate this value to $(98 \pm 2)\%$. Such a low optical loss should enable the observation of more than 13 dB of squeezing; however, pump powers above 600 mW stably controlled and within a clean fundamental mode were not available in our experiment. Note that even though the optical loss was constant throughout our experiments, the purities for the three squeezed states generated were different. For a Gaussian squeezed state the purity is given by $\text{Tr}(\rho^2) = \sqrt{V_1 V_2}$ [4.34], where V_1 and V_2 are again the vacuum noise normalized variances of the squeezed and antisqueezed quadratures, respectively, and ρ is the

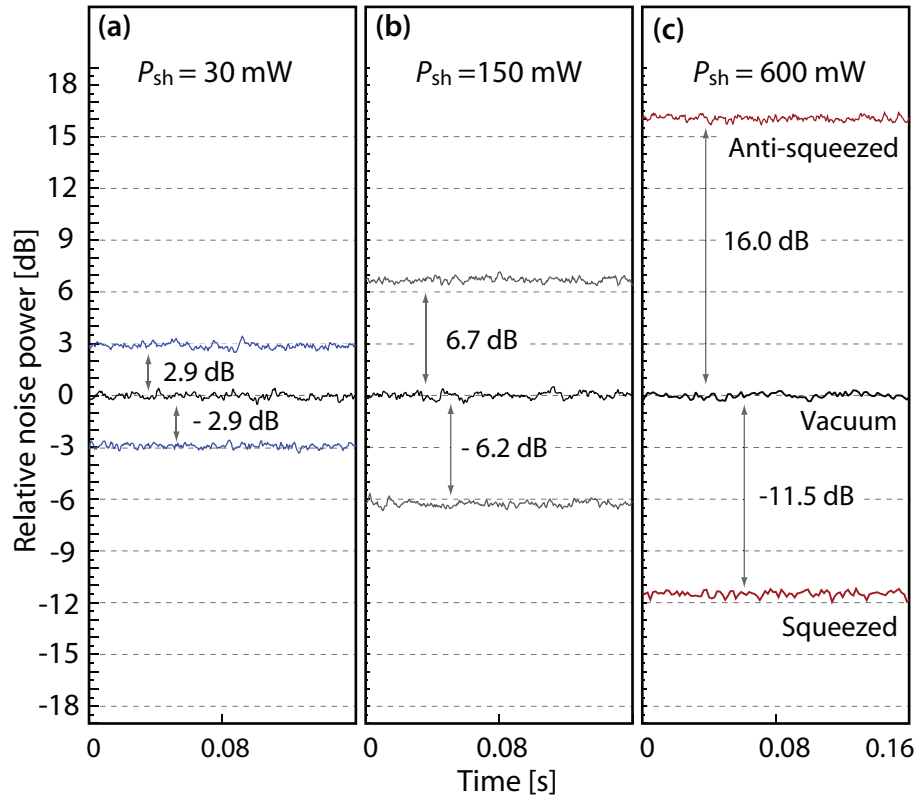


Figure 4.2 — Quadrature noise variances as measured by balanced homodyne detection of three different states produced by the OPO. All traces were recorded at a Fourier frequency of $f=5$ MHz, with a resolution bandwidth of $\Delta f = 100$ kHz and video bandwidth of 100 Hz, and were normalized to the vacuum noise. The data still include electronic detector dark noise; hence all traces represent direct observations without any data postprocessing. (a) Squeezed vacuum state that was generated with a second-harmonic pump power of $P_{sh}=30$ mW. A nonclassical noise reduction of 2.9 dB below vacuum noise was observed, with the respective antisqueezing of 2.9 dB above shot noise. (b), Squeezed vacuum state generated with an increased pump power of $P_{sh}=150$ mW. Squeezing of 6.2 dB was measured with 6.7 dB of antisqueezing. (c), Driving the OPO at maximum pump power $P_{sh}=600$ mW yielded squeezing and antisqueezing of 11.5 dB and 16.0 dB, respectively. The subtraction of the detector dark noise would further increase the value of maximum squeezing to 11.6 dB.

density matrix of the quantum state. Assume a pure state with 3.05 dB (initial) squeezing. Then 4.8% optical loss impairs the squeezing strength resulting in a state with 2.84 dB squeezing and 2.94 dB antisqueezing. Taking into account the accuracy of our measurements, these values agree well with the measurements shown in Fig. 4.2(a). According to the aforementioned formula, the first measured state had a purity of about 0.99. For the states in Fig. 4.2(b) and (c) one finds the purity of 0.94 and 0.60, respectively. Despite constant loss the most strongly squeezed state shows the lowest purity; however, considering the squeezing strength, the value of 0.6 still reflects a relatively high purity.

Figure 4.3 presents the Wigner function [4.28, 4.29, 4.35] of the squeezed vacuum state with variances of -11.5 dB and 16 dB with respect to the vacuum noise variance. The Wigner function represents one of several possible phase-space probability distributions for quantum states. Since it is Gaussian for squeezed vacuum-squeezed states, it is particularly easy to obtain simply by measuring its second moments. The entire statistical properties of the state can then be summarized in a finite dimensional space, namely, by the covariance matrix. Hence, for squeezed vacuum states mixed with the ordinary vacuum state only the variances of the squeezed and antisqueezed quadrature are required to calculate the Wigner function which is then given by

$$W(X_1, X_2) = \frac{(4\pi)^{-1}}{\sqrt{\Delta^2 \hat{X}_1 \Delta^2 \hat{X}_2}} \exp\left(\frac{-\frac{1}{2} X_1^2}{\Delta^2 \hat{X}_1} + \frac{-\frac{1}{2} X_2^2}{\Delta^2 \hat{X}_2}\right),$$

where $\Delta^2 \hat{X}_i$ are again the variances of the quadratures X_1 and X_2 , respectively, with the vacuum noise variance of $1/4$. The vertical axis in Fig. 4.3 represents the quasiprobability density of the quadrature phase space. The Wigner function is a phase-space quasiprobability distribution, since the quadratures cannot simultaneously have precisely defined values. What *can* be precisely measured is one projection of the Wigner function onto the axis of the phase space at a time. The projections are the probability distributions of the particular quadrature and, here, have a Gaussian shape with squeezed or antisqueezed variances with respect to the vacuum noise variance (dotted curves). Contour lines of the Wigner function have an elliptical shape and are thus squeezed in comparison with the circular contour lines of the vacuum state (not shown in Fig. 4.3).

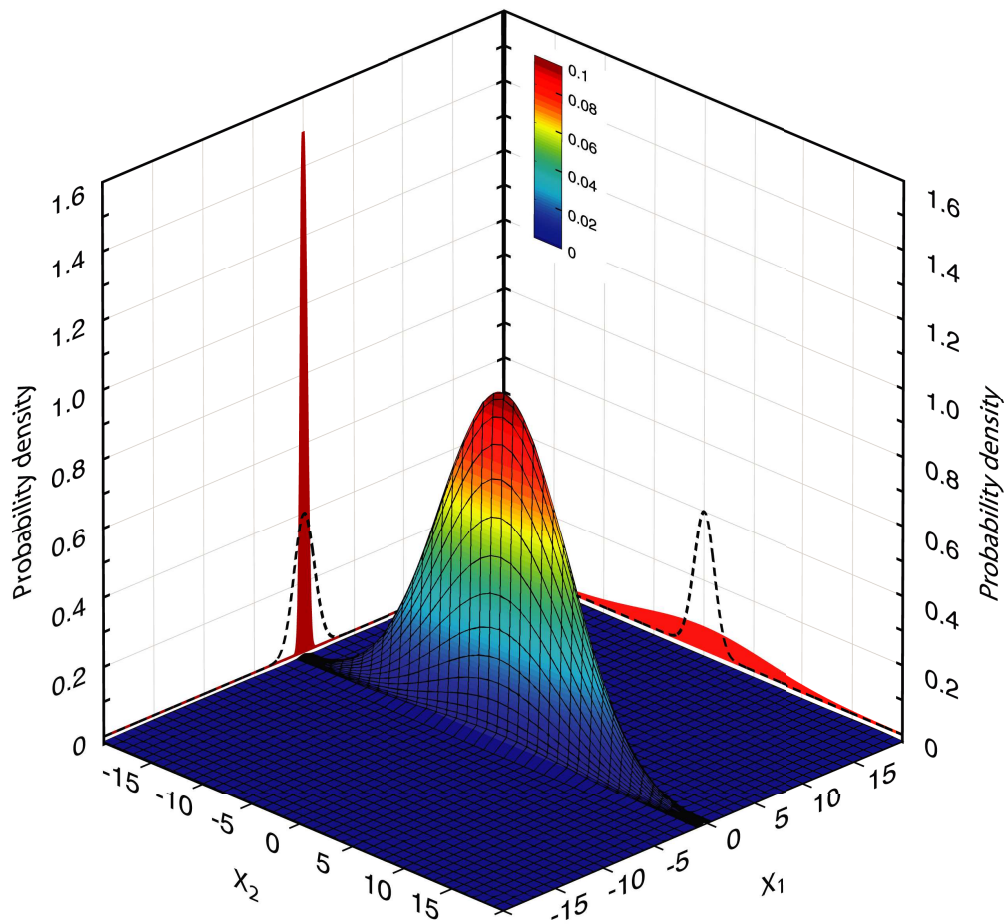


Figure 4.3 — Wigner function of the squeezed vacuum state produced by our OPO. The projections (solid curves) onto the two quadratures yield the gaussian probability distributions with variances of -11.5 dB and 16 dB relative to the projections belonging to a pure vacuum state (dotted curves).

4.4 Squeezed vacuum states in the photon-number basis

All photons that are present in a squeezed vacuum state produced by OPO stem from parametric down-conversion of second-harmonic pump photons. This is also true for a mixture of a squeezed vacuum state with an ordinary vacuum state. For strongly squeezed states not just the detection of photon pairs but also of higher-order photon pairs is expected. However, the overall loss of photons must be sufficiently low to enable such an observation. Since the Wigner function represents the full quantum information of a state it can be used to calculate the state’s density matrix $\rho_{n,m}$ in the photon-number (Fock) basis, which is another complete description of the state. The photon-number distribution $P(n)$ can be obtained from the diagonal elements of the density matrix. Figure 4.4 shows a plot of the first matrix elements (absolute values) up to photon numbers $n, m = 10$ of the observed squeezed state with noise variances of -11.5 dB and 16 dB relative to the vacuum noise. In order to calculate the density matrix [4.21, 4.36] photon numbers of up to $n = m = 170$ were considered, which ensured convergence of all the matrix elements. Similarly, the density matrices for the additional two states have also been generated. Their

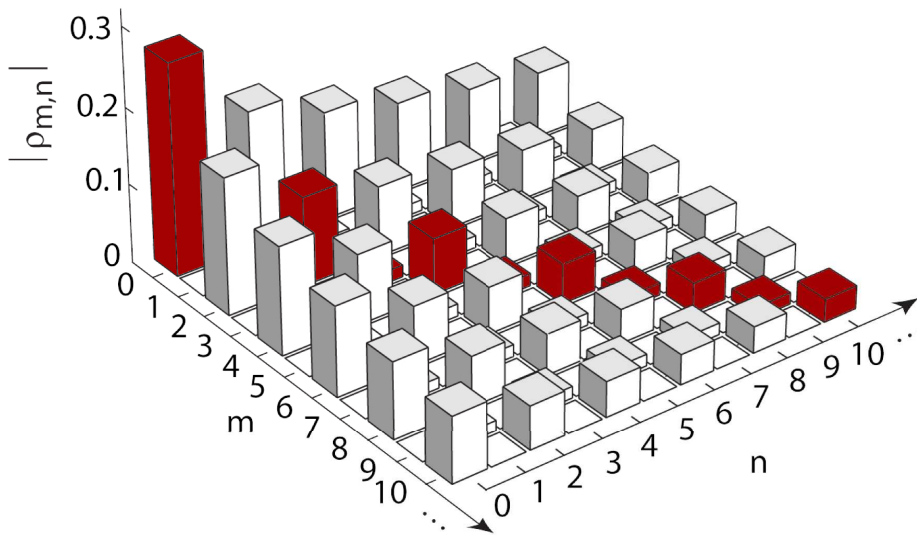


Figure 4.4 — Density matrix of the squeezed state of Fig. 4.2(c). Plot of the absolute values of the density matrix elements with photon numbers up to 10 for the -11.5 -dB squeezed and 16 -dB antisqueezed state. The diagonal elements give the probabilities of finding $0, 1, 2, \dots, n$ photons. Due to the state’s high purity, the probabilities for finding an odd number of photons is significantly suppressed.

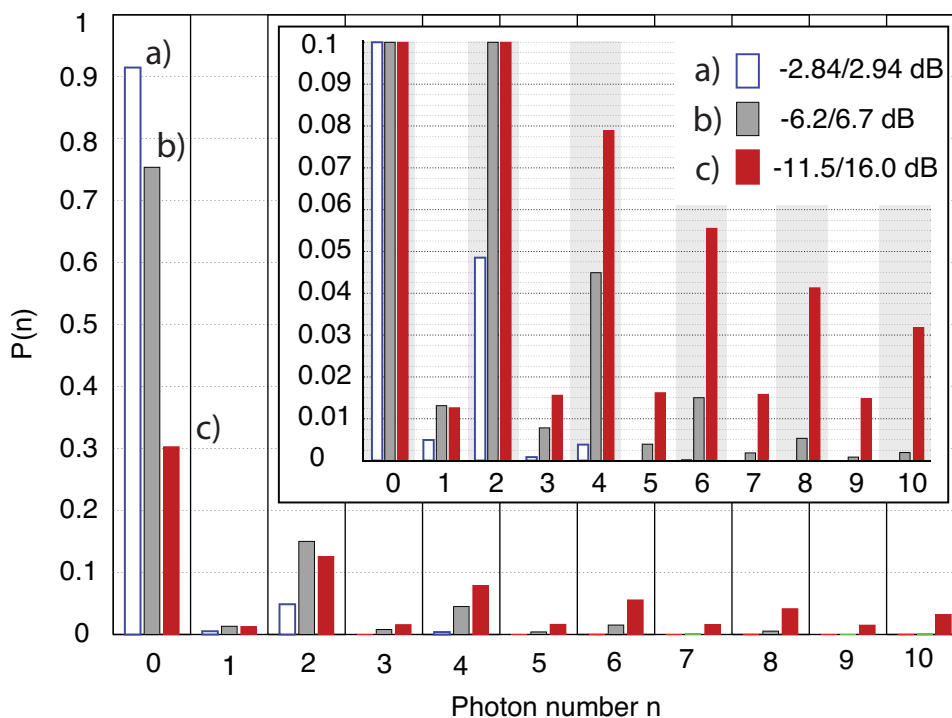


Figure 4.5 — Photon-number oscillation. The probability $P(n)$ of detecting n photons is plotted for the squeezed vacuum states from Figs. 4.2(a), 4.2(b), and 4.2(c). The photon-number distributions clearly show oscillatory behavior. With increasing squeezing the number of higher-order photon pairs grows. For clarity the inset shows a zoomed view restricted to probabilities up to 0.1.

diagonal elements, that is, the photon-number distributions of the states, are depicted in Fig. 4.5. The formula used and the numerical values of the density matrix elements are given in the Appendix. For the 11.5-dB squeezed state a strong odd/even photon-number oscillation is visible. Even the probability of detecting $n = 10$ photons is significantly higher than the probability of detecting $n = 9$ photons. This oscillation further continues for greater photon numbers but is not shown here. For our squeezed states with less squeezing the oscillation flattens out at lower photon numbers, but the odd/even oscillation is even more pronounced at lower photon numbers. For the 2.9-dB squeezed state the probability of finding $n = 1$ photon is as small as 0.5%. Note that for *displaced* squeezed states additional photons are added to the state and the odd photon numbers cannot all have zero probability, even if these state are pure. However, *weakly displaced* squeezed states show photon-number oscillations with larger periods. Such states were originally theoretically analyzed in [4.37].

The photon numbers calculated here are detected per bandwidth in hertz and per detection time interval in seconds. Obviously, the higher the squeezing bandwidth the higher the number of photons per second.

4.5 Observation of high-bandwidth squeezing

For applications in high-speed quantum communication and information processing high photon counting rates or, equivalently, fields with squeezing over a broad Fourier spectrum are essential. The half-width half-maximum (HWHM) *squeezing bandwidth* can be defined as the spectral width over which the squeezed variance increases from its lowest variance at small Fourier frequencies V_1 to $V_1 + 0.5 \cdot (1 - V_1)$. Here the variances are again normalized to unity vacuum noise. Although continuous variable quantum states are often quoted to provide the possibility of high bandwidths, only modest values of the order of a few tens of MHz have been realized (see, for example, Refs. [4.27, 4.38]). Figure 4.6 shows the spectral analysis of the strongly squeezed field from our source with a HWHM squeezing bandwidth of 170 MHz. In contrast to Fig. 4.2, here the electronic dark noise of our homodyne detector was subtracted. At ~ 100 MHz the dark noise reached the measured quantum noise. At frequencies below 5 MHz the measurement was limited by the resolution bandwidth chosen. Since our set-up did not use control beams which might introduce technical noise at low frequencies, a white squeezing spectrum can be expected for lower frequencies if parasitic interferences with frequency-shifted scattered photons are sufficiently suppressed as demonstrated in Refs. [4.32, 4.33].

The spectrum of the squeezed and antisqueezed quadrature variances (V_1 and V_2 , respectively) for the below-threshold OPO can be calculated by [4.25]

$$V_{1,2} = 1 \pm \eta\gamma \frac{4\sqrt{P_{sh}/P_{th}}}{(1 \mp \sqrt{P_{sh}/P_{th}})^2 + 4K^2}, \quad (4.2)$$

where P_{sh} is the power of the second-harmonic pump and P_{th} is the pump power needed to reach the OPO threshold. The detection efficiency η is calculated as the product of the propagation efficiency, the square of the homodyne visibility, and the quantum efficiency of the homodyne detector photo diodes. The OPO escape efficiency $\gamma = T/(T + L)$ is determined by the transmittance T of the out-coupling mirror and the intracavity round-trip loss L . The dimensionless parameter $K = 2\pi f/\kappa$ is the ratio of the Fourier frequency f and the decay rate $\kappa = (T + L)c/l$ of the cavity with round-trip length l . The theoretical curves in Fig. 4.6 were modeled using equation (4.2), with the best agreement obtained upon assumption of the following

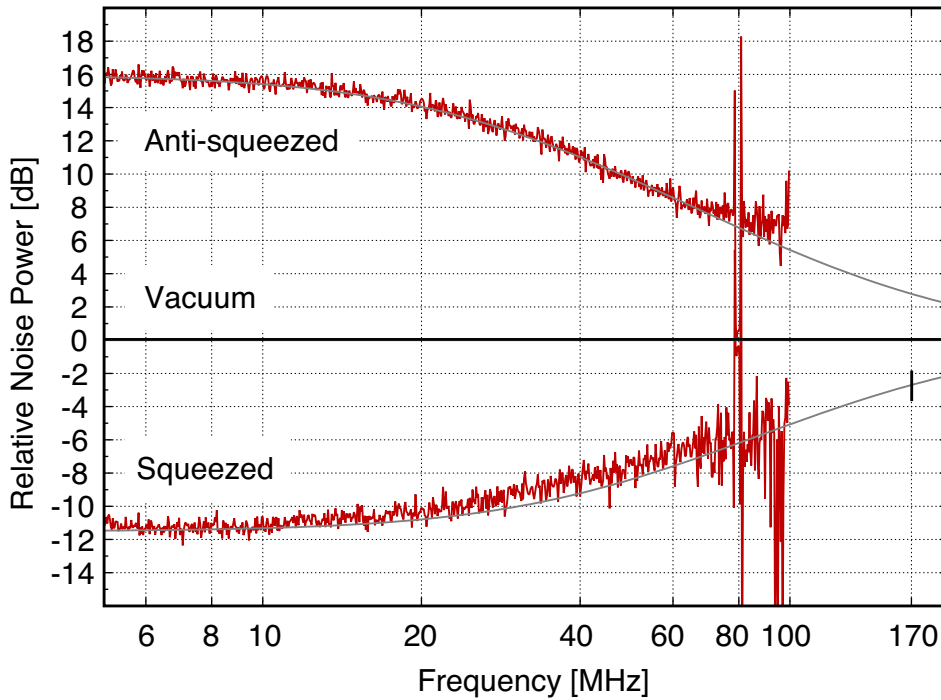


Figure 4.6 — High bandwidth squeezing spectrum. Squeezing (bottom trace) and anti-squeezing (top trace) are shown relative to the vacuum noise variance. The measurements were performed from 5 MHz to 100 MHz. This was limited by the fact that the dark noise clearance of the homodyne detector was too low towards higher frequencies. The traces are averages of 3 measurements each done with a resolution bandwidth of 1 MHz and video bandwidth of 3 kHz. The data was fitted to a model and revealed a squeezing bandwidth of 170 MHz (thin line).

values: a pump beam at 53.5% of the threshold power, the output coupler transmittance of 12%, the round-trip loss within the crystal of approximately 0.1%, and a total detection efficiency $\eta\gamma=95.2\%$ in agreement with our analysis presented in Sec. 4.3. The squeezing bandwidth of our source is given by the Fourier frequency where the squeezed variance has increased to -2.7 dB. According to the theoretical curve in Fig. 4.6 this bandwidth is 170 MHz. This result can be used to calculate the rate of down-converted photons from a full longitudinal mode of our source. To this end, we split the half free spectral range of our source of 5.5 GHz into 55000 frequency bins of 100 kHz each. For every bin i , the photon-number distribution $P_i(n)$ was calculated. By summing these distributions, we find that the spectrally weighted representative photon-number distribution of the central OPO cavity mode around half the pump light frequency $P_f(n) = 1/55000 \cdot \sum_i P_i(n)$. This distribution can now be used to

calculate the mean number of photons per second and bandwidth averaged over the band of 5.5 GHz. Multiplying with 5.5 GHz provides the rate of down-converted photons from this mode of as high as $2.79 \times 10^8 \text{s}^{-1}$, corresponding to a power of 52 pW.

Another relevant value is given by the mean number of correlated photons in the case of a single-photon detection. For a parametric down-conversion source operated far below its threshold and with zero photon loss this number is two because the detection of a single photon proves the presence of, in total, two photons. In order to calculate this number for our source we set $P_f(0) = 0$ and calculate the mean value of the renormalized remaining distribution. For the 11.5-dB squeezed state presented in Fig. 4.6 we obtain $\langle n \rangle_f = 5.93$. Implying that whenever a single-photon detector clicks (possibly without any photon-number resolution) this event proves the presence of, on average, almost six quantum-correlated photons, including the detected photon(s).

4.6 Conclusion

In order to observe strong squeezing levels, we operated an optical parametric oscillator comparatively close to its threshold. In this regime not just single-photon pairs, but a significant number of multiple or *higher-order* photon pairs were produced. This contrasts typical parametric down-conversion experiments in the photon counting regime where the probability of observing more than two quantum-correlated photons is negligible. The density matrix in the photon-number basis of our -11.5 -dB squeezed state not only reveals strong photon-number oscillations but also quantum correlations between photons in the following way: Whenever a photon was photoelectrically detected by the homodyne detector, there was an almost unity probability that an additional odd number of photons were physically realized and were detected by the same detector. In photon counting experiments our squeezed state might therefore be used to overcome the problem of insufficient photon counter efficiencies. The quality of our squeezed states will also enable a great step forward in many applications currently under discussion. In high-power laser interferometers for gravitational wave detection [4.4–4.6] the application of an -11.5 -dB squeezed state reduces the shot noise equivalent to a laser power increase by a factor 14. The interference of two such states on a 50-50 beamsplitter would produce strong Einstein-Podolsky-Rosen entanglement [4.12, 4.13, 4.39] and its high bandwidth may result in the ultrafast generation of quantum keys [4.40]. Our squeezed light source may also find applications in future hybrid quantum information networks. Its well-defined fundamental

Gaussian spatial mode yielded a high fringe contrast with a spatially filtered local oscillator of 99.8% and enables efficient coupling to other systems, for example to atoms coupled to optical cavities [4.41–4.43], in order to realize quantum interfaces of light and matter.

ACKNOWLEDGEMENTS

We would like to thank B. Hage, J. DiGuglielmo, A. Thüring, C. Messenger and J. Fiurášek for many helpful discussions. This work has been supported by the Deutsche Forschungsgemeinschaft (DFG) through Sonderforschungsbereich 407 and the Centre for Quantum Engineering and Space-Time Research QUEST.

APPENDIX

In order to calculate the density matrix elements $\rho_{m,n}$ we followed the prescription given in Ref. [4.36], whereby the entries can be obtained using the following equation:

$$\rho_{m,n} = \sqrt{\frac{m!n!}{\tilde{V}_x\tilde{V}_p}} \sum_a \frac{(-T)^{[(m-n)/2]+2a} U^{n-2a}}{a!(n-2a)! \left(a + \frac{m-n}{2}\right)!}, \quad (4.3)$$

where $\tilde{V}_x = V_x + 1/2$, $\tilde{V}_p = V_p + 1/2$, $U = 1 - \frac{1}{2\tilde{V}_x} - \frac{1}{2\tilde{V}_p}$ and $T = \frac{1}{4\tilde{V}_x} - \frac{1}{4\tilde{V}_p}$. Note that V_x and V_p correspond to the linear quadrature variances of the quantum state as introduced in Eq. (4.2), but with the vacuum variance set to 1/2. This expression for the density matrix in the Fock state basis can be derived from the covariance matrix by first noting that the Husimi Q -function in the coherent state basis is the generating function for the density matrix in the Fock state basis. The covariance matrix needs to be transformed from the quadrature basis into the coherent basis to obtain the aforementioned formula.

We calculated $\rho_{m,n}$ for the three states in Figs.4.2(a)– 4.2(c). For the first state [Fig.4.2(a)] we chose vacuum normalized variances of -2.84 dB and 2.94 dB being within our experimental error bars. These numbers correspond to an originally pure state with 3.05 dB of squeezing and 3.05 dB antisqueezing that was degraded by 4.8% of optical loss. For the remaining two states we chose the variances according to the values in Fig. 4.2(b) (-6.2 dB and 6.7 dB) and Fig. 4.2(c) (-11.5 dB and 16.0 dB). The calculation was done with photon numbers up to 170 to ensure the convergence of all entries, but the respective density matrices $\rho^{(a)}$, $\rho^{(b)}$, and $\rho^{(c)}$ presented below were truncated at $n=m=10$. For clarity the diagonal elements representing the photon number distribution (as shown in Fig. 4.5) are printed in bold red.

68 STRONG SQUEEZING AT 1064 NM FROM A MONOLITHIC SQUEEZED
LIGHT RESONATOR 4.6

$$\rho^{(a)} = \begin{bmatrix} \mathbf{.9416} & 0 & -.2137 & 0 & .0594 & 0 & -.0174 & 0 & .0052 & 0 & -.0016 \\ 0 & \mathbf{.0049} & 0 & -.0019 & 0 & .0007 & 0 & -.0002 & 0 & .0001 & 0 \\ -.2137 & 0 & \mathbf{.0485} & 0 & -.0135 & 0 & .0040 & 0 & -.0012 & 0 & .0004 \\ 0 & -.0019 & 0 & \mathbf{.0008} & 0 & -.0003 & 0 & .0001 & 0 & 0 & 0 \\ .0594 & 0 & -.0135 & 0 & \mathbf{.0038} & 0 & -.0011 & 0 & .0003 & 0 & -.0001 \\ 0 & .0007 & 0 & -.0003 & 0 & \mathbf{.0001} & 0 & 0 & 0 & 0 & 0 \\ -.0174 & 0 & .0040 & 0 & -.0011 & 0 & \mathbf{.0003} & 0 & -.0001 & 0 & 0 \\ 0 & -.0002 & 0 & .0001 & 0 & 0 & 0 & \mathbf{0} & 0 & 0 & 0 \\ .0052 & 0 & -.0012 & 0 & .0003 & 0 & -.0001 & 0 & \mathbf{0} & 0 & 0 \\ 0 & .0001 & 0 & 0 & 0 & 0 & 0 & 0 & 0 & \mathbf{0} & 0 \\ -.0016 & 0 & .0004 & 0 & -.0001 & 0 & 0 & 0 & 0 & 0 & \mathbf{0} \end{bmatrix}$$

$$\rho^{(b)} = \begin{bmatrix} \mathbf{.7538} & 0 & -.3360 & 0 & .1834 & 0 & -.1056 & 0 & .0622 & 0 & -.0372 \\ 0 & \mathbf{.0131} & 0 & -.0101 & 0 & .0071 & 0 & -.0048 & 0 & .0032 & 0 \\ -.3360 & 0 & \mathbf{.1500} & 0 & -.0820 & 0 & .0473 & 0 & -.0279 & 0 & .0167 \\ 0 & -.0101 & 0 & \mathbf{.0078} & 0 & -.0055 & 0 & .0037 & 0 & -.0025 & 0 \\ .1834 & 0 & -.0820 & 0 & \mathbf{.0449} & 0 & -.0259 & 0 & .0153 & 0 & -.0092 \\ 0 & .0071 & 0 & -.0055 & 0 & \mathbf{.0039} & 0 & -.0026 & 0 & .0018 & 0 \\ -.1056 & 0 & .0473 & 0 & -.0259 & 0 & \mathbf{.0150} & 0 & -.0089 & 0 & .0053 \\ 0 & -.0048 & 0 & .0037 & 0 & -.0026 & 0 & \mathbf{.0018} & 0 & -.0012 & 0 \\ .0622 & 0 & -.0279 & 0 & .0153 & 0 & -.0089 & 0 & \mathbf{.0053} & 0 & -.0032 \\ 0 & .0032 & 0 & -.0025 & 0 & .0018 & 0 & -.0012 & 0 & \mathbf{.0008} & 0 \\ -.0372 & 0 & .0167 & 0 & -.0092 & 0 & .0053 & 0 & -.0032 & 0 & \mathbf{.0019} \end{bmatrix}$$

$$\rho^{(c)} = \begin{bmatrix} \mathbf{.3026} & 0 & -.1946 & 0 & .1532 & 0 & -.1272 & 0 & .1082 & 0 & -.0933 \\ 0 & \mathbf{.0126} & 0 & -.0140 & 0 & .0143 & 0 & -.0140 & 0 & .0135 & 0 \\ -.1946 & 0 & \mathbf{.1256} & 0 & -.0993 & 0 & .0828 & 0 & -.0707 & 0 & .0613 \\ 0 & -.0140 & 0 & \mathbf{.0156} & 0 & -.0159 & 0 & .0157 & 0 & -.0151 & 0 \\ .1532 & 0 & -.0993 & 0 & \mathbf{.0789} & 0 & -.0660 & 0 & .0566 & 0 & -.0493 \\ 0 & .0143 & 0 & -.0159 & 0 & \mathbf{.0162} & 0 & -.0160 & 0 & .0155 & 0 \\ -.1272 & 0 & .0828 & 0 & -.0660 & 0 & \mathbf{.0555} & 0 & -.0478 & 0 & .0417 \\ 0 & -.0140 & 0 & .0157 & 0 & -.0160 & 0 & \mathbf{.0158} & 0 & -.0153 & 0 \\ .1082 & 0 & -.0707 & 0 & .0566 & 0 & -.0478 & 0 & \mathbf{.0413} & 0 & -.0362 \\ 0 & .0135 & 0 & -.0151 & 0 & .0155 & 0 & -.0153 & 0 & \mathbf{.0148} & 0 \\ -.0933 & 0 & .0613 & 0 & -.0493 & 0 & .0417 & 0 & -.0362 & 0 & \mathbf{.0318} \end{bmatrix}$$

References

- [4.1] M. Xiao, L. A. Wu, and H. J. Kimble, "Precision measurement beyond the shot-noise limit," *Phys. Rev. Lett.* **59**, 278 (1987).
- [4.2] P. Grangier, R. E. Slusher, B. Yurke, and A. LaPorta, "Squeezed-light-enhanced polarization interferometer," *Phys. Rev. Lett.* **59**, 2153 (1987).
- [4.3] K. McKenzie, D. A. Shaddock, D. E. McClelland, B. C. Buchler, and P. K. Lam, "Experimental Demonstration of a Squeezing-Enhanced Power-Recycled Michelson Interferometer for Gravitational Wave Detection," *Phys. Rev. Lett.* **88**, 231102 (2002).
- [4.4] P. Walther *et al.*, "De Broglie wavelength of a non-local four-photon state," *Nature* **429**, 158 (2004).
- [4.5] H. Vahlbruch *et al.*, "Demonstration of a Squeezed-Light-Enhanced Power- and Signal-Recycled Michelson Interferometer," *Phys. Rev. Lett.* **95**, 211102 (2005).
- [4.6] K. Goda *et al.*, "A quantum-enhanced prototype gravitational-wave detector," *Nature Phys.* **4**, 472–476 (2008).
- [4.7] A. Einstein, B. Podolsky, and N. Rosen, "Can quantum-mechanical description of physical reality be considered complete?", *Phys. Rev.* **47**, 777–780 (1935).
- [4.8] A. Aspect, P. Grangier, and G. Roger, "Experimental Tests of Realistic Local Theories via Bell's Theorem," *Phys. Rev. Lett.* **47**, 460–463 (1981).
- [4.9] Z. Y. Ou, S. F. Pereira, H. J. Kimble, and K. C. Peng, "Realization of the Einstein-Podolsky-Rosen paradox for continuous variables," *Phys. Rev. Lett.* **68**, 3663–3666 (1992).
- [4.10] K. Wagner *et al.*, "Entangling the Spatial Properties of Laser Beams," *Science* **321**, 541 (2008).
- [4.11] D. Bouwmeester *et al.*, "Experimental quantum teleportation," *Nature* **390**, 575–579 (1997).
- [4.12] A. Furusawa *et al.*, "Unconditional quantum Teleportation," *Science* **282**, 706–709 (1998).
- [4.13] W. P. Bowen *et al.*, "Experimental investigation of continuous-variable quantum teleportation," *Phys. Rev. A* **67**, 032302 (2003).

- [4.14] A. Ourjoumtsev, R. Tualle-Brouiri, J. Laurat, and P. Grangier, "Generating Optical Schrödinger Kittens for Quantum Information Processing," *Science* **312**, 83 (2006).
- [4.15] J. S. Neergaard-Nielsen, B. Melholt Nielsen, C. Hettich, K. Mølmer, and E. S. Polzik, "Generation of a Superposition of Odd Photon Number States for Quantum Information Networks," *Phys. Rev. Lett.* **97**, 083604 (2006).
- [4.16] R. Ursin *et al.*, "Entanglement-based quantum communication over 144 km," *Nature Phys.* **3**, 481–486 (2007).
- [4.17] R. Dong *et al.*, "Experimental entanglement distillation of mesoscopic quantum states," *Nature Phys.* **4**, 919–923 (2008).
- [4.18] B. Hage *et al.*, "Preparation of distilled and purified continuous-variable entangled states," *Nature Phys.* **4**, 915–918 (2008).
- [4.19] D. F. Walls, "Squeezed states of light," *Nature* **306**, 141 (1983).
- [4.20] G. Breitenbach, S. Schiller, and J. Mlynek, "Measurement of the quantum states of squeezed light," *Nature* **387**, 471–475 (1997).
- [4.21] C. C. Gerry, and P. L. Knight, *Introductory Quantum Optics* (Cambridge Univ. Press, Cambridge, 2004).
- [4.22] H. P. Yuen, "Two-photon coherent states of the radiation field," *Phys. Rev. A* **13**, 2226–2243 (1976).
- [4.23] V. V. Dodonev, O. V. Manko, and V. I. Manko, "Photon distribution for one-mode mixed light with a generic Gaussian Wigner function," *Phys. Rev. A* **49**, 2993–2001 (1994).
- [4.24] R. Dong *et al.*, "Experimental evidence for Raman-induced limits to efficient squeezing in optical fibers," *Opt. Lett.* **33**, 116 (2008).
- [4.25] Y. Takeno, M. Yukawa, H. Yonezawa, and A. Furusawa, "Observation of -9 dB quadrature squeezing with improvement of phase stability in homodyne measurement," *Opt. Express* **15**, 4321–4327 (2007).
- [4.26] H. Vahlbruch *et al.*, "Observation of Squeezed Light with 10-dB Quantum-Noise Reduction," *Phys. Rev. Lett.* **100**, 33602 (2008).

- [4.27] G. Breitenbach, T. Müller, S. F. Pereira, S. Schiller, and J. Mlynek, "Squeezed vacuum from a monolithic optical parametric oscillator," *J. Opt. Soc. Am. B* **12**, 2304 (1995).
- [4.28] K. Vogel and H. Risken, "Determination of quasiprobability distributions in terms of probability distributions for the rotated quadrature phase," *Phys. Rev. A* **40**, 2847–2849 (1989).
- [4.29] J. Bertrand and P. Bertrand, "A tomographic approach to Wigner's function," *Found. Phys.* **17**, 397–405 (1987).
- [4.30] S. Schiller, G. Breitenbach, S. F. Pereira, T. Müller, and J. Mlynek, "Quantum statistics of the squeezed vacuum by measurement of the density matrix in the number state representation," *Phys. Rev. Lett.* **77**, 2933–2936 (1996).
- [4.31] A. Franzen, B. Hage, J. DiGuglielmo, J. Fiurášek, and R. Schnabel, "Experimental Demonstration of Continuous Variable Purification of Squeezed States," *Phys. Rev. Lett.* **97**, 150505 (2006).
- [4.32] H. Vahlbruch *et al.*, "Coherent Control of Vacuum Squeezing in the Gravitational-Wave Detection Band," *Phys. Rev. Lett.* **97**, 011101 (2006).
- [4.33] H. Vahlbruch, S. Chelkowski, K. Danzmann, and R. Schnabel, "Quantum engineering of squeezed states for quantum communication and metrology," *New J. Phys.* **9**, 371 (2007).
- [4.34] M. G. A. Paris, F. Illuminati, A. Serafini, and S. De Siena, "Purity of Gaussian states: Measurement schemes and time evolution in noisy channels," *Phys. Rev. A* **68**, 012314 (2003).
- [4.35] E. P. Wigner, "On the Quantum Correction For Thermodynamic Equilibrium," *Phys. Rev.* **40**, 749–759 (1932).
- [4.36] P. Marek *et al.*, "Multiple-copy distillation and purification of phase-diffused squeezed states," *Phys. Rev. A* **76**, 053820 (2007).
- [4.37] W. Schleich and J. A. Wheeler, "Oscillations in photon distribution of squeezed states and interference in phase space," *Nature* **326**, 574–577 (1987).
- [4.38] S. Chelkowski, H. Vahlbruch, K. Danzmann, and R. Schnabel, "Coherent control of broadband vacuum squeezing," *Phys. Rev. A* **75**, 043814 (2007).

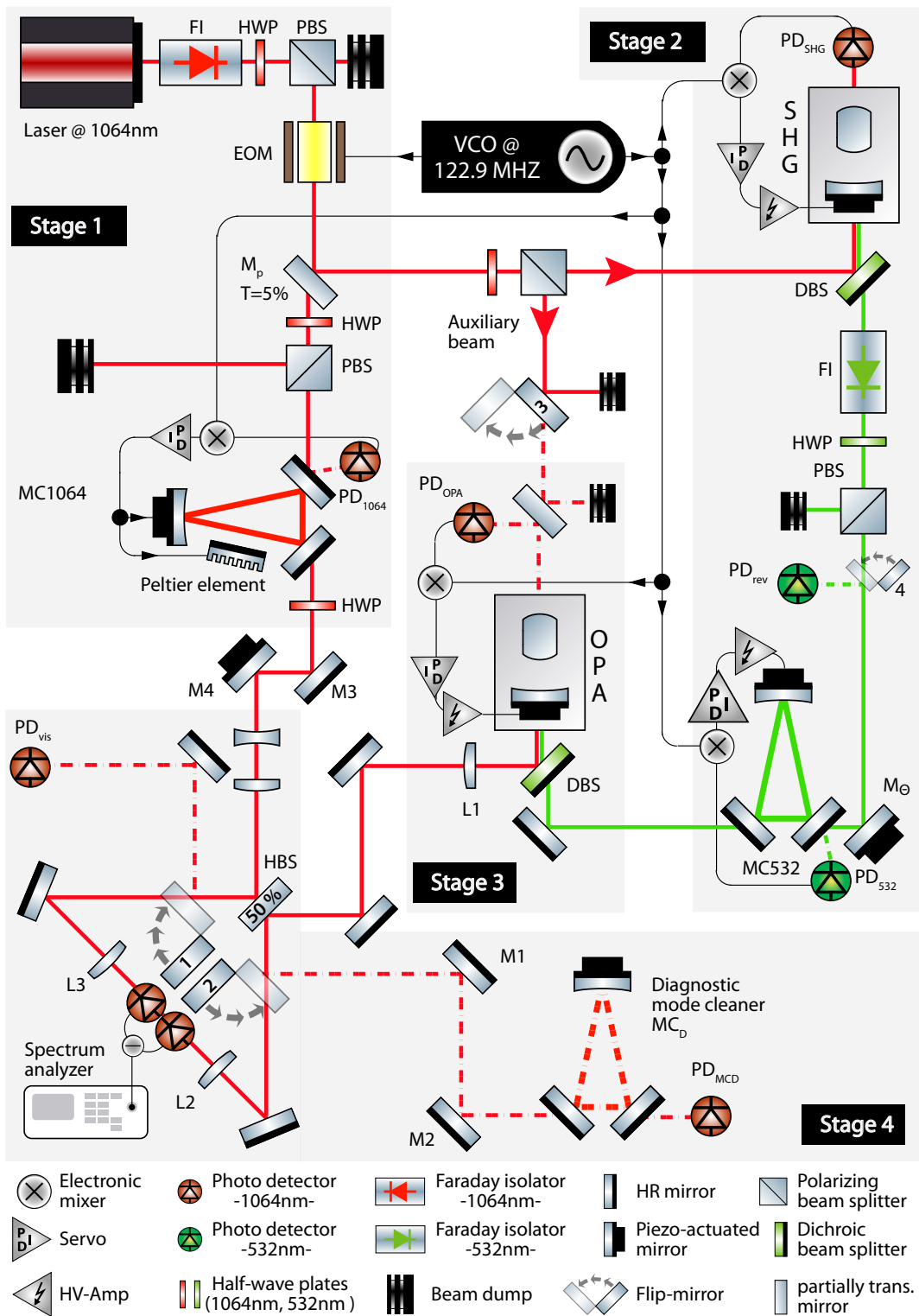
- [4.39] J. DiGuglielmo, B. Hage, A. Franzen, J. Fiurášek, and R. Schnabel, "Experimental characterization of Gaussian quantum-communication channels," *Phys. Rev. A* **76**, 012323 (2007).
- [4.40] N. J. Cerf, M. Lévy, and G. Van Assche, "Quantum distribution of Gaussian keys using squeezed states," *Phys. Rev. A* **63**, 052311 (2001).
- [4.41] M. D. Lukin, S. F. Yelin, and M. Fleischhauer, "Entanglement of Atomic Ensembles by Trapping Correlated Photon States," *Phys. Rev. Lett.* **84**, 4232–4235 (2000).
- [4.42] J. Simon, H. Tanji, J. K. Thompson, and V. Vuletić, "Interfacing Collective Atomic Excitations and Single Photons," *Phys. Rev. Lett.* **98**, 183601 (2007).
- [4.43] P. F. Herskind, A. Dantan, J. P. Marler, M. Albert, and M. Drewsen, "Realization of collective strong coupling with ion Coulomb crystals in an optical cavity.," *Nature Phys.* **5**, 494–498 (2009).

Strong squeezing as an estimator for optical loss

In Sec. 3.3.1 the effect of optical loss on the measured squeezing level was theoretically investigated. It was shown that especially large factors of noise suppression are considerably degraded even by small amounts of additional optical loss. Consequently, the measurement of strong squeezing can be utilized to precisely infer the total optical loss in the system. This chapter presents how this can in particular be exploited to deduce the quantum efficiency of photo diodes with high accuracy.

5.1 Introduction

The total efficiency with which squeezed states can be detected is given as the product of the inefficiencies that occur once the squeezing is produced. As already described in Sec. 3.3 these can basically be divided into the escape efficiency η_{esc} , the propagation efficiency η_{prop} , the homodyne efficiency η_{homo} , and the quantum efficiency η_{qe} . Consequently, in the case that all but one loss terms are known, the remaining term can be derived from the total loss budget. The accuracy of that procedure only depends on the uncertainty of the known parameters. Usually, the biggest unknown is the quantum efficiency of the photo diodes. To determine the quantum efficiency or the responsivity of a photo diode, a measurement on the absolute power of the incident light beam needs to be carried out. Absolute power measurements can be performed with power meters. Commercially available power meters typically have absolute errors of ± 2 up to ± 5 % [5.1–5.3] such that the value for the quantum efficiency is



equally prone to large errors. The use of the level of squeezing as an estimator for the optical loss is more promising since only relative power measurements are involved. However, it was shown in Sec. 3.3.4 that an insufficient stability of the phase between the homodyne local oscillator and the signal field will also degrade the measured squeezing. It is therefore important to distinguish between those two effects.

5.2 Experimental setup

The experimental setup can be divided into four main stages: laser preparation (1), pump field preparation (2), generation of squeezed vacuum states (3), and detection of squeezed vacuum states (4). The stages are indicated in the schematic shown in Fig. 5.1 and are described in more detail below.

5.2.1 Laser preparation

The light source in our setup was a diode-pumped, monolithic non-planar Nd:YAG ring laser (*Mephisto* by *Innolight*). The output was about 2 W of continuous-wave single mode radiation at 1064 nm. A Faraday isolator was incorporated to prevent retro-reflections into the laser. The combination of half-wave plate (HWP) and polarizing beam splitter (PBS) was used to adjust the overall input power. In a next step a phase modulation was imprinted onto the light by means of a home-made, resonantly enhanced electro-optical modulator (EOM). The modulation frequency of 122.9 MHz was provided by a voltage controlled oscillator (VCO). Subsequently, a partially transmissive mirror with 95% reflectivity split the beam into two parts. The transmitted beam was mode-matched to the TEM_{00} mode of a mode-cleaning filter cavity (MC1064). As shown in Fig. 5.2 this filter cavity was designed as a Fabry-Pérot ring-cavity composed of three mirrors that were rigidly attached to an aluminum spacer. The transmissivity of the two plane/plane mirrors (M1 and M2)

Figure 5.1 (preceding page) — Schematic of the experimental setup. A detailed description of the four stages is given in the text. The first stage included preparing a local oscillator beam and providing an input field to the second-harmonic generator. In the second stage, the pump field for the parametric down-conversion process was generated from the infrared light by frequency doubling. The generation of squeezed vacuum states in a hemilithic optical parametric amplifier (OPA) is described in stage three, and in stage four the quadrature variances are measured with a balanced homodyne detector.



Figure 5.2 — CAD drawing of the mode cleaner cavities MC1064 and MC532. The geometric layout of the spacer and the radius of curvature of M3 was equal for cavities operating at 1064 nm and 532 nm. The cavity round-trip length is 42 cm and the resulting $\text{FSR} \approx 714$ MHz. The reflectivities of the plane/plane mirrors for different polarization and wavelengths lead to the following values for the Finesse \mathcal{F} and the (FWHM) linewidth ν . **MC1064:** $\mathcal{F}_p \approx 280$, $\nu_p \approx 2.5$ MHz, and $\mathcal{F}_s \approx 4200$, $\nu_s \approx 170$ kHz. **MC532:** $\mathcal{F}_p \approx 560$, $\nu_p \approx 1.7$ MHz, and $\mathcal{F}_s \approx 13400$, $\nu_s \approx 50$ kHz. The spacer for MC1064 was made of aluminum. The spacer for MC532 was made of invar.

was 1.1% (700 ppm) for p-polarized (s-polarized) light. The cavity had a round-trip length of 42 cm ($\Rightarrow \text{FSR} \approx 714$ MHz) and had a design finesse of approximately 280 (4000) for p(s)-polarized light. The linewidth (FWHM) was 2.5 MHz for p-polarized light and 180 kHz for s-polarized light. A Pound-Drever-Hall locking scheme [5.5] was used to stably control the cavity to be resonant with the carrier frequency of the laser. The error signal was derived by detecting the reflected light with a photodiode (PD_{1064}) and multiplying the output with an electronic local oscillator from the same VCO. This demodulated signal needs to be low-pass filtered in order to extract the DC-term, which constitutes the final error signal. An introduction to the PDH-locking scheme can be found in [5.6]. To actuate the cavity length we used split-feedback to the piezo-driven curved mirror (M3 in Fig. 5.2) and Peltier elements that were attached to the aluminum spacer. This cavity was utilized to reduce phase fluctuations and mode distortion on the transmitted light, thereby providing a local oscillator (LO) beam of maximum quality. Another HWP-PBS combination in front of MC1064 enabled accurate LO power adjustment. The power adjustment was done in front of MC1064 in order to profit from the non-degeneracy of the polarization in a three-mirror cavity. Hence, the polarization of the LO beam was maintained, even though the PBS might have distorted the polarization when different power levels were adjusted.

5.2.2 Pump field preparation

The frequency conversion from 1064 nm to 532 nm was accomplished by means of intra-cavity type I phase-matched second-harmonic generation (SHG). As illustrated in Fig. 5.3, the frequency doubling cavity was designed as a hemilithic standing-wave resonator, defined by a coupling mirror and the backside of the nonlinear medium itself. The nonlinear medium was a 7% magnesium oxide doped lithium niobate (MgO:LiNbO₃) crystal. The doping of 7% results in a phase matching temperature of approximately 60°. The dimensions of the crystal measured 6.5×2×2.5 mm³. The front and rear face of the crystal were equally curved with a radius of curvature (ROC) of 8 mm. The coupling mirror had a radius of curvature of 25 mm, and had a reflectivity of 90% at 1064 nm and a residual reflectivity ($R < 2\%$) at 532 nm. The rear side of the crystal was highly reflective ($R \geq 99.95\%$) for both the fundamental and harmonic wavelengths, whereas the crystal's front side was AR coated ($R < 0.1\%$) for the involved frequencies. The reflectivity of the coupling mirror was chosen to be 90% for 1064 nm resulting in a finesse of ~ 60 . The refractive index of the crystal was $n=2.23$ and the air gap between the crystal and the coupling mirror was 23 mm, resulting in a cavity waist size $w_0 \approx 29\mu\text{m}$. Within an oven design the crystal was embedded between two copper plates with a Peltier element underneath. The Peltier element was used to adjust the temperature of the crystal to the phase-matching temperature. As the temperature sensor a negative temperature coefficient thermistor (NTC) was placed inside a bore hole in the lower copper plate. A home-made temperature controller compared the NTC signal with the set point to provide the necessary feedback current for the Peltier element. Active stabilization of the crystal temperature is important to minimize the phase mismatch and thereby enabling efficient frequency conversion. Approximately 1.7 W at 1064 nm were available in

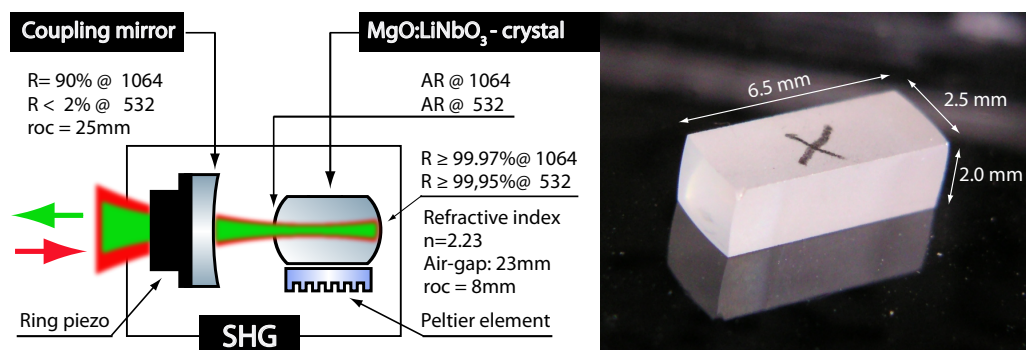


Figure 5.3 — Schematic layout and optical properties of the SHG and photo of a MgO:LiNbO₃-crystal.

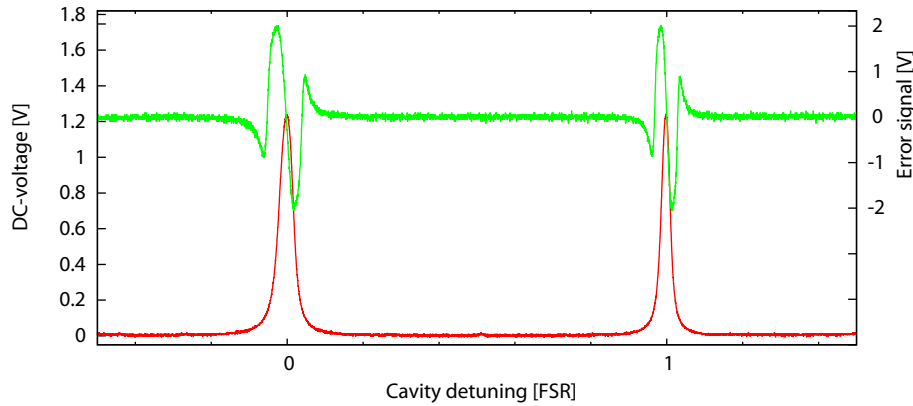


Figure 5.4 — SHG transmission and corresponding error signal. Traces were recorded by scanning the cavity length.

reflection of the partially transmissive mirror (M_p). This field was mode-matched to the TEM_{00} -mode of the SHG cavity. The photo detector (PD_{SHG}) in transmission of the SHG was used to monitor the efficiency of the mode-matching. The same detector was used to demodulate the transmitted light at 122.9 MHz in order to derive the error signal to implement a locking scheme to stabilize the SHG on resonance with the 1064 nm input field. Figure 5.4 shows the DC-signal and the corresponding error signal as recorded with PD_{SHG} when the cavity length was scanned over more than one FSR. Approximately 1 W of second-harmonic radiation at 532 nm was available when the SHG was locked. The 532 nm field was separated from the 1064 nm field on transmission through a dichroic beam splitter (DBS). The pump field passed through an optical diode to prevent the SHG from back reflected light, a combination of half-wave plate and polarizing beam splitter for power adjustment, and was then mode-matched to the TEM_{00} -mode of a mode-cleaning cavity (MC532). The geometric layout of MC532 is equal to the mode-cleaner used for 1064 nm. The optical properties of both ring cavities are summarized in Fig. 5.2. The SHG process also up-converts the phase-modulation that was initially imprinted on the 1064 nm light. Therefore, a PDH error signal for MC532 could be generated by detecting the reflected light with a photo diode (PD_{532}) and demodulating at 122.9 MHz. For this locking loop, feedback was solely applied to the piezo. The reason is the spacer being made of invar, a nickel steel alloy that has an extremely low coefficient of thermal expansion. Therefore, a temperature change would not cause the spacer to change its length. The locking loop was designed such that MC532 could be stably locked with input powers ranging from some milliwatts up to approximately 100 mW.

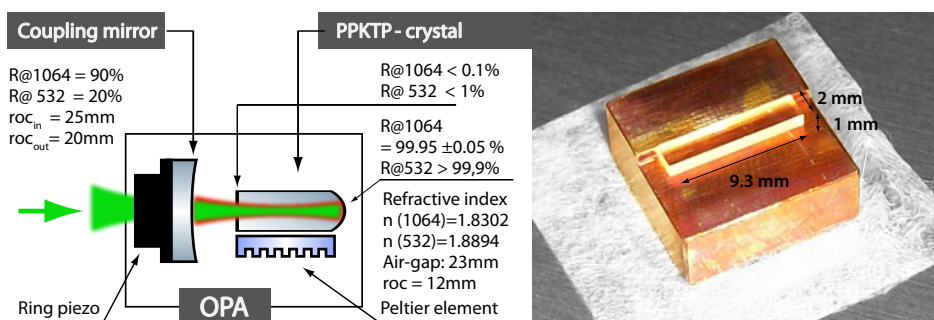


Figure 5.5 — Left: Schematic of the nonlinear cavity and summary of the basic optical properties of the squeezed-light source. Right: photo of a PPKTP crystal on a copper plate. The copper plate is part of an oven that is used to bring the crystal to its phase-matching temperature of approximately 38°.

5.2.3 Generation of squeezed vacuum states

The squeezed vacuum states at 1064 nm were generated by intra-cavity parametric down-conversion. In contrast to the squeezed light source presented in the previous chapter, the squeezing resonator was constructed in a half-monolithic (hemilithic) configuration similar to the SHG design in Fig. 5.3. As the nonlinear medium a crystal made of periodically poled potassium titanyl phosphate (PPKTP) was chosen. The optical properties of the crystal and the basic optical layout of the OPA are summarized in Fig. 5.5. Compared to MgO:LiNbO₃, which was used for the monolithic squeezer, PPKTP has a larger nonlinear coefficient and shows less absorption at 1064. Both facts make PPKTP a very promising material to enable efficient squeezing. In fact, the strongest squeezing reported so far (−12.7 dB) was demonstrated in an experiment [5.7] where we used a monolithic PPKTP squeezer in order to reduce the intra-cavity loss to a minimum.

The realization of the mode-matching of the green pump field into the squeezed light resonator was non-trivial. Since the coupling mirror of the resonator merely had a reflectivity of ~20% for the 532 nm light, almost no reference cavity mode was available. In such cases, the classical gain is often used as an indicator. Let us assume that the cavity is locked and the auxiliary beam is detected with a photo diode in transmission. When the pump field is injected, parts of it will down-convert and interfere with the auxiliary field. As a consequence, when scanning the relative phase (e.g. with a piezo actuated mirror) the voltage on the photo detector will oscillate periodically. Optimizing these interference fringes in terms of the maximum voltage, is equal to maximizing the mode overlap within the resonator. The classical gain is the factor by which the voltage on the photo diode is amplified due to the pump

field with respect to the initial voltage with no pump field. However, here we chose another method to align the pump. When sufficient power is available for the auxiliary beam, the squeezed light source can also be used as an SHG. The generated green light was transmitted through the DBS and was then mode-matched into MC532. The mode spectrum in (reverse) transmission of MC532 was detected with PD_{rev} when the flip-mirror #4 was set to reflect the light. In contrast to the pump field adjustment via the classical gain, this method provided a means to accurately quantify the mode-matching efficiency of the pump. It was determined to be 97%.

5.2.4 Detection of squeezed vacuum states

In order to minimize optical loss, the number of optical components needs to be kept small. One dichroic beamsplitter (DBS) and two HR steering mirrors were used to guide the squeezing into the homodyne detector beamsplitter (HBS). With only two additional HR mirrors, the homodyne detector was set up in a triangular geometry as illustrated in Fig 5.1. In total only three lenses were used in the squeezed light path: L1 (ROC = 50 mm) to focus the divergent beam exiting from the squeezing resonator, and L2 and L3 (both ROC = 25 mm) to focus the beam onto the homodyne photo diodes. Custom-made InGaAs PIN diodes were used for our homodyne detector. They had an active area of 300 μm in diameter and had no protective glass window. The HBS splitting ratio is highly sensitive to the angle and could be precisely adjusted by monitoring the DC-difference signal of the homodyne detector. Assuming identical gain for the two diodes, bringing the DC-difference voltage to zero means that the HBS is adjusted correctly at a 50% splitting ratio. Or vice versa: possible (small) differences in the gain of the two photo diodes can be balanced by the appropriate HBS tilt. The smaller the difference voltage, the better is the common mode rejection (CMR) of the homodyne detector circuit. A large CMR is desirable because this leads to a strong cancellation of possible technical noise present in the local oscillator field. If all the correlated technical noise vanishes, the LO is quantum-noise limited at all frequencies. In order to quantify the CMR one needs to compute the sum of the voltages measured individually on each diode when the other is blocked and compare it to the difference voltage. This could only be done at a LO power that did not saturate the single detectors. Such a measurement typically resulted in values $\sim 8\text{ V}$ for the sum and $\sim 1\text{ mV}$ for the difference, such that

$$\text{CMR} = 10 \log_{10} \left[\frac{1}{8000} \right] \approx -40 \text{ dB} . \quad (5.1)$$

The performance of the homodyne detector was tested by measuring the output noise for different powers of the LO. An increase or decrease of the power by a factor of

2 resulted in a 3 dB increase or decrease of the measured noise level, which verified the homodyne detector's linearity and indicated that LO was quantum noise limited. In squeezing experiments the homodyne visibility (VIS), that is the interference contrast between the local oscillator and the squeezed (signal) field on the 50/50 beam splitter, is crucial because any mode mismatch quadratically translates into optical loss. To adjust the homodyne visibility a bright beam was needed that resembled the squeezed vacuum output of the OPA and could be interfered with the LO. To this end the auxiliary beam (see Fig. 5.1) was matched to the TEM_{00} mode through the HR-coated rear surface of the OPA. When flip-mirror #3 was unflipped, a photo diode (PD_{OPA}) detected the reflected light and by demodulating at 122.9 MHz, an appropriate PDH-error signal was produced to lock the OPA length. The transmitted light propagated congruent with the mode to be squeezed. For high precision alignment of the mode-overlap we used the diagnostic mode cleaner MC_D (another ring-cavity similar to the MC-cavities) as a reference. First, the auxiliary beam was guided via flip-mirror #2 towards MC_D , whose transmission spectrum was monitored with PD_{MCD} . The lens (L1) in the squeezing path was positioned so that the resulting focus exactly met the waist size of MC_D . The mode-matching was done with the steering mirrors M1 and M2. A mode-matching of $> 99.7\%$ was obtained. Second, using the steering mirrors M3 and M4, the local oscillator beam was aligned to match the mode defined by MC_D with almost equal efficiency. Flip-mirror #1 guided the light on a monitoring photo detector PD_{vis} that was used to measure the interference fringes when the relative phase between LO and auxiliary beam was scanned. By carefully adjusting the power of LO and auxiliary beam to be equal, a visibility of as high as $99.4 \pm 0.1\%$ was achieved.

5.3 Observation of 12.3 dB squeezing at 1064 nm

During data taking the auxiliary field was blocked. This ensured true vacuum squeezing and avoided the degradation of the squeezing level due to excess noise from the auxiliary beam. To keep the squeezed light source on resonance, the cavity length was tuned manually. This was accomplished by adjusting the offset of the HV-amplifier connected to the piezo that moved the coupling mirror. As an indicator for the squeezed light source being on resonance, the signal on the spectrum analyzer was used. The detected quadrature is continuously rotated from squeezing to anti-squeezing when scanning the phase of the green pump field by moving the phase shifter (mirror M_θ) in front of MC532. The cavity could be precisely adjusted

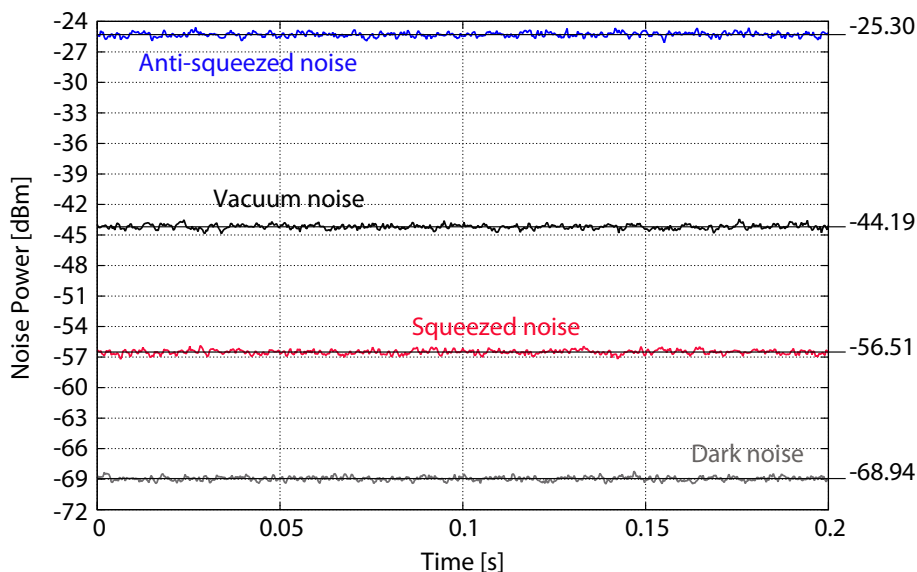


Figure 5.6 — 1064 nm-squeezed light from the hemilithic squeezed light source. The squeezer was pumped with 70 mW at 532 nm. The LO power was 18 mW. All traces were recorded in zero-span mode at 5 MHz sideband frequency and with RBW = 300 kHz and VBW = 300 Hz. Each trace was fitted for its means value by a simple linear regression. The obtained mean values are given by the solid lines with their corresponding values specified on the right. The squeezing was 12.32 ± 0.25 dB below the vacuum noise; the anti-squeezing was 18.89 ± 0.25 dB above the vacuum noise. The detector dark noise was almost 25 dB below the vacuum level and was not subtracted from the data.

on resonance by maximizing the anti-squeezing. To optimize the gain, the crystal temperature was also accurately tuned to its optimum.

At a sideband frequency of 5 MHz, a pump power of 70 mW yielded maximum squeezing. The corresponding data as collected by the spectrum analyzer are depicted in Fig. 5.6. The traces were recorded as zero-span measurements with a resolution bandwidth (RBW) of 300 kHz and video bandwidth (VBW) of 300 Hz. The vacuum noise level was measured when only the LO input to the HBS was opened. The corresponding LO power was ~ 18 mW. The anti-squeezed vacuum noise and the squeezed vacuum noise were measured by injecting the output of the squeezed light into the signal port. Again, the phase of the pump was used to control the quadrature angle. The detector dark noise was measured when both, LO and signal input were blocked. It was approximately 25 dB below the vacuum noise and was not subtracted from the data. Hence, the resulting squeezing value of 12.3 dB is a direct observation. The anti-squeezing was 18.9 dB above vacuum noise. In order to get more detailed

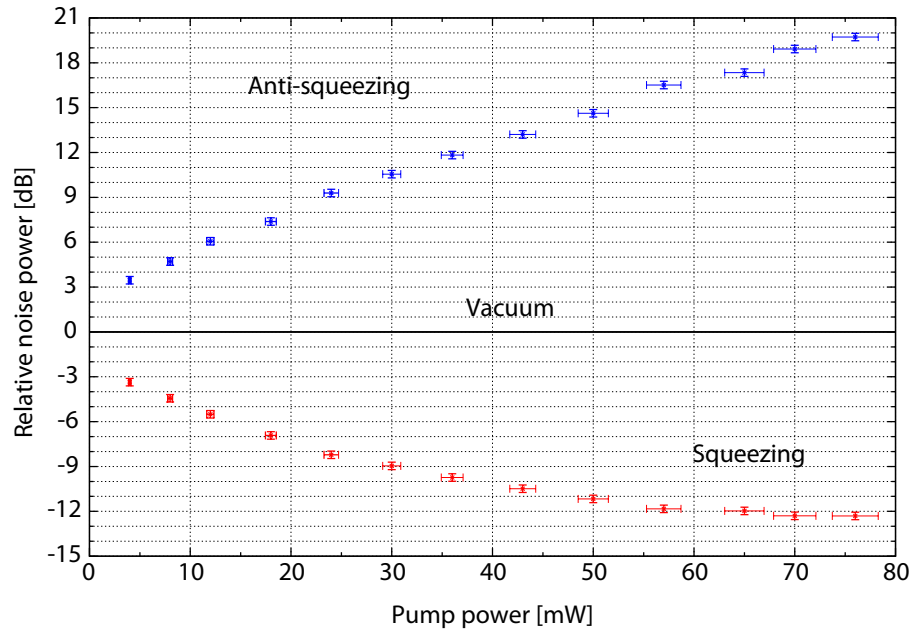


Figure 5.7 — Anti-squeezing and squeezing as a function of the pump power. The measurement frequency was 5 MHz. All points were obtained from an average of two single traces of the vacuum noise, the squeezing and the anti-squeezing measured in zero-span mode with $\text{RBW} = 300 \text{ kHz}$ and $\text{VBW} = 300 \text{ Hz}$. Subsequently, squeezing and anti-squeezing were normalized to the vacuum level. The detector dark noise is still included in the data. Hence all values represent direct observations. The uncertainty in the pump power originated from the 3% uncertainty of the power meter; the vertical error-bars correspond to the standard deviation ($\pm 0.25 \text{ dB}$) of the linear regression.

information on the performance of the squeezer, such zero-span measurements were conducted for various pump power values. Measured in transmission of MC532, these ranged from 4 mW up to 76 mW. The results are plotted in Fig. 5.7; the numeric values as they were used in the plot are summarized in Table 5.1. Each data point is an average of two individually measured traces, hence the value of maximum squeezing is slightly less compared to the single trace above.

5.4 Experimental data vs. theory

The model introduced in Sec. 3.4 can be used to fit measurement data for the total detection efficiency and the phase noise. This model does not include a term that

Pump power [mW]	Anti-sqz [dB]	Sqz [dB]	σ_{fit} [dB]
4 ± 0.12	3.46	-3.36	0.25
8 ± 0.24	4.71	-4.44	0.25
12 ± 0.36	6.06	-5.51	0.25
18 ± 0.54	7.38	-6.92	0.25
24 ± 0.72	9.29	-8.22	0.25
30 ± 0.90	10.55	-8.96	0.25
36 ± 1.08	11.83	-9.74	0.25
43 ± 1.29	13.21	-10.49	0.25
50 ± 1.50	14.62	-11.17	0.25
57 ± 1.71	16.51	-11.83	0.25
65 ± 1.95	17.34	-11.97	0.25
70 ± 2.10	18.92	-12.30	0.25
76 ± 2.28	19.72	-12.31	0.25

Table 5.1 — Measurement data: Anti-squeezing and squeezing vs. pump power. The error in the pump power is $\pm 3\%$ due to the uncertainty of the power meter. The error of ± 0.25 dB in the anti-squeezing and squeezing values is the standard deviation σ_{fit} as given by the linear fit.

resembles the contribution of electronic detector noise. Therefore, the measurement data need to be corrected by subtraction of the dark noise. Moreover, the pump power needs to be normalized with respect to the efficiency of the mode matching between the pump field and the TEM₀₀-mode of the squeezing resonator. This will effect the resulting threshold power. In order to correct the data, first the dark noise was subtracted from every trace (anti-squeezing, vacuum, and squeezing) before normalizing all traces to the (new) vacuum. Second, the pump power was scaled by the 97% mode matching efficiency. The corrected data are summarized in Table 5.2.

5.4.1 Direct measurement of the linewidth and free spectral range

The frequency dependence of the model is given by the ratio of the measurement frequency and the cavity's half-linewidth. The linewidth of the squeezing resonator is usually inferred from the transmission of the coupling mirror, the intra-cavity loss, the transmission of the HR-mirror and the optical length of the cavity. All of these values are difficult to assess. Therefore, a second laser, referred to as the *probe laser*, was used to directly determine the linewidth and the free spectral range (FSR) of the squeezed-light source. The modification that had to be realized in order to conduct the measurement are shown in Fig. 5.8. The probe laser was overlapped with the auxiliary

Pump power [mW]	Anti-sqz [dB]	Sqz [dB]	σ_{fit} [dB]
3.9	3.46	-3.37	0.25
7.8	4.72	-4.47	0.25
11.6	6.07	-5.55	0.25
17.5	7.39	-6.98	0.25
23.3	9.30	-8.30	0.25
29.1	10.56	-9.07	0.25
34.9	11.84	-9.87	0.25
41.7	13.22	-10.64	0.25
48.5	14.64	-11.35	0.25
55.3	16.53	-12.04	0.25
63.1	17.36	-12.19	0.25
67.9	18.93	-12.54	0.25
73.7	19.74	-12.55	0.25

Table 5.2 — Corrected measurement data: Anti-squeezing and squeezing vs. pump power. Here, electronic detector dark noise was subtracted from the anti-squeezing and the squeezing values. The pump power mean values were corrected for the mode matching efficiency of 97%. The error in the pump power still is $\pm 3\%$.

beam on a partially transmissive mirror (M1) and was hence also mode-matched to the fundamental mode of the cavity. A second partially transmissive mirror (M2) was used to split the two beams in one part that bypassed the cavity and one part that was transmitted through the cavity. By means of the flip-mirrors, both beams (bypassed and transmitted) could subsequently be detected with the same photo detector (PD_{GHz}). This detector had a bandwidth >4 GHz and was connected to a spectrum analyzer. As before, the length of the cavity was stabilized by means of the auxiliary beam. To measure the linewidth the transmitted light was detected. The cavity transfer function was then readily obtained by operating the spectrum analyzer in ‘max-hold’ mode and scanning the probe laser frequency. The frequency adjustment was accomplished by actuating on the laser’s built-in piezo which changed the output frequency by 1 MHz per applied volt. A typical result is displayed in Fig. 5.9. The peaks correspond to the beat signal between the carrier field and the probe laser. By changing the probe laser detuning, a frequency range from 2 MHz up to 110 MHz could be mapped out. Trace (a) is the spectrum analyzer signal as recorded in transmission, and thus is the amplitude transfer function of the cavity. The line width can then be obtained by fitting a pole of the form $1/(1 + i(x/f_c))$ to the data, where f_c is the cutoff frequency which is equal to the half linewidth of the cavity. The spectral response of

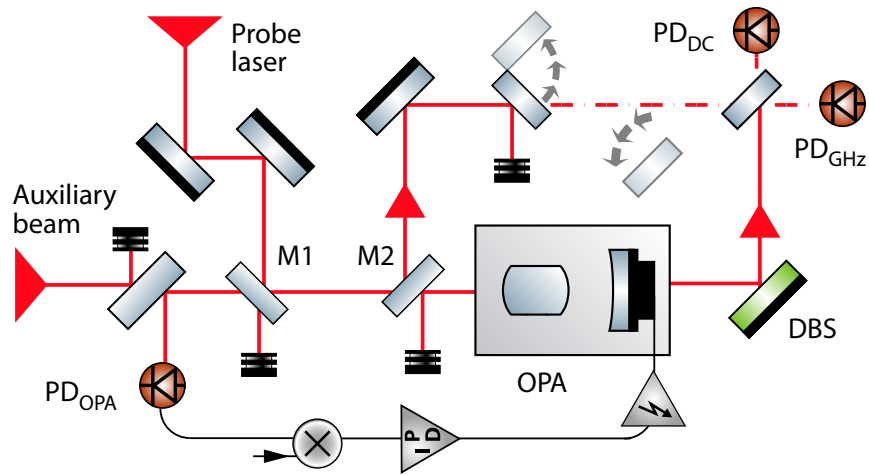


Figure 5.8 — Schematic of the experimental setup for direct measurement of the cavity linewidth. To overlap the probe laser with the auxiliary (carrier) beam, the mirror M1 was incorporated.

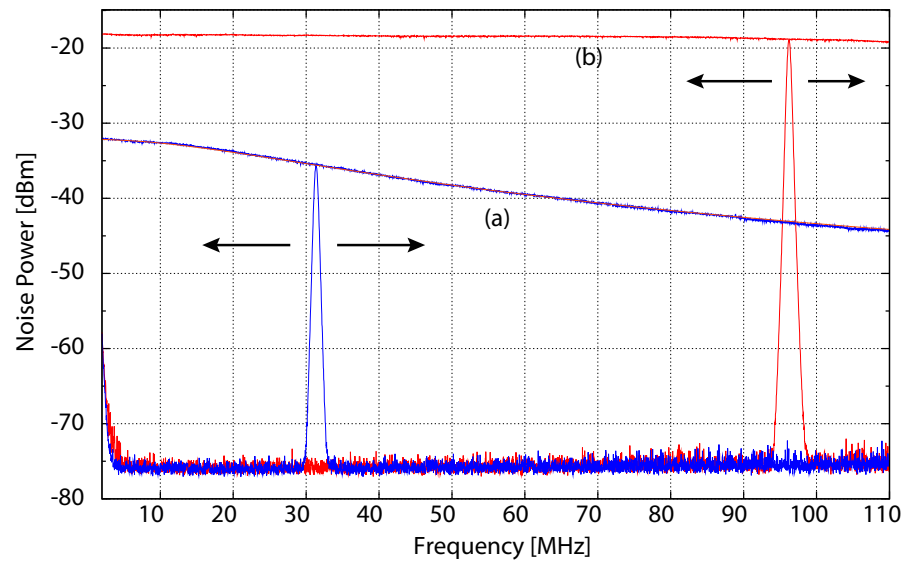


Figure 5.9 — Measurement of the cavity linewidth. The peaks are the beat signal between the probe laser and the main laser. Trace (a) is the transfer function detected in transmission of the cavity. Trace (b) was recorded when the cavity was bypassed.

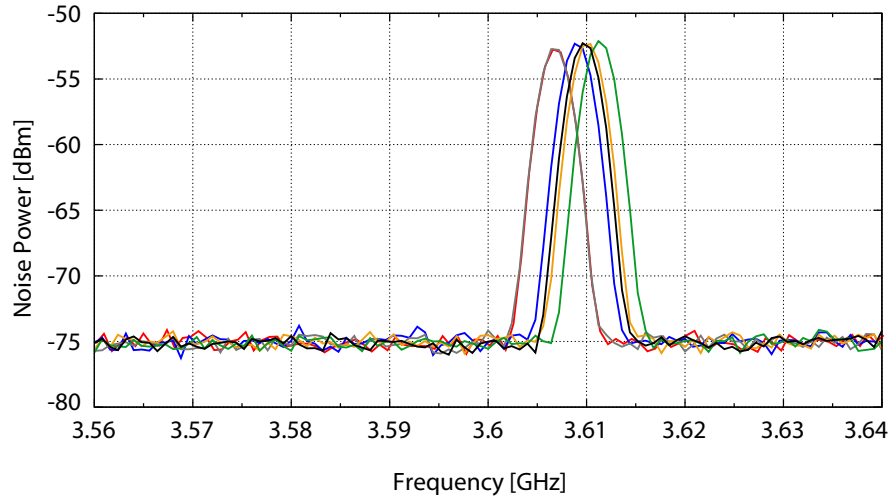


Figure 5.10 — Measurement of the free spectral range of the squeezing cavity. The peaks are the beat signal between the probe laser and the main laser. The detuning corresponding to one FSR was determined to be 3.607 GHz, 3.6098 GHz, 3.6102 GHz, 3.609 GHz, and 3.6115 GHz.

the bypassed signal, that is the pure beat signal, is shown as trace (b). As it is flat up to a frequency of 80 MHz, this frequency was chosen as the maximal frequency for the fit. A total of nine measurements were made. The resulting half-linewidth was calculated to be $\nu/2 = 28.996 \pm 0.534$ MHz. Similarly, the FSR of the squeezing resonator could be determined. To this end, the cavity length was periodically scanned and the transmitted intensity was monitored with the second photo diode (PD_{DC}) resulting in an oscilloscope image similar to Fig. 5.4. The beat frequency could now be controlled to be exactly zero by observing the transmission peak of the probe laser and the spectrum analyzer signal simultaneously. From degeneracy, the probe laser was then shifted until the transmission peak appeared exactly at one FSR on the oscilloscope. At that particular moment the spectrum analyzer signal was recorded. 31 measurements of that kind were conducted, yielding a value for the free spectral range of $\text{FSR} = 3.6104 \pm 0.0044$ GHz. One set of six such measurements is shown in Fig. 5.10. This leads to a cavity finesse of $\mathcal{F} = \text{FSR}/\nu \approx 62.3 \pm 1.2$.

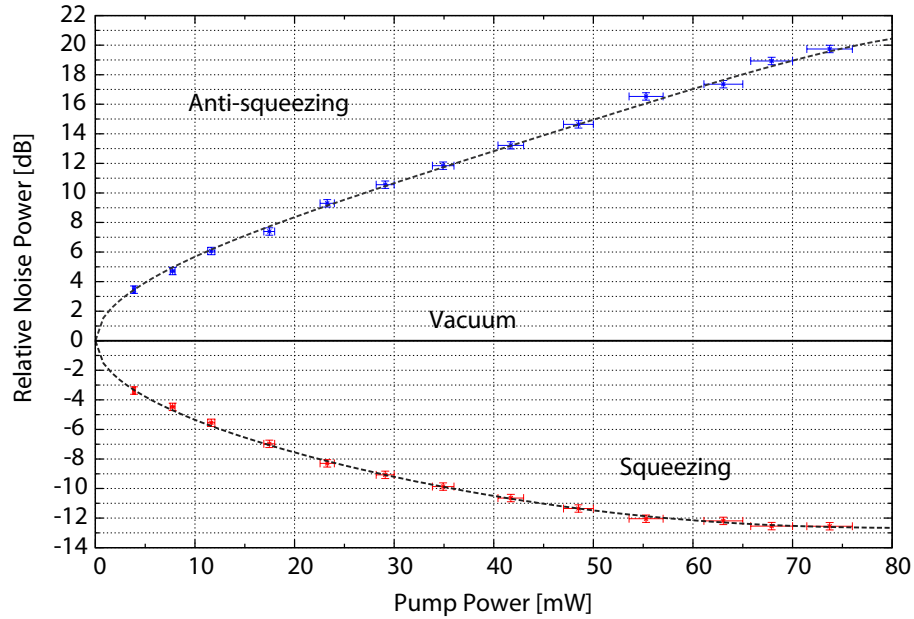


Figure 5.11 — Squeezing and anti-squeezing as a function of the pump power. The corrected data were fitted for the total detection efficiency η , the threshold power P_{th} and the phase noise θ_{fluc} . The best fit was obtained with $\eta = 0.96$, $P_{\text{th}} = 89.2 \text{ mW}$, and $\theta_{\text{fluc}} = 0.4^\circ$.

5.4.2 Deriving the detection efficiency via the level of squeezing and anti-squeezing

The obtained value of 29 MHz for the linewidth can now be used in the model, Eqs. (3.62)–(3.65), by setting $\nu/2 = 29 \text{ MHz}$. Figure 5.11 illustrates the result from fitting the data as given in table 5.2 for the total detection efficiency, the phase noise, and the threshold power. Dashed lines are the anti-squeezing and squeezing values as predicted by the model when inserting the resulting parameters of the fit: $\eta = 0.96$, $P_{\text{th}} = 89.2 \text{ mW}$, and $\theta_{\text{fluc}} = 0.4^\circ$. As the result, we find the total detection efficiency of our system to be 96%.

5.4.3 Loss analysis

As mentioned above, the total detection efficiency is calculated as the product of escape efficiency η_{esc} , propagation efficiency η_{prop} , homodyne efficiency η_{homo} , and the quantum efficiency η_{qe} . A detailed analysis was carried out to determine each of the efficiencies separately.

Homodyne efficiency

The homodyne efficiency, which is the visibility squared, can easily be determined with high accuracy. As already stated earlier, the visibility was measured to be $VIS = 99.4 \pm 0.1\%$. This translates into a homodyne efficiency $\eta_{\text{homo}} = VIS^2 = 98.8 \pm 0.2$.

Propagation efficiency

To investigate the propagation loss, the transmitting components were investigated in more detail. In an independent measurement, the residual reflection due to each of the lenses was determined to be smaller than 0.05%. Only three lenses were used, one to refocus the beam exiting the squeezed-light source; and one in front of each of the homodyne detector photo diodes. Including the possible absorption in the fused-silica lenses, the total loss due to a single lens is estimated to be smaller 0.1%. The residual reflection at the AR coating of the 50/50 beamsplitter was measured to be smaller than 0.02%. A total of four HR steering mirrors and one dichroic beamsplitter was used in the squeezed-light path. All of those mirrors were super-polished and had a reflectivity greater 99.995%. The last item to consider is the the coupling mirror of squeezing resonator. It was 6 mm thick half-inch substrate made of generic fused-silica. The AR coating and the absorption are estimated to contribute another 0.1%–0.2% of optical loss. The product of all these efficiencies yields a minimum propagation efficiency of $\eta_{\text{prop}} \approx 99.6\%$.

Escape efficiency

The escape efficiency, as given by Eq. (3.48), is determined by the reflection of the coupling mirror and the intra-cavity round-trip loss. The round-trip loss includes the residual reflection of the crystal's AR coating, the loss due to absorption and scattering, and the transmission through the HR coating on the crystal's rear side. The finesse of the cavity was determined to $\mathcal{F} = FSR/\nu \approx 62.3 \pm 1.2$. From this one can infer an effective reflectivity, which comprises all losses, of $90.6 \pm 0.2\%$. The HR was specified to $99.95 \pm 0.05\%$ by the manufacturer. By using the HR side as the coupling mirror and detecting the reflection pattern when scanning the cavity length, the reflectivity was determined to be 99.96% by comparison with a *Finesse*-simulation [5.9]. In [5.10] the absorption within a PPKTP crystal similar to the one used here was determined to be $1.2 \times 10^{-3} \text{ m}^{-1}$. Thus, the intra-cavity loss is governed by the quality of the AR coating. Assuming the coating to be perfect, the coupling mirror transmission would be $9.36 \pm 0.2\%$, which yields a maximum escape efficiency of $\eta_{\text{esc,max}} \approx 99.6$. However, if the AR coating has a residual reflectivity of 0.05%, this adds another 0.1% to the roundtrip loss and the escape efficiency decreases to $\eta_{\text{esc}} \approx 98.5$.

5.4.4 Quantum efficiency of the photo diodes

It is now possible to obtain the quantum efficiency of the photo detectors by dividing the total detection efficiency $\eta = 96\%$ by the product of the efficiencies obtained above. First, an absolute lower limit for the quantum efficiency can be derived by setting the escape efficiency equal to the maximum escape efficiency. This yields $\eta_{qe,min} = \eta / (\eta_{homo}\eta_{prop}\eta_{esc,max}) = 0.98 \pm 0.002$. Using the escape efficiency of 98.5%, the obtained lower limit for the quantum efficiency is $\eta_{qe} = 0.99 \pm 0.002$.

5.5 Conclusion

From the observation of squeezing levels of up to 12.3 dB, a total detection efficiency of 96% was determined. In order to derive a value for the quantum efficiency of the photo diodes used in the homodyne detector, the possible sources of loss were analyzed in detail. It was found that 1.6% can be attributed to the imperfect homodyne visibility and the propagation loss. The biggest uncertainty is given by the loss due to the escape efficiency of the squeezed light source. Assuming the least possible amount of loss, yielded the lower limit of $98 \pm 0.2\%$ for the quantum efficiency. A residual reflection at the AR coating of 0.05% was assumed to illustrate the effect of additional intra-cavity loss. The new resulting lower limit for the quantum efficiency was $99 \pm 0.2\%$. To infer the escape efficiency more precisely it is planned to set up an experiment which provides more knowledge on the value of round-trip loss. One means to realize this, is to incorporate the crystal into a high-finesse cavity. In this case, the impedance matching is much more sensitive to the intra-cavity losses and deviations from the nominal values will be more prominent.

References

- [5.1] Product data sheet, available at <http://www.ophiropt.com/laser-measurement-instruments/laser-power-energy-meters/products/power-sensors/photodiode-sensors>
- [5.2] Product data sheets, available at http://www.thorlabs.de/NewGroupPage9.cfm?ObjectGroup_ID=3337
- [5.3] Product data sheet, http://www.lasercomponents.com/fileadmin/user_upload/home/Datasheets/gentec/calibration.pdf

- [5.4] B. Wilke, N. Uehara, E. K. Gustafson, R. L. Byer, P. J. King, S. U. Seel, and R. L. Savage, Jr. "Spatial and temporal filtering of a 10-W Nd:YAG laser with a Fabry-Perot ring-cavity premode cleaner," *Optics Letters* **23**, 1704 (1998).
- [5.5] R. W. P. Drever, J. L. Hall, F. V. Kowalski, J. Hough, G. M. Ford, A. J. Munley, and H. Ward, "Laser phase and frequency stabilization using an optical resonator," *Appl. Phys. B* **31**, 97–105 (1983).
- [5.6] E. D. Black, "An introduction to pound-drever-hall laser frequency stabilization," *Am. J. Phys.* **69**, 79–87 (2001).
- [5.7] T. Eberle, S. Steinlechner, J. Bauchrowitz, V. Händchen, H. Vahlbruch, M. Mehmet, H. Müller-Ebhardt, and R. Schnabel, "Quantum Enhancement of the Zero-Area Sagnac Interferometer Topology for Gravitational Wave Detection," *Phys. Rev. Lett.* **104**, 251102 (2010).
- [5.8] H. Vahlbruch, *Squeezed Light for Gravitational Wave Astronomy*, PhD thesis, Leibniz Universität Hannover, 2008.
- [5.9] An interferometer simulation tool. <http://www.gwoptics.org/finesse/>
- [5.10] T. Meier, *High-Power CW Green Lasers for Optical Metrology and Their Joint Benefit in Particle Physics Experiments*, PhD thesis, Leibniz Universität Hannover, 2011.

Squeezed light at 1550 nm

We report on the generation of cw squeezed vacuum states of light at the telecommunication wavelength of 1550 nm. The squeezed vacuum states were produced by type I optical parametric amplification in a standing-wave cavity built around a periodically poled potassium titanyl phosphate crystal. A nonclassical noise reduction of 5.3 dB below the shot noise was observed by means of balanced homodyne detection.

Originally published as M. Mehmet et al. *Opt. Lett.* **34**, 1060–1062 (2009).

6.1 Introduction

Squeezed states of light were proposed to improve the sensitivity of laser interferometers for the detection of gravitational waves (GWs) [6.1] and to establish quantum communication channels [6.2], e.g., for quantum key distribution [6.3, 6.4]. For any application of squeezed states of light, a low decoherence level is required, i.e., optical loss and thermally driven noise sources need to be minimized. In this respect the laser wavelength of 1550 nm has emerged as a very interesting topic. First, at this wavelength conventional silica-based telecommunication glass fibers show low optical loss and can be used for the transmission of squeezed states. Losses of as low as 0.2 dB/km were already measured in the late 1970s [6.5], and ultralow loss (ULL) fibers with an attenuation of 0.17–0.18 dB/km are commercially available today [6.6]. Second, at this wavelength, crystalline silicon constitutes an excellent test mass material for interferometric applications with low optical loss and high mechanical quality [6.7]. GW detectors require the generation of squeezed states in a single spatiotemporal mode of cw light, whereas quantum channels can also be established in the pulsed

laser regime. In previous years squeezed states at wavelengths beyond $1.5 \mu\text{m}$ were generated mainly in the latter regime, and various degrees of squeezing have been observed; for example 6.8 dB at $1.5 \mu\text{m}$ [6.8], 3.2 dB at $1.535 \mu\text{m}$ [6.9], and 1.7 dB at $1.55 \mu\text{m}$ [6.10]. Recently, 1560 nm cw-squeezed vacuum states showing a nonclassical noise suppression of 2.4 dB were generated by an optical parametric oscillator based on periodically poled LiNbO_3 [6.11].

Here, we report on the generation of cw squeezed vacuum states at a wavelength of 1550 nm based on periodically poled potassium titanyl phosphate (PPKTP). Squeezing of 5.3 dB was observed by balanced homodyne detection. The visibility of the mode matching between the squeezed field and a spatially filtered local oscillator beam was measured to be 99%, thereby proving a high spatial mode quality of the squeezed states.

6.2 Experimental setup

The light source in our setup, as schematically depicted in Fig. 6.1, was a high-power erbium microfiber laser providing about 1.6 W of cw radiation at 1550 nm. The laser beam was first sent through a ring mode cleaner (MC) cavity with a finesse of 350 and a linewidth of 1.2 MHz for p -polarized light, thus reducing mode distortions of the laser's TEM_{00} spatial mode profile as well as its phase and amplitude fluctuations at frequencies above the MC linewidth. Approximately 10 mW of the transmitted light served as a local oscillator (LO) for balanced homodyne detection, while the remaining power of about one 1 W was used for second-harmonic generation (SHG) to provide the frequency-doubled pump field for the optical parametric amplification (OPA). Both SHG and OPA were realized as single-ended standing-wave cavities formed by two mirrors and the nonlinear crystal in between. In both cavities we employed a PPKTP crystal of dimension $10 \text{ mm} \times 2 \text{ mm} \times 1 \text{ mm}$ with flat, antireflection (AR) coated front and end faces. Inside a polyoxymethylene (POM) housing, each crystal is embedded in a copper fixture mounted on a Peltier element. Together with an integrated thermistor this enabled us to actively fine tune the crystal temperature for efficient nonlinear coupling around 55°C . A highly reflective (HR) mirror with a power reflectivity $r > 99.98\%$ for both the fundamental and second harmonic field faces one AR side of the crystal, and a piezodriven outcoupling mirror was mounted on the opposite side. The OPA outcoupling mirror had 90% and 20% power reflectivity for 1550 and 775 nm, respectively. For the SHG we also used 90% reflectivity for the fundamental but only a marginal reflectivity for the second harmonic. The mirrors

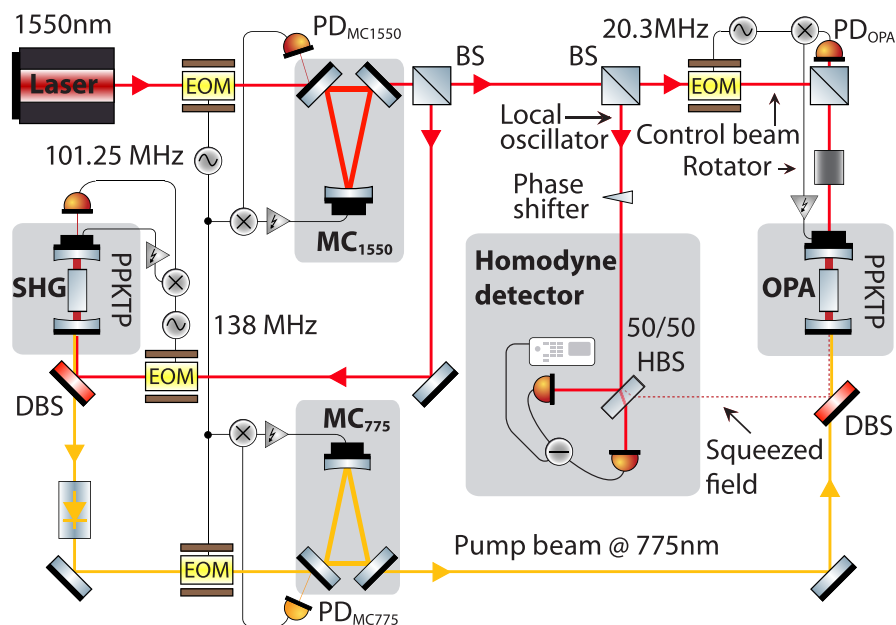


Figure 6.1 — Schematic of the setup. After being sent through a MC cavity, one part of the light is used as a control beam for the OPA and the local oscillator for balanced homodyne detection. The other part is frequency doubled in a SHG cavity to provide the 775 nm field to pump the OPA. The squeezed field leaves the OPA in the counter direction to the pump and is measured with the homodyne detector. PBS, polarizing beam splitter; DBS, dichroic beam splitter; HBS, homodyne beam splitter; MC, mode cleaner cavity; PD, photo diode; EOM, electro-optical modulator.

and the ring-piezo were mounted inside aluminum blocks that were rigidly attached to the POM housing. Considering the refractive index of $n=1.816$ for PPKTP at 1550 nm and the spacing of 20 mm between crystal end faces and mirrors, the cavity waist size w_0 , free spectral range FSR, and linewidth (FWHM) were calculated to be $w_0=60 \mu\text{m}$, $\text{FSR}=2.6 \text{ GHz}$, and $\text{FWHM}=43 \text{ MHz}$, respectively. When the SHG cavity was locked on resonance it produced up to 800 mW at 775 nm, which was separated from the fundamental by a dichroic beam splitter (DBS). The harmonic beam passed a combination of a half-wave plate and a polarizing beam splitter for pump power adjustment, a Faraday isolator to prevent the SHG from retroreflected light, and an electro-optical modulator (EOM), and was mode matched to the TEM_{00} mode of another MC cavity (MC_{775}) with characteristics equal to those of MC_{1550} . The transmitted beam was then carefully aligned to match the OPA-cavity TEM_{00} mode. The length control of the cavities in our setup was accomplished by means

of a modulation-demodulation (Pound-Drever-Hall) scheme utilizing custom-made EOMs and matched photodetectors. Details on the particular implementation can be found in Fig. 6.1. The squeezed states left the OPA in the counter direction to the second-harmonic pump, where another DBS separated the two of them. The measurement of field quadrature variances was accomplished by means of balanced homodyne detection, for which the squeezed field was subsequently made to interfere with the LO on a 50/50-beam splitter. A piezoactuated steering mirror was employed to shift the LO phase relative to the squeezed field. To adjust the visibility we injected a control beam through the HR back side of the OPA. This control beam was matched to the OPA TEM₀₀ mode. The light that was transmitted propagated congruent to the mode to be squeezed and, by locking the OPA cavity length, could be used to overlap with the LO on the homodyne beam splitter (HBS). We reached a fringe visibility of 99.0%. The two outputs of the 50/50-beam splitter were each focused down and detected by a pair of Epitaxx ETX-500 photodiodes. The difference current was fed to a spectrum analyzer.

6.3 Observation of 5.3 dB squeezing

To verify our detector's linearity we took measurements of the vacuum noise power against the incident LO power at a sideband frequency of 5 MHz, as depicted in Fig. 6.2. Changing the LO power by a factor of two entailed a 3 dB shift of the corresponding noise trace, showing that the detector was quantum noise limited and operated linearly in the measurement regime.

We found the optimum pump power for our OPA to be 300 mW, yielding a noise reduction of 5.3 dB in the squeezed quadrature. This entailed an increase of 9.8 dB in the antisqueezed quadrature. To switch between the two, a piezoactuated mirror was used to phase shift the LO with respect to the squeezed field. The measured noise curves are depicted in Fig. 6.3. Trace (a) is the measured vacuum noise when the signal port of the HBS is blocked. The associated power of the incident LO was approximately 4 mW. Upon opening the signal port and injecting the squeezed field of the resonant OPA, trace (d) was recorded by linearly sweeping the LO phase, thereby changing the measured quadrature from antisqueezed to squeezed values. By holding the homodyne angle fixed, continuous traces of the squeezing (b) and antisqueezing (c) were recorded. All traces were recorded at a sideband frequency of 5 MHz and are, apart from (d), averaged twice. The contribution of electronic dark noise of our detector was negligible (18 dB below the shot noise) and was not subtracted from the

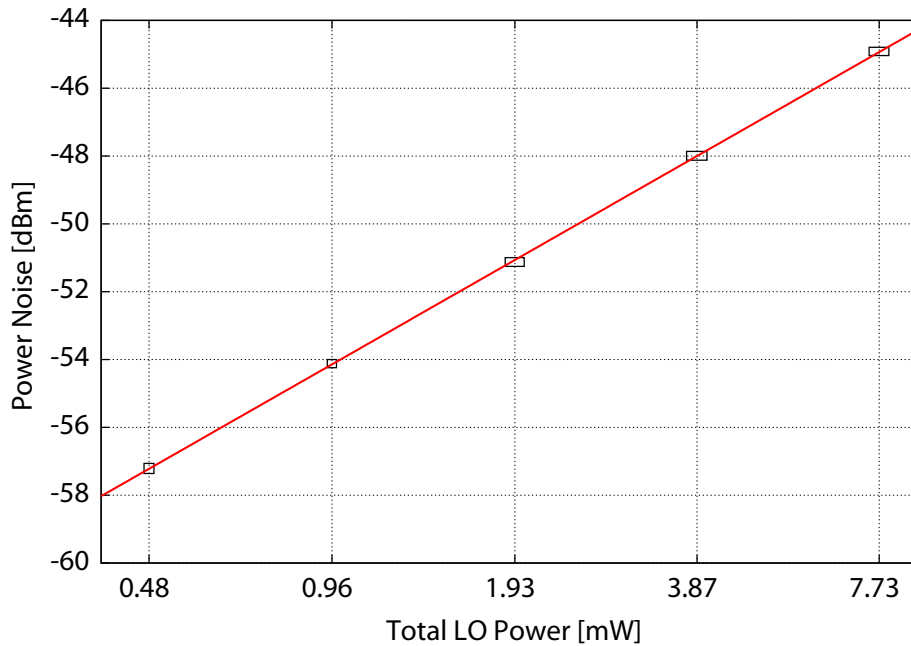


Figure 6.2 — Noise power levels of the homodyne detector were measured at different LO powers at a center frequency of 5 MHz with the signal port blocked. Box sizes indicate the standard deviation of the fit and an estimated $\pm 5\%$ uncertainty of the power meter used. The graph shows that our homodyne detector was quantum noise limited and operated linearly within our measurement regime.

measured data.

6.4 Conclusion

The observed squeezed noise power was 5.3 dB below shot noise; however, the observed antisqueezing was about 10 dB above shot noise, revealing an uncertainty product of about a factor of 3 above the minimum uncertainty. With an increased pump power we observed further increased antisqueezing, but a constant squeezing level. Following the argumentation in [6.12] this observation implies that our measurement was not limited by phase noise [6.13, 6.14] but by optical losses. With 0.25% residual reflectance of our crystal AR coatings and 0.1 %/cm absorption loss within the crystal we estimate the escape efficiency of the OPA cavity to be 90%. Together

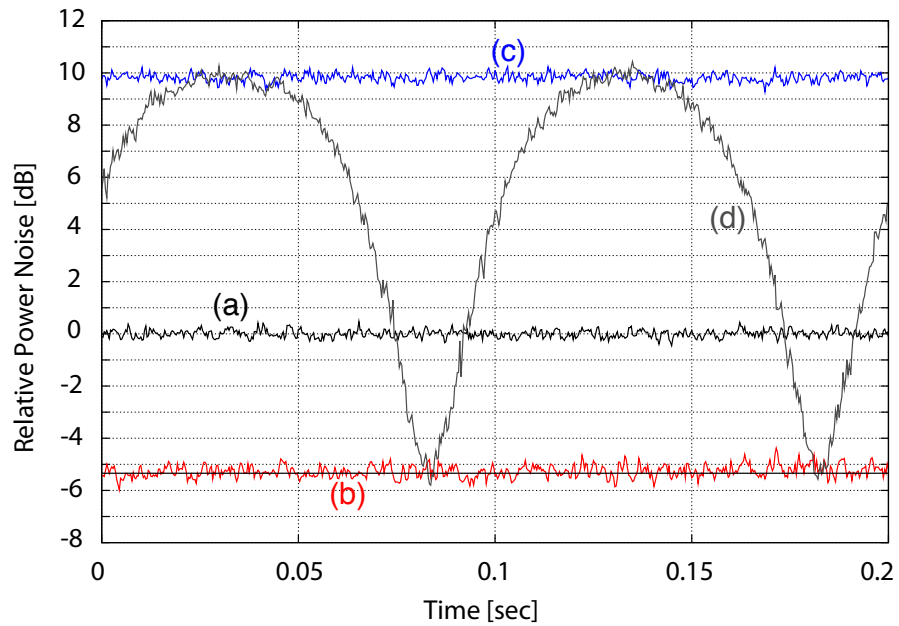


Figure 6.3 — Noise powers of the squeezed light emitted by the OPA at a sideband frequency of 5 MHz normalized to the shot-noise level [trace (a)]. All traces were recorded with a resolution bandwidth of 300 kHz and a video bandwidth of 300 Hz. Squeezing (b) and antisqueezing (c) curves were averaged twice. Curve (d) was recorded by linearly sweeping the LO phase, which continuously rotated the measured quadrature from antisqueezing to squeezing.

with a propagation loss of approximately 3%, we estimate the quantum efficiency of our photodetectors to be $90\% \pm 4\%$. This yields a total of $23\% \pm 4\%$ optical loss that degrades the squeezing once it is produced.

We note that PPKTP has already been successfully applied for the generation of squeezed and entangled states at wavelengths between 532 and 1064 nm [6.14–6.18] with the maximum squeezing strength of 9 dB observed at 860 nm in [6.14]. The strongest squeezing to date was reported in [6.12], where a MgO:LiNbO₃ crystal enabled the observation of a noise reduction of 10 dB below shot noise at 1064 nm. However, at 1550 nm the phase-matching condition of this material is uncomfortably high, and temperature gradients would significantly complicate the stable operation of a squeezed-light source. This makes PPKTP the preferable material for the generation of squeezed light at 1550 nm, and we expect that, by utilizing better photodiodes and an OPA optimized for better escape efficiency, squeezing levels of 10 dB or even higher could be observed in future.

In conclusion, we have demonstrated strong squeezing at the telecommunication

wavelength of 1550 nm. Our experiment proved that PPKTP is an effective material for the generation of squeezed states at this wavelength. The spatiotemporal mode of the squeezed field had a high purity, ensuring the compatibility with quantum memories and quantum repeaters. By implementing a control scheme according to [6.19] squeezing in the detection band of current GW detectors can be realized. These detectors are operated at 1064 nm [6.17]; however, future detector designs might consider silicon as test mass material and the laser wavelength of 1550 nm to reduce the thermal noise floor.

The authors acknowledge the German Research Foundation and the Centre for Quantum Engineering and Space-Time Research QUEST for financial support.

References

- [6.1] C. M. Caves, "Quantum-mechanical noise in an interferometer", *Phys. Rev. D* **23**, 1693 (1981).
- [6.2] Y. Yamamoto and H. A. Haus, "Preparation, measurement and information capacity of optical quantum states", *Rev. Mod. Phys.* **58**, 1001 (1986).
- [6.3] T.C. Ralph, "Continuous variable quantum cryptography", *Phys. Rev. A* **61**, 010303 (1999).
- [6.4] M. Hillary, "Quantum cryptography with squeezed states", *Phys. Rev. A* **61**, 022309 (2000).
- [6.5] T. Miya, Y. Terunuma, T. Hosaka, and T. Moyashito, "Ultimate low-loss single-mode fiber at 1.55 μm ", *Electron. Lett.* **15**, p.106–108 (1979).
- [6.6] M. Li and Daniel A. Nolan, "Optical Transmission Fiber Design Evolution", *Journal of Lightwave Technology* **26**, p.1079 (2008).
- [6.7] D. F. McGuigan, C. C. Lam, R. Q. Gram, A. W. Hoffman, D. H. Douglass, H. W. Gutche, "Measurements of the Mechanical Q of Single-Crystal Silicon at Low Temperatures", *J. Low Temp. Phys.* **30**, 621 (1978).
- [6.8] R. Dong, J. Heersink, J. Corney, P. Drummond, U. Andersen, G. Leuchs, "Experimental evidence for Raman-induced limits to efficient squeezing in optical fibers", *Opt. Lett.* **33**, 116–118 (2008).
- [6.9] Y. Eto, T. Tajima, Y. Zhang, and T. Hirano, "Observation of squeezed light at 1.535 μm using a pulsed homodyne detector", *Opt. Lett.* **32**, 1698 (2007).

- [6.10] N. Nishizawa, K. Sone, J. Higuchi, M. Mori, K. Yamane, and T. Goto, "Squeezed Vacuum Generation Using Symmetric Nonlinear Polarization Interferometer", *Jpn. J. Appl. Phys.* **41**, L130 (2002).
- [6.11] J. Feng, X. Tian, Y. Li, and K. Zhanga, "Generation of a squeezing vacuum at a telecommunication wavelength with periodically poled LiNbO₃", *Appl. Phys. Lett.* **92**, 221102 (2008).
- [6.12] H. Vahlbruch, M. Mehmet, S. Chelkowski, B. Hage, A. Franzen, N. Lastzka, S. Goßler, K. Danzmann, and R. Schnabel, "Observation of Squeezed Light with 10-dB Quantum-Noise Reduction", *Phys. Rev. Lett.* **100**, 33602 (2008).
- [6.13] A. Franzen, B. Hage, J. DiGuglielmo, J. Fiurášek, R. Schnabel, "Experimental Demonstration of Continuous Variable Purification of Squeezed States", *Phys. Rev. Lett.* **97**, 150505 (2006).
- [6.14] Y. Takeno, M. Yukawa, H. Yonezawa, and A. Furusawa, "Observation of -9 dB quadrature squeezing with improvement of phase stability in homodyne measurement", *Opt. Express* **15**, 4321–4327 (2007).
- [6.15] G. Hétet, O. Glöckl, K. A. Pilypas, C. C. Harb, B. C. Buchler, H.-A. Bachor, and P. K. Lam, "Squeezed light for bandwidth-limited atom optics experiments at the rubidium D1 line", *J. Phys. B* **40**, 221–226 (2007).
- [6.16] T. Aoki, G. Takahashi, and A. Furusawa, "Squeezing at 946nm with periodically poled KTiOPO", *Opt. Express* **14**, 6930–6935 (2006).
- [6.17] K. Goda, O. Miyakawa, E. E. Mikhailov, S. Saraf, R. Adhikari, K. McKenzie, R. Ward, S. Vass, A. J. Weinstein, and N. Mavalvala, "A quantum-enhanced prototype gravitational-wave detector", *Nat. Phys.* **4**, 472–476 (2008).
- [6.18] N. Grosse, S. Assad, M. Mehmet, R. Schnabel, T. Symul, and P.K. Lam, "Observation of Entanglement between Two Light Beams Spanning an Octave in Optical Frequency", *Phys. Rev. Lett.* **100**, 243601 (2008).
- [6.19] H. Vahlbruch, S. Chelkowski, B. Hage, A. Franzen, K. Danzmann, and R. Schnabel, "Coherent Control of Vacuum Squeezing in the Gravitational-Wave Detection Band", *Phys. Rev. Lett.* **97**, 011101 (2006).

A quantum-enhanced fiber Sagnac interferometer

The injection of squeezed light can be used to improve the sensitivity of an interferometer beyond the limit imposed by the zero point fluctuation of the electromagnetic field. Here, we report on the realization of such a quantum enhanced interferometer with a fiber-based Sagnac topology. Continuous wave squeezed states at 1550 nm with a noise reduction of 6.4 dB below shot noise were produced by type I optical parametric amplification and subsequently injected into the dark port of the interferometer. A reduction of the interferometer shot noise by 4.5 dB was observed, and the enhancement of the signal-to-noise ratio for a phase modulation signal generated within the interferometer could be demonstrated. We achieved a 95% fiber transmission for the squeezed states, which suggests that corresponding fiber-based quantum metrology and communication systems are feasible.

Originally published as M. Mehmet et al. *Opt. Lett.* **35**, 1665–1667 (2010).

7.1 Introduction

Fiber Sagnac interferometers are used as optical rotation sensors and fiber optic gyroscopes [7.1], but their versatility has led to numerous further application that include, among others, fiber loop mirrors [7.2] serving as high reflectors, fiber optic current sensors [7.3], and applications in the automotive industry [7.4].

For a given geometry and laser power, the sensitivity of any such optical measurement device is fundamentally limited by the so-called shot noise. For uncorrelated photons,

i.e., for coherent states of light, the smallest measurable phase change is given by $\Delta\phi \geq 1/\sqrt{N}$, where N is the photon number per measurement time. Consequently, the sensors' performance can be improved by increasing the laser power. However, excess phase and polarization noise stemming from photon-phonon interactions like stimulated Raman scattering [7.5], stimulated Brillouin scattering, and guided acoustic wave Brillouin scattering [7.6] constrain the maximum transmittable power through conventional all-silica fibers. An arbitrary increase in laser power to improve the sensitivity is therefore not possible.

In 1981, Cave [7.7] envisaged a way how to enable the measurement beyond the shot-noise limit (SNL). The quantum-mechanical approach to the interferometer response (to a phase signal) showed that all the measurement noise comes from only *one* quadrature of the vacuum field entering the interferometer through the unused port of its 50:50 beam splitter. Caves' idea was to replace the vacuum field by a squeezed field that exhibits less noise in this quadrature, thereby reducing the quantum noise and hence increasing the signal to shot noise ratio. The two quadrature components of the electromagnetic field are the amplitude and phase quadrature, \hat{X}_1 and \hat{X}_2 , respectively. Their variances are restricted by an uncertainty relation of the form $\Delta^2\hat{X}_1 \cdot \Delta^2\hat{X}_2 \geq 1$. The minimum uncertainty state with symmetrically distributed noise $\Delta^2\hat{X}_1 = \Delta^2\hat{X}_2 = 1$ corresponds to the field's ground state and the so-called vacuum field. A state with a quadrature variance below unity is called a squeezed state, and the variance suppression factor is called the squeezing factor. Following Caves' suggestions several table top experiments demonstrated quantum enhanced Mach-Zehnder [7.8], polarization [7.9], and Michelson interferometers [7.10–7.12]. In all of these experiments freely propagating continuous-wave (cw) laser beams were used. Generally, a critical issue in the quantum enhancement of interferometers is the optical loss introduced by the interferometer, because loss is a decoherence effect and degrades the squeezing factor. A quantum enhanced fiber-based interferometer is more difficult to realize because of absorption and scattering in the optical fiber. Also, the mode matching of a squeezed field into a fiber is critical and should be close to perfect. The same is true for the quantum efficiency of the final photoelectric detection. For instance, an optical loss of 20% diminishes a squeezing factor from 10 to 3.6; see, for example [7.13]. In the pulsed laser regime squeezed states of light are produced by using the optical Kerr effect in fibers. Unfortunately, the high laser intensities required set Raman-induced limits to efficient squeezing in optical fibers [7.5]. Squeezed states of cw laser radiation are efficiently produced by parametric downconversion in optical resonators containing a second-order nonlinear crystal. Squeezing factors greater than ten have been realized recently at the laser wavelength of 1064 nm [7.13, 7.14]. Also recently, squeezed states of cw laser light at 1550 nm could be produced [7.15]. This wavelength is in the c-band transmission window of standard telecommunication

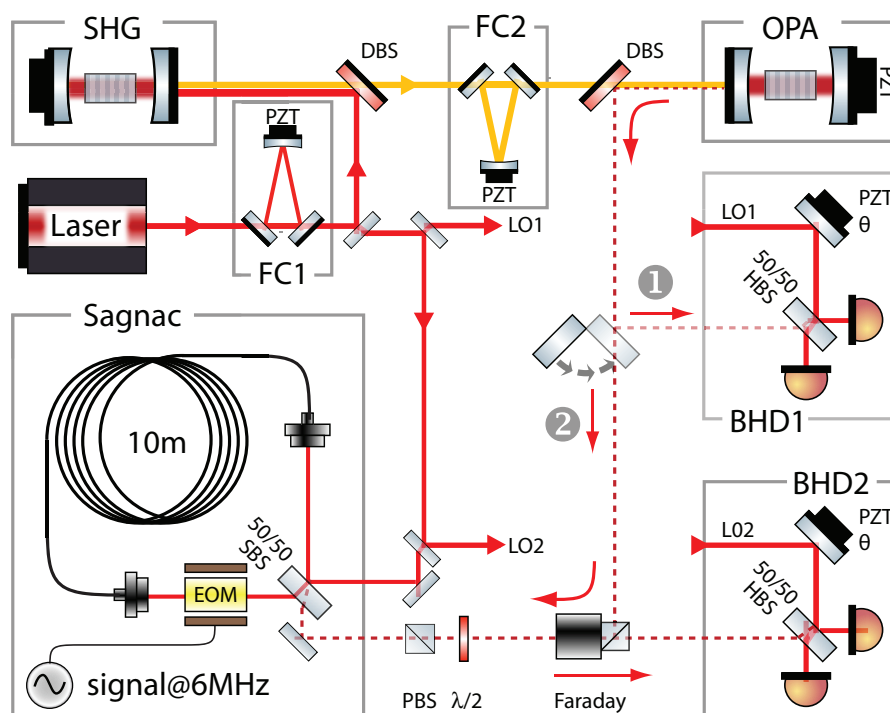


Figure 7.1 — Schematic diagram of the optical setup. The experiment is driven by a fiber laser emitting 1550 nm radiation. SHG, second-harmonic generator producing the 775 nm pump field; FCs, filter cavities for spatial mode cleaning; PZT, piezo-electric transducer; DBS, dichroic beam splitter; OPA, optical parametric amplifier generating squeezed states; LO, local oscillator beam of the balanced homodyne detector, BHD. For characterization the squeezed field was sent via path 1 onto BHD1. To quantum enhance the Sagnac interferometer the squeezing was sent along path 2 and was injected into the dark signal port by using a Faraday rotator, half-wave plate, and a polarizing beam splitter (PBS). EOM, electro optic modulator to generate a phase modulation signal inside the Sagnac interferometer. The interferometer signal and the squeezed quantum noise was detected with BHD2.

fibers, where attenuation and dispersion effects are comparatively weak. In this Letter, we report the realization of a fiber Sagnac interferometer with a sensitivity beyond its SNL. Squeezed light from a nonlinear resonator was injected into the fiber interferometer. The interferometer signal and the squeezed quantum noise were detected by a high-quantum-efficiency balanced homodyne detector. A nonclassical sensitivity improvement of 4.5 dB was achieved.

7.2 Experimental setup

Figure 7.1 illustrates our experimental setup. A 10 m fiber Sagnac interferometer was operated with a cw erbium microfiber laser at 1550 nm. The two output fields of the 50:50 Sagnac beam splitter (SBS) were carefully mode matched into the ends of a 10 m polarization maintaining PANDA-type fiber with $10.5 \mu\text{m}$ mode field diameter and numerical aperture of 0.12. In addition to two lenses in each arm of the interferometer, aspheric lenses with $f = 11 \text{ mm}$ were used to compensate for the strong divergence due to the fiber. The fiber had antireflective (AR) coatings on its end faces to minimize coupling loss for the traversing light. The single-path transmission efficiency was determined to be $95(\pm 1)\%$ by a relative power measurement with a single photo detector in front of and behind the fiber.

For the generation of squeezed light at 1550 nm we employed type I parametric downconversion (optical parametric amplification) in a $2 \text{ mm} \times 1 \text{ mm} \times 10 \text{ mm}$ periodically poled potassium titanyl phosphate (PPKTP) crystal inside a single-ended standing wave cavity with coupling-mirror power reflectivity of 90% and 20% for the fundamental and harmonic field, respectively. The crystal had AR coatings on its end faces with residual reflection $\approx 0.25\%$, which together with $0.1\%/ \text{cm}$ absorption loss within the crystal and the mirror transmittance of 10% resulted in 90% escape efficiency. The second-harmonic pump field at 775 nm was generated in another nonlinear standing wave cavity. For details on the squeezed light generation at 1550 nm we refer to [7.15].

7.3 Characterization of the squeezed states

The squeezed field from the optical parametric amplifier (OPA) cavity was guided by a flip mirror into a balanced homodyne detector (BHD1) for characterization (path 1 in Fig. 7.1). The visibility with the homodyning local oscillator (LO) was 0.994. By changing the relative phase θ between LO and signal beam with a piezo actuated mirror the measured quadrature $X(\theta) = \cos(\theta)X_1 + \sin(\theta)X_2$ was determined. The collected data are shown in Fig. 7.2. The vacuum (shot) noise reference level was measured with the signal input blocked. When the signal port was opened and the phase angle was set to detect the squeezed quadrature [$X(0) = X_1$], a noise reduction of 6.4 dB below the shot noise was obtained. By switching to the orthogonal quadrature [$X(\pi/2) = X_2$] the corresponding antisqueezing of 11.1 dB above shot noise was recorded. These results can be well explained by a simple model assuming

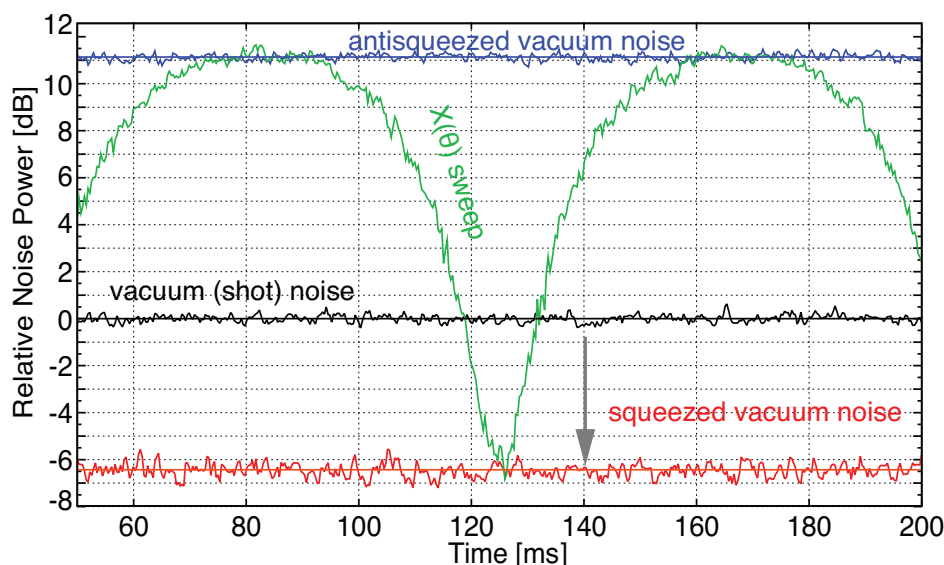


Figure 7.2 — Noise powers of the squeezed states initially emitted by the OPA at a sideband frequency of 5 MHz normalized to the shot-noise level. Shot-noise, squeezed noise, and antisqueezed noise were averaged twice. $X(\theta)$ was recorded by linearly sweeping the LO phase. All traces were recorded with a resolution bandwidth of 300 kHz and a video bandwidth of 300 Hz; the detector dark noise (20 dB below shot noise) was not subtracted.

16% optical loss, zero phase noise, and an initially pure state with 11.8 dB of squeezing (solid lines in Fig. 7.2). In our experiment photons were lost owing to the imperfect escape efficiency [$10(\pm 3)\%$], during propagation [$1(\pm 0.5)\%$], imperfect homodyne visibility (1.2%), and due to the limited quantum efficiency of our custom-made photodiodes which we infer to be about $96(\pm 3)\%$. Obviously the measured squeezing strength was primarily limited by loss due to the imperfect AR coatings on the PPKTP crystal itself.

7.4 Squeezed states in a Sagnac interferometer

After the characterization of the field produced by the OPA the squeezed mode was guided via path 2 (Fig. 7.1) and was precisely modematched to the (dark) signal port mode of the Sagnac interferometer. To generate a phase-modulation signal inside the interferometer a broadband electro-optic modulator (EOM) that could be driven by a signal generator was placed close to the Sagnac beam splitter. The signal at the output port was analyzed with a second balanced homodyne detector (BHD2).

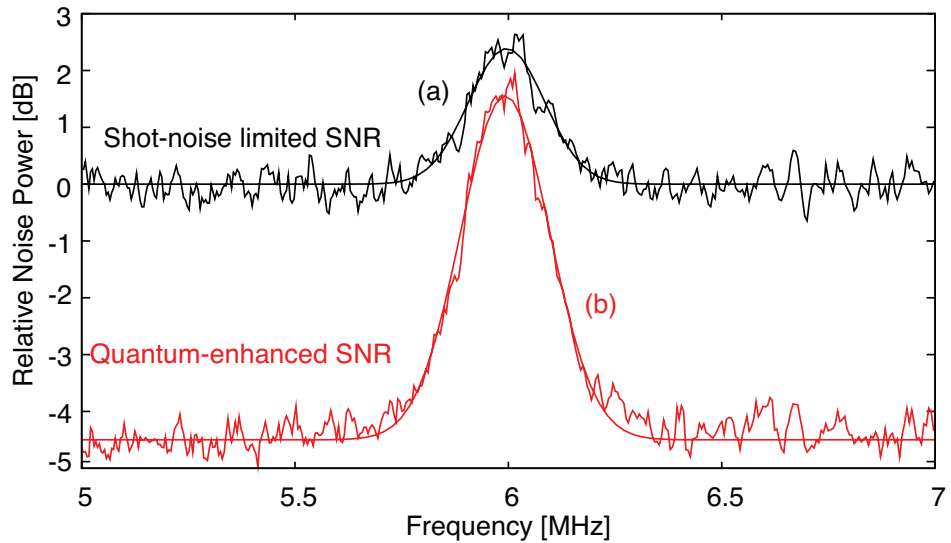


Figure 7.3 — Sagnac interferometer output signal as recorded by the balanced homodyne detector. A 6 MHz phase modulation was measured without [trace (a)] and with [trace (b)] squeezed light input, which yielded a reduction of the interferometer shot noise by 4.5 dB.

Figure 7.3 shows a 6 MHz phase modulation measured with the Sagnac interferometer without (a) and with (b) squeezed light input. Both traces were normalised to the vacuum and recorded with a resolution bandwidth of 200 kHz and a video bandwidth of 200 Hz. The curves were averaged twice; the dark noise was not subtracted from the data. The Sagnac input power was $200 \mu\text{W}$, and the LO power 1.75 mW, which yielded a dark noise clearance of about 16 dB. The LO phase was set to the signal maximum; the phase of the pump and the length of the OPA cavity were set to yield maximum squeezing. By the injection of squeezed vacuum a noise reduction of 4.5 dB below shot noise was achieved, which corresponds to a coherent state laser power increase of 2.8 and a phase sensitivity increase by a factor of about 1.7. When the squeezing was injected into the interferometer further optical loss occurred, which limited the nonclassical sensitivity improvement. The assumption of an additional 15% loss could account for this degradation. The detection efficiencies for BHD1 and BHD2 were almost equivalent and did not need to be taken into account. Independent measurements provided about $2.5(\pm 1)\%$ loss due to the imperfect overlap between squeezed field and Sagnac, $4(\pm 1)\%$ loss due to the double pass through Faraday rotator, PBSs, and a waveplate, 1.2% due to the contrast at the Sagnac beam splitter, and $5(\pm 1)\%$ due to the transmission through the fiber. In addition to that we assume $2(\pm 1)\%$ propagation loss inside the interferometer due to the lenses and the EOM

and 0.5% loss due to lenses and mirrors needed for the squeezed light input. These contributions yield an additional loss of approximately $14(\pm 1)\%$ which, given the experimental uncertainties, accounts well for our observations. Note that light exiting the fiber (both directions) could be matched to a reference cavity with an overlap of 0.996 and 0.997, respectively, illustrating that the transmission efficiency of 95% was essentially limited by suboptimal AR coatings.

7.5 Conclusion

In conclusion we have demonstrated the nonclassical sensitivity improvement of a 10 m fiber Sagnac interferometer by 4.5 dB beyond its SNL. The total loss due to the input mode matching into the fiber and due to the output mode matching to a spatially filtered local oscillator beam was just 5%. Given that conventional optical fibers can have losses as low as ~ 0.2 dB/km [7.16], the 6.4 dB squeezed states generated here could be transmitted over a fiber length of 8 km and would still show 3 dB of squeezing assuming a 5% loss due to input-output mode matching. Our results show that the quantum enhancement of local area (kilometer-size) optical fiber networks and fiber-based measurement devices with squeezed light are feasible.

The authors acknowledge the Deutsche Forschungsgemeinschaft (DFG) and the Centre for Quantum Engineering and Space-Time Research QUEST for financial support.

References

- [7.1] B. Culshaw, “The optical fibre sagnac interferometer: an overview of its principles and applications,” *Meas. Sci. Technol.* **17**, R1–R16 (2006).
- [7.2] D. Mortimore, “Fiber loop reflectors,” *J. Lightw. Technol.* **6**, 1217–1224 (1988).
- [7.3] J. Blake, P. Tantaswadi, and R. de Carvalho, “In-line sagnac interferometer current sensor,” *IEEE Trans. Power Del.* **11**, 116–121 (1996).
- [7.4] J. M. López-Higuera, *Handbook of Optical Fibre Sensing Technology* (John Wiley & Sons, 2002).
- [7.5] R. Dong, J. Heersink, J. F. Corney, P. D. Drummond, U. L. Andersen, and G. Leuchs, “Experimental evidence for raman-induced limits to efficient squeezing in optical fibers,” *Opt. Lett.* **33**, 116–118 (2008).

- [7.6] D. Elser, C. Wittmann, U. L. Andersen, O. Glockl, S. Lorenz, C. Marquardt, and G. Leuchs, “Guided acoustic wave brillouin scattering in photonic crystal fibers,” *Journal of Physics: Conference Series* **92**, 012108 (4pp) (2007).
- [7.7] C. M. Caves, “Quantum-mechanical noise in an interferometer,” *Phys. Rev. D* **23**, 1693 (1981).
- [7.8] M. Xiao, L.-A. Wu, and H. J. Kimble, “Precision measurement beyond the shot-noise limit,” *Phys. Rev. Lett.* **59**, 278–281 (1987).
- [7.9] P. Grangier, R. E. Slusher, B. Yurke, and A. LaPorta, “Squeezed-light-enhanced polarization interferometer,” *Phys. Rev. Lett.* **59**, 2153–2156 (1987).
- [7.10] K. McKenzie, D. A. Shaddock, D. E. McClelland, B. C. Buchler, and P. K. Lam, “Experimental demonstration of a squeezing-enhanced power-recycled michelson interferometer for gravitational wave detection,” *Phys. Rev. Lett.* **88**, 231102 (2002).
- [7.11] H. Vahlbruch, S. Chelkowski, B. Hage, A. Franzen, K. Danzmann, and R. Schnabel, “Demonstration of a squeezed-light-enhanced power- and signal-recycled michelson interferometer,” *Phys. Rev. Lett.* **95**, 211102 (2005).
- [7.12] K. Goda, O. Miyakawa, E. E. Mikhailov, S. Saraf, R. Adhikari, K. McKenzie, R. Ward, S. Vass, A. J. Weinstein, and N. Mavalvala, “A quantum-enhanced prototype gravitational-wave detector,” *Nat. Phys.* **4**, 472–476 (2008).
- [7.13] H. Vahlbruch, M. Mehmet, S. Chelkowski, B. Hage, A. Franzen, N. Lastzka, S. Goßler, K. Danzmann, and R. Schnabel, “Observation of squeezed light with 10-db quantum-noise reduction,” *Phys. Rev. Lett.* **100**, 033602 (2008).
- [7.14] M. Mehmet, H. Vahlbruch, N. Lastzka, K. Danzmann, and R. Schnabel, “Observation of squeezed states with strong photon-number oscillations,” *Phys. Rev. A* **81**, 013814 (2010).
- [7.15] M. Mehmet, S. Steinlechner, T. Eberle, H. Vahlbruch, A. Thüring, K. Danzmann, and R. Schnabel, “Observation of cw squeezed light at 1550 nm,” *Opt. Lett.* **34**, 1060–1062 (2009).
- [7.16] M.-J. Li and D. Nolan, “Optical transmission fiber design evolution,” *J. Lightw. Technol.* **26**, 1079–1092 (2008).

Strongly squeezed light at 1550 nm

Continuous-wave squeezed states of light at the wavelength of 1550 nm have recently been demonstrated, but so far the obtained factors of noise suppression still lag behind today's best squeezing values demonstrated at 1064 nm. Here we report on the realization of a half-monolithic nonlinear resonator based on periodically-poled potassium titanyl phosphate which enabled the direct detection of up to 12.3 dB of squeezing at 5 MHz. Squeezing was observed down to a frequency of 2 kHz which is well within the detection band of gravitational wave interferometers. Our results suggest that a long-term stable 1550 nm squeezed light source can be realized with strong squeezing covering the entire detection band of a 3rd generation gravitational-wave detector such as the Einstein Telescope.

Originally published as M. Mehmet et al. *Opt. Express* **19**, 25763–25772 (2011).

8.1 Introduction

It has been shown by Caves [8.1] that squeezed light can be used to enhance the sensitivity of (quantum noise limited) interferometers as they pursue the first direct detection of gravitational waves (GWs). Caves' analysis revealed that the quantum noise contribution to the interferometer output signal was almost completely caused by the vacuum noise coupling into the interferometer through the open port of its 50/50 beam splitter. The replacement of this vacuum field by a field with less quantum noise in the measured quadrature, namely a squeezed vacuum state, would directly

decrease the photon shot noise on the detector and hence increase the output signal to noise ratio.

All current GW interferometers are operated with lasers at 1064 nm. Accordingly, squeezed light research within the GW community has mainly been focused on the generation of continuous-wave (cw) squeezed light at that respective wavelength. Maximum squeezing values of 11.5 dB from a bulk lithium niobate (LiNbO_3) crystal [8.2] and 12.7 dB from a periodically-poled potassium titanyl phosphate (PPKTP) crystal [8.3] have been reported. These results were obtained in the MHz regime, and more importantly they used *monolithic* resonators to reduce intra-cavity optical loss. Monolithic resonators are not feasible as a GW detector squeezed light source, because a fast enough tuning of their resonance frequency to follow the detector's baseline laser has not been achieved so far. Active length/frequency stabilization can be realized by setting up the squeezed light source as a hemilithic (half-monolithic) resonator and feeding back a control signal to the piezo-driven coupling mirror. The implementation of the required control scheme usually introduces excess noise (typically technical laser noise) that masks the squeezing at frequencies below a few megahertz. In order to generate squeezing within the detection band of today's GW detectors, which ranges from about 10 Hz to 10 kHz, Vahlbruch et al. [8.4] proposed and demonstrated what they called a *coherent control scheme*. This control scheme facilitated the detection of squeezed light at frequencies of as low as 1 Hz [8.5]. A similar control scheme was used to construct the GEO 600 squeezed light source [8.6] that produced 8–9 dB of squeezing in a detection band from 10 Hz to 10 kHz. Just recently, this squeezed light source was successfully incorporated as an add-on into the km-scale gravitational wave detector GEO 600 [8.7, 8.8]. The injection of squeezed vacuum states into GEO 600 led to a broadband noise reduction of up to 3.5 dB in the detectors's shot-noise limited regime (above 700 Hz).

With the feasibility of squeezed light injection having been demonstrated, squeezing could contribute to achieving the envisaged sensitivities of the second generation of GW detectors such as Advanced Virgo [8.9] and Advanced LIGO [8.10]. Here, the application of squeezed light allows for the reduction of the design laser power and thus the potentially critical thermal load on the interferometer's optical components [8.11]. Beyond these advanced detectors, plans for third-generation instruments already exist, e.g. those presented in the recent European design study for the so-called Einstein Telescope (ET) [8.12]. To improve the displacement sensitivity in the low-frequency range it is proposed to use cryogenically cooled interferometers with silicon test masses, which would reduce the thermal noise contribution to the detector sensitivity. Consequently, these detectors would need to be driven by 1550 nm lasers [8.13, 8.14]. As squeezing enhancement is indeed considered for ET, cw squeezed states at 1550 nm covering the frequencies from 1 Hz to 10 kHz are required to achieve a broad-band

reduction of its quantum noise.

Squeezed states of light at a wavelength of 1550 nm have only recently been produced in the cw regime [8.15–8.17] with the highest value of 9.9 dB reported in [8.17]. So far, squeezing factors beyond 10 dB were reported from monolithic cavity designs and at megahertz frequencies only. Here, we report on the observation of 1550 nm squeezed light from an optical parametric amplifier that was designed as a hemilithic resonator and generated squeezing values exceeding 10 dB at frequencies of as low as 18 kHz. Squeezed vacuum states were generated using quasi phase-matched degenerate parametric down-conversion, also known as optical parametric amplification, in a crystal made of PPKTP. The crystal end face and a piezo-driven coupling mirror were used to realize the squeezing resonator in the desired hemilithic configuration. By means of balanced homodyne detection, a non-classical noise reduction of 12.3 ± 0.2 dB was directly observed at a sideband frequency of 5 MHz. Furthermore, we extended our investigation to the sub megahertz-regime which revealed a squeezing factor of more than 10 dB from 80 kHz down to a frequency of 18 kHz. A maximum noise suppression of 11.4 ± 0.5 dB was observed between 60 kHz and 80 kHz. Despite a considerable degradation of the squeezing level from 18 kHz downwards some degree of noise reduction expanded well into the detection band of GW detectors with a remaining 5 dB of squeezing measured at a frequency of 2 kHz.

8.2 Experimental setup

A schematic of our experimental setup is shown in Fig. 8.1. As the laser source we used a commercially available high power cw erbium microfiber laser with an output power of 1.5 W. The laser was transmitted through a three-mirror ring cavity (FC1) that provided spatio-temporal filtering of the beam for the downstream experiment. Approximately 20 mW of the transmitted light were reserved to be used as the local oscillator (LO) for balanced homodyne detection (BHD). Approximately 1 W of the remaining light was sent into a second-harmonic generator (SHG) to furnish the 775 nm pump field needed to drive the optical parametric amplifier (OPA). The SHG was a single-ended standing wave cavity built by two mirrors with 25 mm radius of curvature with a double anti-reflection (AR) coated, 10 mm long PPKTP crystal in between. The end mirror was highly reflective (HR) for both wavelengths; the piezo-driven coupling mirror had a 90 % power reflectivity for the fundamental and only a marginal reflectivity (< 0.2 %) for the second-harmonic field. Taking into account the refractive index of $n = 1.816$ for PPKTP at 1550 nm and the spacing of 20 mm between the crystal end faces and the mirrors, the cavity waist size and linewidth

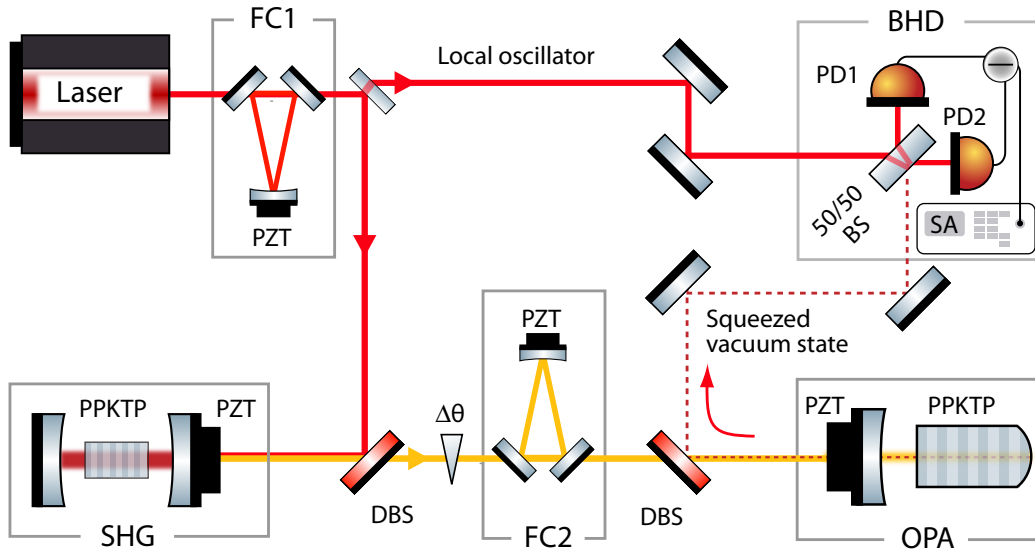


Figure 8.1 — Schematic of the experiment. Laser: 1550 nm fiber laser. FCs, filter cavities for spatio-temporal mode cleaning at both wavelengths. PZT, piezoelectric transducer; SHG, external second-harmonic generator to produce the 775 nm pump field; BS, beam splitter; DBS, dichroic beam splitter; PDs, photo diodes; SA, spectrum analyzer that converts the differential current of the two photo diodes into variances; BHD, balanced homodyne detector for the characterization of the squeezed field.

were $w_0 = 60 \mu\text{m}$ and $\text{FWHM} = 43 \text{ MHz}$, respectively. A second ring cavity (FC2) with specifications similar to FC1 was incorporated to reduce amplitude and phase fluctuations on the pump field. In order to servo-control the length of FC1, FC2 and the SHG to be resonant with their respective carrier fields a modulation-demodulation locking technique was used. The required phase modulations were imprinted onto the light using electro-optical modulators (not shown in Fig. 8.1) with frequencies (101.25 MHz for FC1 and FC2, 138 MHz for the SHG) chosen to be far outside the cavity linewidth such that unwanted sidebands on the transmitted light were kept small. The filtered pump beam was then mode matched to the TEM_{00} mode of the OPA with a mode matching efficiency of 95%.

Our OPA included a piezo-actuated coupling mirror and a PPKTP crystal of dimensions $9.3 \text{ mm} \times 2 \text{ mm} \times 1 \text{ mm}$. The crystal end face had a radius of curvature of 12 mm and was HR coated for 1550 nm and 775 nm, thus serving as the cavity end mirror. The PPKTP front side was AR coated for both wavelengths. An air gap of 23 mm length was realized between the AR coated side of the crystal and the coupling mirror.

As the input/output coupler we chose a half-inch substrate that had a power reflectivity of 90 % for the fundamental and 20 % for the second harmonic field and had a radius of curvature of 25 mm. The intra-cavity waist size and linewidth were $40\ \mu\text{m}$ and 63 MHz, respectively. A peltier element beneath the crystal was used to keep the phase matching temperature at around 40°C .

The squeezed states propagated in the opposite direction to the pump. By reflection at a dichroic beam splitter (DBS) the squeezed field was separated from the pump and was directed towards a balanced homodyne detector. The homodyne detector essentially consists of a 50/50 beam splitter and two photo detectors (PD1 and PD2) that detect the light in the output ports. The difference signal is then converted into a variance by spectrum analyzer (SA). The photo diodes we used for our homodyne detector were custom-made InGaAs PIN diodes with an active area of $300\ \mu\text{m}$ in diameter and a quantum efficiency of $\sim 99\%$.

In squeezing experiments the interference contrast between the local oscillator and the squeezed (signal) field on the 50/50 beam splitter (also known as the homodyne visibility) is crucial because any mode mismatch quadratically translates into optical loss which degrades the squeezing level. To adjust the homodyne visibility a bright beam was needed that resembled the squeezed vacuum output of the OPA. To this end an auxiliary beam (omitted in Fig.8.1) was matched to the TEM_{00} mode through the HR rear surface of the OPA. With this control beam the OPA length could be locked and the transmitted light propagated congruent with the mode to be squeezed. By carefully adjusting the overlap between auxiliary signal beam and LO a fringe visibility of 99.5% was achieved. During data taking the auxiliary field was blocked. This ensured true vacuum squeezing and avoided the degradation of the squeezing by additional noise from the control beam. The rigidity of the cavity construction allowed us to keep the squeezed light source on resonance by solely applying DC-voltage to the piezo.

8.3 Observation of 12.3 dB squeezing at 5 MHz sideband frequency

The two observables of interest were the amplitudes of the amplitude quadrature \hat{X}_1 and the phase quadrature \hat{X}_2 of the electromagnetic field. The homodyne detector measured their respective variances which obey an uncertainty relation, $\Delta^2 \hat{X}_1 \cdot \Delta^2 \hat{X}_2 \geq 1/16$ [8.18]. The relative phase θ between signal beam and local oscillator defines the quadrature under investigation, given by $\hat{X}(\theta) = \hat{X}_1 \cos \theta + \hat{X}_2 \sin \theta$. As depicted in Fig.8.1, in our setup a phase shifter (piezo driven mirror) in the pump path allowed

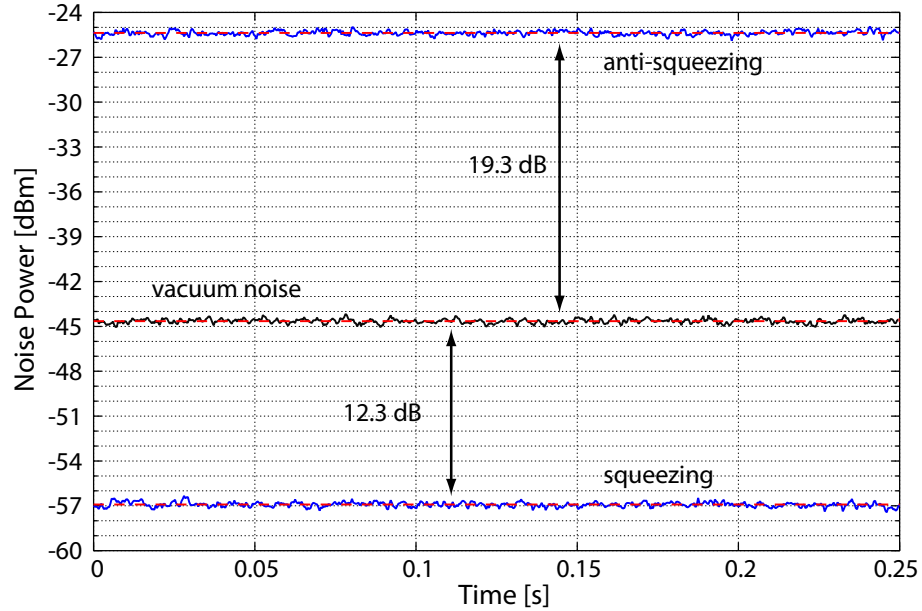


Figure 8.2 — Balanced homodyne measurements of the quadrature noise variances. The vacuum reference was recorded with a LO power of 11.8 mW and a blocked signal port. The OPA was driven with a pump power of approximately 171 mW. With an open signal port, the squeezed variance and the anti-squeezed variance were measured by choosing the corresponding relative phase between signal field and LO. The depicted measurements are averages of 2 traces that were recorded at a Fourier frequency of 5 MHz, with a resolution bandwidth of 200 kHz and a video bandwidth of 200 Hz. No data postprocessing was applied, i.e., the data still include electronic dark noise, and thus represent direct observations. A linear fit to the linearized variances was used to determine the variance mean values and the associated standard deviation. The anti-squeezing was at $+19.3 \pm 0.2$ dB relative to the vacuum noise, whereas the squeezing was at -12.3 ± 0.2 dB.

us to vary the phase of the pump incident on the OPA. This led to a change of the phase with which the squeezing was produced and hence enabled us to adjust θ to measure, e.g., the squeezed quadrature ($X(0) = X_1$) or the anti-squeezed quadrature ($X(\pi/2) = X_2$), respectively. The pump power fluctuations due to beam pointing relative to the eigenmode of FC2 were below 1% and could be neglected. The output signal of the homodyne detector, i.e., the differential current of the two photo diodes, was converted into variances with a spectrum analyzer. We performed measurements at a sideband frequency of 5 MHz and with a pump power of approximately 171 mW. Note that this value is already corrected for the 95% mode-matching efficiency of the pump field into the OPA and that this correction is also included in all other pump

power values given below. The data as collected by the spectrum analyzer are shown in Fig .8.2. Approximately 11.8 mW of LO power was used to obtain the vacuum (or shot noise) reference level with the signal input port of the 50/50 beam splitter blocked. When the input port was opened, the phase θ was subsequently adjusted to measure the anti-squeezed and the squeezed quadrature. A squeezing value of 12.3 ± 0.2 dB below shot noise was directly measured. The corresponding anti-squeezing was 19.3 ± 0.2 dB above the shot noise level. The homodyne detector's electronic dark noise was 26 dB below the vacuum noise and was not subtracted from the data.

8.4 Characterization of the OPA

For the below-threshold OPA the anticipated variances of the squeezed and anti-squeezed quadratures (V_1 and V_2 , respectively) can be modeled by [8.19]

$$V_{1,2} = 1 \pm \eta_{\text{det}}\eta_{\text{esc}} \frac{4\sqrt{P/P_{\text{thr}}}}{(1 \mp \sqrt{P/P_{\text{thr}}})^2 + 4(2\pi f\kappa^{-1})^2}, \quad (8.1)$$

where P is the second-harmonic pump power and P_{thr} is the amount of pump power needed to reach the OPA threshold. The total detection efficiency $\eta = \eta_{\text{det}}\eta_{\text{esc}}$, where η_{det} is the detection efficiency including propagation loss, the homodyne visibility (that is the quality of the mode overlap of the signal and LO on the 50/50 beam splitter), and the quantum efficiency of the photo diodes, and η_{esc} is the escape efficiency of the OPA cavity defined as $\eta_{\text{esc}} = T/(T + L)$, with the amplitude transmissivity T of the coupling mirror and the cavity round trip loss L . With the cavity round-trip length l and the speed of light c the decay rate of the cavity can be defined as $\kappa = c(T + L)l^{-1}$, and f is the measurement frequency.

The amount of detectable squeezing is not limited by optical loss alone. Fluctuations in the relative phase between signal and LO can likewise degrade the measured squeezing level. In an experiment, such phase noise might have numerous origins, for example unstable locking loops, residual phase modulation, or acoustically induced mirror motion. When assuming the standard deviation of the normally distributed phase fluctuations to be small, phase jitter with an rms of θ_{fluc} is equal to the homodyne detector measuring at a phase offset θ_{fluc} . The resulting variances can then be written as

$$V'_{1,2} = V_{1,2} \cos^2 \theta_{\text{fluc}} + V_{2,1} \sin^2 \theta_{\text{fluc}}. \quad (8.2)$$

At a Fourier frequency of 5 MHz, we repeatedly took zero-span measurements of squeezing and anti-squeezing at different pump powers. The collected data are shown

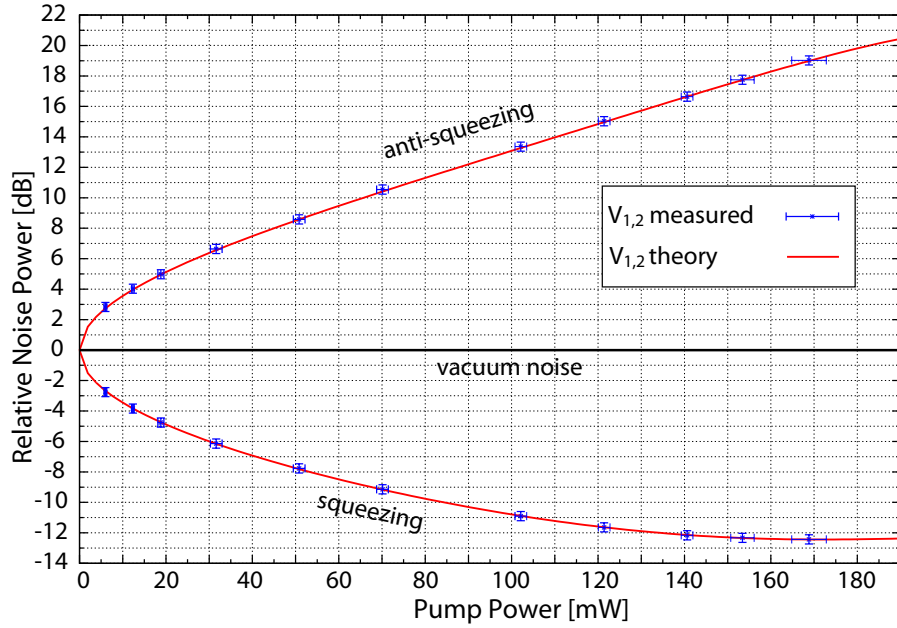


Figure 8.3 — Pump power dependence of anti-squeezed and squeezed quadrature variances. All values were obtained from zero-span measurements at 5 MHz. In order to fit the numerical model, all the data were dark-noise corrected and subsequently normalized to the vacuum reference.

in Fig. 8.3. All measurements were normalized to their respective vacuum level. Here, the contribution of the electronic detector dark noise was subtracted and hence the value of best (optimum) squeezing improved to -12.4 ± 0.3 dB. The horizontal error bars correspond to the fluctuation of the pump power P during data taking. For constant monitoring of P , a calibrated photo diode in transmission of a steering mirror in the pump path was used. The absolute error of a given pump power is $\pm 3\%$ due to the measurement uncertainty of the power meter used for calibration. The vertical error bars are the standard deviation of 0.3 dB as given by the linear fit to each recorded trace. Taking into account the parameters of our cavity, namely $l = 7.98$ cm, $T = 10\%$, $L = 0.1\%$, and the measurement frequency $f = 5$ MHz, we fitted for the total detection efficiency, the threshold power and the amount of phase noise using our model defined in Eqs. (8.1) and (8.2). This yields the following values: $\eta = 0.965 \pm 0.002$, $P_{\text{thr}} = 221 \pm 3$ mW, $\theta_{\text{fluc}} = 0.66 \pm 0.06^\circ$. We confirmed these results by inserting the obtained values into Eq. (8.2) to model the frequency dependence of our squeezer and compared it to measured squeezing spectra. For that we took measurements from 2.5 MHz to 50 MHz at several pump powers between

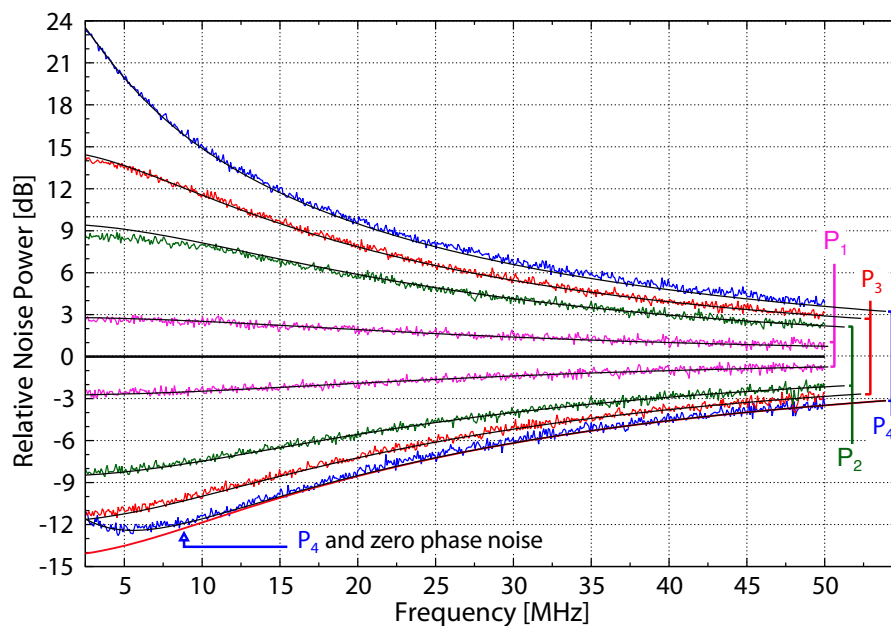


Figure 8.4 — Pump power dependence of the squeezing spectra, experiment and theory. All depicted traces are averages of 10 individual traces each recorded with a resolution bandwidth $RBW = 500$ kHz and video bandwidth $VBW = 2$ kHz. All traces were corrected for electronic detector dark noise and were normalized to the vacuum level. The theoretical predictions (solid lines) were obtained from Eq. (8.2) using $\eta = 0.965$, $P_{thr} = 221$ mW, and $\theta_{fluc} = 0.66^\circ$ with the respective pump power values of $P_1 = 6$ mW, $P_2 = 56$ mW, $P_3 = 106$ mW, and $P_4 = 180$ mW. The remaining cavity parameters were used as given in the text. The bottom curve shows the squeezing spectrum under the assumption of zero phase noise.

6 mW and 180 mW. The collected data are depicted in Fig. 8.4. All spectra were averaged 10 times. As can be seen in Fig. 8.4 our theoretical model does indeed provide a good prediction of the experimental outcome. We especially note the quality of the fit with regards to the phase noise parameter θ_{fluc} since a considerable degradation of the squeezing level at frequencies below 5 MHz becomes apparent when approaching high pump powers. Assuming zero phase noise, the squeezing level would approach 14 dB as indicated by the bottom curve in Fig. 8.4.

8.5 Low frequency performance

For the observation of squeezing in the kHz regime, we used our homodyne detector together with a low-noise FFT-analyzer. This enabled us to measure the quantum noise from 80 kHz downwards. For all measurements a power of 4.8 mW for the LO was used. This yielded a vacuum reference level with a clearance from the electronic dark noise of approximately 15 to 20 dB over the entire FFT window. Therefore, no data postprocessing to subtract the detector dark noise was applied. The resulting noise spectra are shown in Fig. 8.5. The measured anti-squeezing [trace (b)]

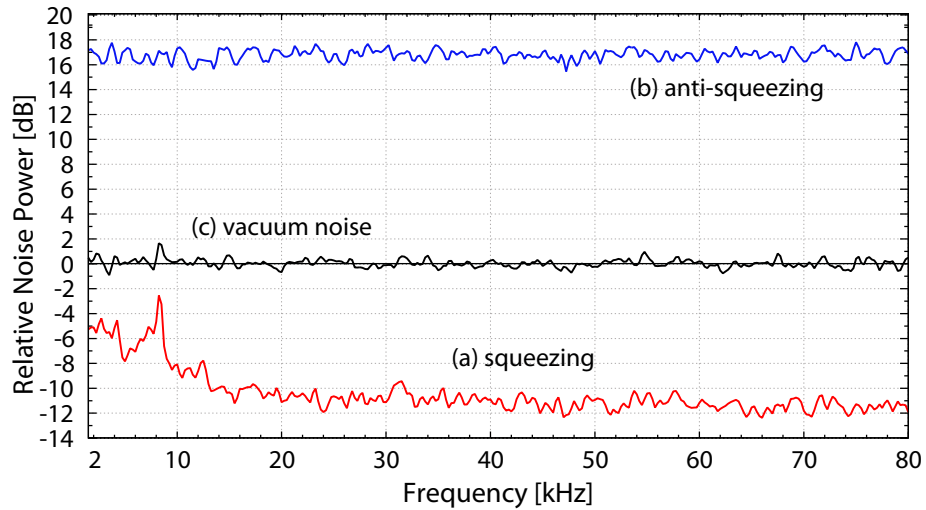


Figure 8.5 — Squeezing at frequencies between 1.5 kHz and 80 kHz. All traces were measured with RBW of 250 Hz and were normalized to the vacuum noise level corresponding to a LO power of 4.8 mW. Each measurement point is the averaged root mean square value of 20 [40 for trace(c)] measurements. Trace (a) shows the direct observation of more than 10 dB of squeezing down to a frequency of 18 kHz with a maximum noise suppression of -11.4 ± 0.5 dB between 60 kHz and 80 kHz. Below 18 kHz the squeezing level degraded, reaching approximately -5 dB at 2 kHz. The peak at 8 kHz was caused by a residual, non-stationary amplitude modulation from FC1. The anti-squeezing [trace (b)] was 16.8 ± 0.5 dB above the vacuum noise level as measured by the homodyne detector [trace (c)]. Electronic dark noise was not subtracted from the measurement data.

was at 16.8 ± 0.5 dB above the vacuum noise level [trace (c)]. The spectrum of the squeezed quadrature [trace (a)] showed a maximum non-classical noise suppression of -11.4 ± 0.5 dB between 60 kHz and 80 kHz. Going down in frequency the squeezing slightly decreased reaching -10.7 ± 0.4 dB at 20 kHz. From 18 kHz downwards the

squeezing level degraded considerably. We attribute this mainly to two characteristics of our setup. First, no stabilization scheme was used to control the relative phase between LO and signal field. Hence, acoustically excited motion cannot be compensated for and together with the prolonged measurement times at smaller sideband frequencies this led to an averaging effect that decreased the observed squeezing level. Second, no Faraday isolator was incorporated between the squeezing resonator and homodyne detector to protect the OPA from back-scattered and reflected light. It is known that stray light can introduce excess noise [8.20, 8.21] and can cause parasitic interferences [8.5] within the system. Both effects can impair or even completely annihilate squeezing in the audio band. Despite the roll-up towards lower frequencies, squeezing of approximately -5 dB could still be observed at 2 kHz.

8.6 Conclusion

By means of balanced homodyne detection we directly observed 12.3 dB of squeezing of the vacuum fluctuations of a 1550 nm cw laser beam at a sideband frequency of 5 MHz. This non-classical noise reduction was achieved by degenerate parametric down-conversion below threshold in a standing wave resonator. High quality optics and the low absorption of the PPKTP crystal made it possible to construct the squeezing resonator as a hemilithic cavity and still keep the optical loss small enough to detect such strong squeezing. Pump power dependent squeezing values were used to characterize our squeezer in terms of optical loss and phase noise. By fitting a theoretical model to the data the overall optical loss and residual phase noise between signal and LO were determined to be 3.5% and 0.66° , respectively. Note that the value obtained for the optical loss includes the escape efficiency of the squeezing resonator, propagation loss and the subsequent homodyne detection. The amount of phase noise could most likely be reduced by the implementation of a stable control for the phase of the pump beam as well as the homodyne detection phase. Assuming zero residual phase noise, 14 dB of (dark noise corrected) squeezing would then be detectable in our setup. However, such control schemes are usually not easily realized without introducing excess noise from the participating light fields and hence were not pursued here. Although our overall loss value of 3.5% is already small, we believe that a further loss reduction is possible and that even higher values of squeezing should be feasible with current technology.

Squeezed vacuum states at frequencies within the detection band of GW interferometers can be used to enhance the sensitivity of the respective detector. These frequencies typically range from some Hertz up to 10 kHz. Here, we were able to measure up to

11.4 dB of squeezing below 80 kHz. Even though from 18 kHz downwards acoustically induced modulation and residual stray light degraded the level of squeezing, it extended into the detection band of a GW detector. Owing to the hemilithic layout of the squeezed light resonator, a coherent control scheme according to [8.4] is applicable. With such a control scheme the squeezing spectrum would presumably broaden to cover the entire range of frequencies down to a few hertz. Additionally, the required long-term stability would be obtained and an even higher squeezing factor can be expected since the aforementioned phase noise would be reduced.

We note that squeezed light at 1550 nm is also of interest in the field of fiber-based quantum communication because this wavelength lies in one of the telecommunication windows associated with low loss of silica fibers.

Acknowledgments

The authors acknowledge the International Max Planck Research School (IMPRS) on Gravitational Wave Astronomy for support.

References

- [8.1] C. M. Caves, "Quantum-mechanical noise in an interferometer," *Phys. Rev. D* **23**, 1693 (1981).
- [8.2] M. Mehmet, H. Vahlbruch, N. Lastzka, K. Danzmann, and R. Schnabel, "Observation of squeezed states with strong photon-number oscillations," *Phys. Rev. A* **81**, 013814 (2010).
- [8.3] T. Eberle, S. Steinlechner, J. Bauchrowitz, V. Händchen, H. Vahlbruch, M. Mehmet, H. Müller-Ebhardt, and R. Schnabel, "Quantum Enhancement of the Zero-Area Sagnac Interferometer Topology for Gravitational Wave Detection," *Phys. Rev. Lett.* **104**, 251102 (2010).
- [8.4] H. Vahlbruch, S. Chelkowski, B. Hage, A. Franzen, K. Danzmann, and R. Schnabel, "Coherent Control of Vacuum Squeezing in the Gravitational-Wave Detection Band," *Phys. Rev. Lett.* **97**, 011101 (2006).
- [8.5] H. Vahlbruch, S. Chelkowski, K. Danzmann, and R. Schnabel, "Quantum engineering of squeezed states for quantum communication and metrology," *New. J. Phys.* **9**, 371 (2007).

- [8.6] H. Vahlbruch, A. Khalaidovski, N. Lastzka, Ch. Gräf, K. Danzmann and R. Schnabel, "The GEO 600 squeezed light source," *Class. Quantum Grav.* **27**, 084027 (2010).
- [8.7] H. Grote for the LIGO Scientific Collaboration, "The status of GEO 600," *Class. Quantum Grav.* **25**, 114043 (2008).
- [8.8] The LIGO Scientific Collaboration, "A gravitational wave observatory operating beyond the quantum shot-noise limit," *Nat. Phys.* (to be published).
- [8.9] The Virgo Collaboration, "Advanced Virgo Baseline Design," Virgo Technical Report VIR-0027A-09 (2009), <https://tds.ego-gw.it/ql/?c=6589>.
- [8.10] G. M. Harry (for the LIGO Scientific Collaboration), "Advanced LIGO: the next generation of gravitational wave detectors," *Class. Quantum Grav.* **27**, 084006 (2010).
- [8.11] R. Schnabel, N. Mavalvala, David E. McClelland, and P. K. Lam "Quantum metrology for gravitational wave astronomy," *Nat. Commun.* **1** 121 (2010).
- [8.12] The ET Science Team, "Einstein gravitational wave Telescope (ET) conceptual design study," ET-0106C-10 (2011), <https://tds.ego-gw.it/ql/?c=7954>.
- [8.13] S. Rowan, J. Hough, D. R. M. Crooks, "Thermal noise and material issues for gravitational wave detectors," *Phys. Lett. A* **347** 25–32 (2005).
- [8.14] R. Schnabel, M. Britzger, F. Brückner, O. Burmeister, K. Danzmann, J. Dück, T. Eberle, D. Friedrich, H. Lück, M. Mehmet, R. Nawrodt, S. Steinlechner and B. Willke, "Building blocks for future detectors: Silicon test masses and 1550 nm laser light," *J. Phys.: Conf. Ser.* **228**, 012029 (2010).
- [8.15] M. Mehmet, S. Steinlechner, T. Eberle, H. Vahlbruch, A. Thüring, K. Danzmann, and R. Schnabel, "Observation of cw squeezed light at 1550 nm," *Opt. Lett.* **34**, 1060 (2009).
- [8.16] M. Mehmet, T. Eberle, S. Steinlechner, H. Vahlbruch, and R. Schnabel, "Demonstration of a quantum-enhanced fiber Sagnac interferometer," *Opt. Lett.* **35**, 1665 (2009).
- [8.17] T. Eberle, V. Händchen, J. Duhme, T. Franz, R. F. Werner, and R. Schnabel, "Strong Einstein-Podolsky-Rosen entanglement from a single squeezed light source," *Phys. Rev. A* **83**, 052329 (2011).

- [8.18] C. C. Gerry, and P. L. Knight, *Introductory Quantum Optics* (Cambridge Univ. Press, Cambridge, 2004).
- [8.19] T. Aoki, G. Takahashi, and A. Furusawa, "Squeezing at 946 nm with periodically poled KTiOPO₄," *Opt. Express* **14**, 6930–6935 (2006).
- [8.20] W. P. Bowen, R. Schnabel, N. Treps, H.-A. Bachor, and P. K. Lam, "Recovery of continuous wave squeezing at low frequencies," *J. Opt. B* **4**, 421 (2002).
- [8.21] K. McKenzie, N. Grosse, W. P. Bowen, S. E. Whitcomb, M. B. Gray, D. E. McClelland, and P. K. Lam, "Squeezing in the Audio Gravitational-Wave Detection Band," *Phys. Rev. Lett.* **93**, 161105 (2004).

Summary and Conclusion

The research presented in this thesis focuses on the realization of strongly squeezed states of light at the wavelengths of 1064 nm and 1550 nm in the continuous-wave regime. Squeezed light at these wavelengths has the potential to contribute to reaching the envisaged sensitivities of second- and third-generation GW detectors. Furthermore, squeezed light is a valuable resource in quantum information. Here, especially the wavelength of 1550 nm is of interest in view of fiber-based quantum communication because it is in the third telecommunication window of conventional silica fibers where optical loss is weakest. In several experiments presented here, the limits to the obtainable factors of noise suppression were investigated and applications of squeezed light were demonstrated.

A monolithic resonator made from a $\text{MgO}:\text{LiNbO}_3$ crystal was used to generate squeezed states at 1064 nm via degenerate parametric down-conversion. The nonclassical states were strongly squeezed (11.5 dB), were of high purity (with a vacuum contribution $< 5\%$), and were in a well-defined spatial Gaussian fundamental mode (99.8% mode overlap with a spatially filtered local oscillator beam). These properties are of great importance for applications in high-precision measurements as well as in quantum information. The OPA could not be operated closer to threshold than approximately 54% and thus the squeezing level was effectively limited by an insufficient amount of pump power. The monolithic squeezed-light source also exhibited a broad squeezing bandwidth and thus constitutes a bright source of quantum-correlated photons. *Monolithic* resonators do not seem feasible as a GW detector squeezed-light source, because a reliable tuning of their resonance frequency to follow the detector's baseline laser has not been achieved so far. Therefore, a squeezed-light resonator in a *half-monolithic* configuration was realized. A quantum noise suppression of 12.3 dB (94%) was directly measured at 5 MHz, this time using a PPKTP crystal. It was found

that such strong squeezing can be utilized to accurately measure the optical loss of an optical system. A total detection efficiency of 96% was determined by comparison of experimental data with the theoretical model. A loss analysis was used to derive an absolute lower bound of 98% for the quantum efficiency of the photo diodes. These were made from the same wafer as the photodiode currently used in the GW detector GEO 600. Therefore, it can be inferred that at maximum 2% of GEO's overall loss budget is attributable to its photo detector. This is important in view of the GEO-HF upgrade in which it is planned to realize a sensitivity improvement by up to 6 dB with squeezed-light input. Assuming 12 dB of squeezing entering the dark port of the interferometer, all further loss is required to be smaller 18%, since the total optical loss within the entire system must not be larger than 20% (see Fig. 3.5).

In a proof of principle experiment it was shown that PPKTP is also a suitable nonlinear material for the generation of squeezed states at the telecommunication wavelength of 1550 nm. Using off-the-shelf crystals and generic InGaAs photo diodes, a nonclassical noise suppression of 5.3 dB was achieved at a sideband frequency of 5 MHz.

An increase in the squeezing at the wavelength of 1550 nm to 6.4 dB was accomplished by using custom-made photo diodes for the homodyne detector. The injection of the squeezed states into the dark port of a fiber-based Sagnac interferometer yielded a nonclassical noise reduction of 4.5 dB beyond the interferometer's shot-noise limit. These results illustrate that the quantum enhancement of local-area optical fiber networks and fiber-based measurement devices with strongly squeezed light are feasible. It was found that the squeezing level at 1550 nm was primarily limited due to the residual reflections of the AR coating on the PPKTP crystal facet inside the squeezing resonator. By using a custom-polished and high-quality coated crystal and optics, a maximum squeezing level of 12.3 dB could be observed in the MHz regime. The spectrum of the squeezed quadrature also exhibited a strong noise suppression of 11.4 dB at sideband frequencies between 60 kHz and 80 kHz. The analysis of the system revealed that a total optical loss on the squeezing of 3.5% and phase jitter (between the squeezed field and the local oscillator field) of $\sim 0.7^\circ$ were the limiting factors to the detectable squeezing level. Moreover, the same squeezed-light source was used to demonstrate 1550 nm squeezed light at sideband frequencies within the audio band for the first time. At 20 kHz, the squeezing was still 10.7 dB below shot-noise. From 18 kHz downwards the level of noise suppression degraded gradually, reaching a value of approximately 5 dB at 2 kHz. However, this low-frequency degradation is well understood and can be overcome by the implementation of the control scheme already in use in the GEO 600 squeezed-light laser. Consequently, long-term stable 1550 nm squeezed-light sources providing 12-14 dB in the frequency band of the Einstein Telescope seem viable already today.

Curriculum vitae

Moritz Mehmet

Date of birth: Sep. 7th, 1978

Place of birth: Gießen, Germany

University studies

- | | |
|-------------------|----------------------------------------------------------------------------------------------------------------------------------------------------------------------------|
| 04/2006 – present | Doctoral studies at the Max-Planck-Institut für Gravitationsphysik (Albert-Einstein-Institut) and the Institut für Gravitationsphysik of the Leibniz Universität Hannover. |
| 08/2008 – present | Research associate within the Cluster of Excellence QUEST (Centre for Quantum Engineering and Space-Time Research). |
| 04/2006 – 07/2008 | Scholarship holder at the International Max Planck Research School (IMPRS) on Gravitational Wave Astronomy. |
| 07/2007 – 09/2007 | Research visit at the Australian National University, Canberra. |
| 01/1999 – 03/2006 | Undergraduate studies in Engineering Physics with final degree Master of Science, Carl von Ossietzky Universität Oldenburg. |
| 11/2004 – 03/2006 | Master's thesis at the Max-Planck-Institut für Gravitationsphysik. |
| 09/2002 – 03/2003 | Study visit at Chalmers University of Technology, Gothenburg, Sweden. |

Community service

- | | |
|-------------------|----------------------------|
| 09/1998 – 09/1999 | Caritasverband Gießen e.V. |
|-------------------|----------------------------|

Education

- | | |
|---------|------------------------------|
| 06/1998 | Abitur, Herderschule Gießen. |
|---------|------------------------------|

Publications

Publications within the Quantum Interferometry Group

- 1 | M. Mehmet, St. Ast, T. Eberle, S. Steinlechner, H. Vahlbruch, and R. Schnabel, "*Squeezed light at 1550 nm with a quantum noise reduction of 12.3 dB*", Optics Express **19**, 25763–25772 (2011).
- 2 | St. Ast, R. Moghadas Nia, A. Schönbeck, N. Lastzka, J. Steinlechner, T. Eberle, M. Mehmet, S. Steinlechner, and R. Schnabel, "*High-efficiency frequency doubling of continuous-wave laser light*", Opt. Lett. **36**, 3467–3469 (2011).
- 3 | T. Eberle, S. Steinlechner, J. Bauchrowitz, V. Händchen, H. Vahlbruch, M. Mehmet, H. Müller-Ebhardt, R. Schnabel, "*Quantum Enhancement of the Zero-Area Sagnac Interferometer Topology for Gravitational Wave Detection*", Phys. Rev. Lett. **104**, 251102 (2010).
- 4 | R. Schnabel, M. Britzger, F. Brückner, O. Burmeister, K. Danzmann, J. Dück, T. Eberle, D. Friedrich, H. Lück, M. Mehmet, R. Nawrodt, S. Steinlechner, and B. Willke, "*Building blocks for future detectors: Silicon test masses and 1550 nm laser light*", J. Phys.: Conf. Ser. **228**, 012029 (2010).
- 5 | M. Mehmet, H. Vahlbruch, N. Lastzka, K. Danzmann, and R. Schnabel, "*Observation of squeezed states with strong photon-number oscillations*", Phys. Rev. A **81**, 013814 (2010).
- 6 | M. Mehmet, T. Eberle, S. Steinlechner, H. Vahlbruch, and R. Schnabel, "*Demonstration of a quantum-enhanced fiber Sagnac interferometer*", Opt. Lett. **35**, 1665 (2009).
- 7 | M. Mehmet, S. Steinlechner, T. Eberle, H. Vahlbruch, A. Thüring, K. Danzmann, and R. Schnabel, "*Observation of cw squeezed light at 1550 nm*", Opt. Lett. **34**, 1060 (2009).

130 PUBLICATIONS

- 8 | A. Thüring, Ch. Gräf, H. Vahlbruch, M. Mehmet, K. Danzmann, and R. Schnabel, "*Broadband squeezing of quantum noise in a Michelson interferometer with Twin-Signal-Recycling*", *Opt. Lett.* **34**, 824-826 (2009).
- 9 | N. B. Grosse, S. Assad, M. Mehmet, R. Schnabel, T. Symul, and P. K. Lam, "*Observation of Entanglement between Two Light Beams Spanning an Octave in Optical Frequency*", *Phys. Rev. Lett.* **100**, 24360 (2008).
- 10 | H. Vahlbruch, M. Mehmet, S. Chelkowski, B. Hage, A. Franzen, N. Lastzka, S. Goßler, K. Danzmann, and R. Schnabel, "*Observation of Squeezed Light with 10 dB Quantum-Noise Reduction*", *Phys. Rev. Lett.* **100**, 033602 (2008).

Publications within the LIGO Scientific Collaboration

- 11 | The LIGO Scientific Collaboration, "*A gravitational wave observatory operating beyond the quantum shot-noise limit*", *Nat. Phys.* **7**, 962–965 (2011).
- 12 | J. Abadie, . . . , M. Mehmet, . . . , and J. Palfreyman, "*Beating the Spin-down Limit on Gravitational Wave Emission from the Vela Pulsar*", *ApJ* **737**, 93 (2011).
- 13 | J. Abadie, . . . , M. Mehmet, . . . , and J. Zweizig, "*Search for gravitational waves from binary black hole inspiral, merger, and ringdown*", *Phys. Rev. D* **83**, 122005 (2011).
- 14 | J. Abadie, . . . , M. Mehmet, . . . , and S. Buchner, "*Search for gravitational waves associated with the August 2006 timing glitch of the Vela pulsar*", *Phys. Rev. D* **83**, 042001 (2011).
- 15 | J. Abadie, . . . , M. Mehmet, . . . , and K. Yamaoka, "*Search for gravitational wave bursts from six magnetars*", *ApJ* **734**, L35 (2011).
- 16 | J. Abadie, . . . , M. Mehmet, . . . , and J. Zweizig, "*Calibration of the LIGO gravitational wave detectors in the fifth science run*", *Nucl. Instrum. Meth. A* **624**, 223–240 (2010).
- 17 | J. Abadie, . . . , M. Mehmet, . . . , and J. Zweizig and The LIGO Scientific Collaboration, "*First Search for Gravitational Waves from the Youngest Known Neutron Star*", *ApJ* **722**, 1504 (2010).

- 18 | B. P. Abbott,..., M. Mehmet,..., and J. Zweizig, "*Search For Gravitational-wave Bursts Associated with Gamma-ray Bursts using Data from LIGO Science Run 5 and Virgo Science Run 1*", *ApJ* **715**, 1438 (2010).
- 19 | J. Abadie,..., M. Mehmet,..., and J. Zweizig, "*Search for gravitational waves from compact binary coalescence in LIGO and Virgo data from S5 and VSR1*", *Phys. Rev. D* **82**, 102001 (2010).
- 20 | J. Abadie,..., M. Mehmet,..., and K Belczynski, "*Predictions for the rates of compact binary coalescences observable by ground-based gravitational-wave detectors*", *Class. Quantum Grav.* **27**, 173001 (2010).
- 21 | J. Abadie,..., M. Mehmet,..., J. Zweizig and The LIGO Scientific Collaboration & The Virgo Collaboration, "*Search for Gravitational-wave Inspiral Signals Associated with Short Gamma-ray Bursts During LIGO's Fifth and Virgo's First Science Run*", *ApJ* **715**, 1453 (2010).
- 22 | J. Abadie,..., M. Mehmet,..., and J. Zweizig, "*All-sky search for gravitational-wave bursts in the first joint LIGO-GEO-Virgo run*", *Phys. Rev. D* **81**, 102001 (2010).
- 23 | B. P. Abbott,..., M. Mehmet,..., and B. Stappers, "*Searches for Gravitational Waves from Known Pulsars with Science Run 5 LIGO Data*", *ApJ* **713**, 671 (2010).
- 24 | B. P. Abbott,..., M. Mehmet,..., J. Zweizig and The LIGO Scientific Collaboration, "*Search For Gravitational-wave Bursts Associated with Gamma-ray Bursts using Data from LIGO Science Run 5 and Virgo Science Run 1*", *ApJ* **715**, 1438 (2010).
- 25 | B. P. Abbott,..., M. Mehmet,..., and J. Zweizig, "*An upper limit on the stochastic gravitational-wave background of cosmological origin*", *Nature* **460**, 990 (2009).
- 26 | B. P. Abbott,..., M. Mehmet,..., and J. Zweizig, "*Search for gravitational wave ringdowns from perturbed black holes in LIGO S4 data*", *Phys. Rev. D* **80**, 062001 (2009).
- 27 | B. P. Abbott,..., M. Mehmet,..., and J. Zweizig, "*Search for high frequency gravitational-wave bursts in the first calendar year of LIGO's fifth science run*", *Phys. Rev. D* **80**, 102002 (2009).

- 28 | B. P. Abbott,..., M. Mehmet,..., and J. Zweizig, "*Stacked Search for Gravitational Waves from the 2006 SGR 1900+14 Storm*", *ApJ* **701**, L68-L74 (2009).
- 29 | B. P. Abbott,..., M. Mehmet,..., and J. Zweizig, "*Search for gravitational-wave bursts in the first year of the fifth LIGO science run*", *Phys. Rev. D* **80**, 102001 (2009).
- 30 | B. P. Abbott,..., M. Mehmet,..., and J. Zweizig, "*Einstein@Home search for periodic gravitational waves in early S5 LIGO data*", *Phys. Rev. D* **80**, 042003 (2009).
- 31 | B. P. Abbott,..., M. Mehmet,..., and J. Zweizig, "*Search for Gravitational Waves from Low Mass Compact Binary Coalescence in 186 Days of LIGO's fifth Science Run*", *Phys. Rev. D* **80**, 047101 (2009).
- 32 | B. P. Abbott,..., M. Mehmet,..., J. Zweizig, and F. Robinet, "*First LIGO search for gravitational wave bursts from cosmic (super)strings*", *Phys. Rev. D* **80**, 062002 (2009).
- 33 | B. P. Abbott,..., M. Mehmet,..., and J. Zweizig, "*Search for Gravitational Waves from Low Mass Binary Coalescences in the First Year of LIGO's S5 Data*", *Phys. Rev. D* **79**, 122001 (2009).
- 34 | B. P. Abbott,..., M. Mehmet,..., and J. Zweizig, "*All-sky LIGO Search for Periodic Gravitational Waves in the Early S5 Data*", *Phys. Rev. Lett.* **102**, 111102 (2009).
- 35 | B. P. Abbott,..., M. Mehmet,..., and J. Zweizig, "*LIGO: The Laser Interferometer Gravitational-Wave Observatory*", *Rep. Prog. Phys.* **72**, 076901 (2009).